

Università degli Studi di Padova
Centro Ricerche Fusione (**CRF**)

Universidade de Lisboa
Instituto Superior Técnico (**IST**)

Università degli Studi di Napoli Federico II

JOINT RESEARCH DOCTORATE IN FUSION SCIENCE AND ENGINEERING
Cycle XXXI

DEVELOPMENT OF EQUIVALENT PLASMA-CIRCUITS AXISYMMETRIC MODELS FOR EXISTING AND FUTURE TOKAMAKS

Coordinator: Prof. Paolo Bettini

Supervisor: Prof. Roberto Ambrosino

Co-Supervisor: Prof. Gianmaria De Tommasi

Ph.D. Student: Antonio Castaldo

Padova, October 2018

Dedicata a mio nonno Antonio

Contenents

Ringraziamenti

Giunto alla fine di questi 3 splendidi anni di dottorato, mi accingo a ringraziare tutti coloro che mi sono stati vicino e che mi hanno sempre supportato durante questo percorso.

In primo luogo, il mio ringraziamento più grande va al mio Tutor Prof. Roberto Ambrosino. Non finirò mai di essergli grato per i costati stimoli e per il continuo incoraggiamento. Grazie per avermi sostenuto, grazie per avermi redarguito e grazie per aver sempre creduto nelle mie capacità.

Un ringraziamento speciale va al Prof. Raffaele Albanese, le sue incredibili doti scientifiche possono essere superate solo dalla sua grande umanità. Lo ringrazio per avermi coinvolto nel progetto DTT e per essere fonte di costante ispirazione e motivazione.

Desidero inoltre ringraziare tutti i membri del consorzio CREATE in particolare i Prof. Gianmaria De Tommasi e Alfredo Pironti per gli interessanti dibattiti scientifici e per il continuo incoraggiamento, i Prof. Giuseppe Ambrosino, Vincenzo Coccorese, Marco Ariola e Massimiliano Mattei per i consigli e per la cordialità sempre mostrata.

Ringrazio inoltre il coordinatore del corso di dottorato Prof. Paolo Bettini per la magnifica organizzazione dei corsi e per la costante presenza.

Un ringraziamento doveroso va a tutte le persone con le quali ho avuto la fortuna e il piacere di collaborare in particolare il Prof. Giuseppe Calabrò, il dott. Francesco Maviglia, il dott. Flavio Crisanti e il dott. Giuseppe Ramogida. Desidero inoltre ringraziare i colleghi dell'ASIPP in particolare il Prof. Bingjia Xiao e il dott. Zhengping Luo per avermi concesso l'opportunità di lavorare su EAST.

Grazie a questo dottorato ho potuto inoltre incontrare colleghi fantastici in particolare desidero ringraziare i miei colleghi sia dell'Università Federico II in particolare Vincenzo, Roberto, Mariano e Nicola sia dell'Università Parthenope in particolare Diego, Michele, Gaetano, Angel, Salu, Maria, Tonia, Hossein, Andrea, Sergio e Bilel. Ci siamo sempre supportati l'un l'altro sostenendoci a vicenda ed è questo che ci ha permesso di raggiungere i nostri obiettivi!

Dico inoltre grazie ai miei colleghi del XXXI° ciclo di dottorato in Fusion Science and Engineering Adriano, Matteo I., Matteo V., Giuseppe e Daniele. Li ringrazio per il tempo speso insieme durante i corsi, per i bei momenti passati e per gli interessanti scambi di idee circa la nostra ricerca scientifica!

Vorrei inoltre ringraziare i miei più cari amici in particolare Gaetano, Tommaso ed Enzo ai quali sono legato da un'amicizia decennale. Grazie per il continuo sostegno e per i momenti unici che abbiamo condiviso!

In ultimo desidero ringraziare la mia famiglia, in particolare i miei genitori Gennaro e Giuseppa e mia sorella Maria Laura per avermi sempre sostenuto in questo percorso, senza il loro supporto non ce l'avrei mai fatta. Ringrazio mia nonna Maria, i miei zii Pina e Giovanni e mia cugina Angela per essersi sempre interessati al mio percorso di studi e per essermi sempre stati vicino.

In ultimo dedico questa tesi a mio nonno Antonio uomo di una bontà unica che mi ha insegnato l'importanza di essere umili.

Abstract

Electromagnetic modelling of tokamak devices assumes a crucial role in scientific research both for the study of operating devices and for the design of future reactors. Having reliable models is fundamental for the design of model-based control systems for the vertical stability of confined plasmas and to provide good performances in terms of plasma shape, current and position control. Finally, it is possible to use these models to optimize geometrical configurations and PF coil systems of future generation devices.

My PhD activities have been focused on the development of plasma equilibria and electromagnetic dynamical models for EAST tokamak, site in Hefei, P.R. China, and the future generation tokamaks DEMO and DTT. CREATE-NL and CREATE-L computation codes have been used to perform the electromagnetic analyses.

An important part of this work has been dedicated to the study of alternative plasma configurations such as Double Null, Snowflake, X-divertor and Super-X. These configurations are currently considered promising by the fusion community in order to tackle the power exhaust problem in view of the construction of the next generation device DEMO. Alternative configurations have been designed on DEMO size tokamak and have been analyzed in terms of costs and benefits illustrating the figure of merits and possible showstopper for the realization of DEMO.

The contents of the thesis are shortly listed below.

In *Chapter 1* the nuclear fusion concept will be presented, analyzing the main fusion reactions which involve Hydrogen and his isotopes illustrating extensively Deuterium-Tritium reaction since it represents the most efficient reaction at operative temperatures of a fusion reactor. Moreover, the concept of plasma will be introduced. Different plasma confinement techniques will be presented with particular emphasis on magnetic confinement.

In *Chapter 2* magnetohydrodynamic (MHD) theory will be introduced. Starting from MHD equations, plasma equilibrium concept will be illustrated achieving the well-known Grad-Shafranov equation in toroidal axisymmetric geometries. Finally, the finite element code CREATE-NL will be presented, which is widely used in fusion scientific community in order to calculate plasma equilibriums in Tokamak devices.

In *Chapter 3* tokamak machines will be introduced, starting from the description of the main components of the reactor (PF coils, Blanket, Vacuum Vessel, etc.) and illustrating the main physical limits which restrict the operation space of the device. A general overview of the main heating techniques (ICRH, ECHR e NBI) and plasma diagnostics employed in a tokamak will be provided. Finally, a brief description of the devices on which the research activity has been focused will be presented.

In *Chapter 4* the research activity performed during the last three years on EAST, DTT and DEMO will be presented. EAST modelling activities have been mainly focused on the development of a finite element model of the EAST device and a reliable dynamic simulator able to reproduce EAST experimental shots. Linearized models of the EAST equilibria in different scenario phases have been produces for the design of a model-based closed loop control for the vertical instability and plasma shape control. DEMO activities have been mainly focused on the definition and optimization of alternative plasma configurations for a DEMO size device. For each alternative configuration concept an optimized geometry and PF coil system has been produced. Moreover, a preliminary vertical stability analysis will be provided. Finally, the main activities on the next generation tokamak DTT will be presented making use of the last version (August 2018) of the geometry design with a major radius of 2.10m. For the DTT device, the breakdown and the reference plasma scenarios for Single Null, Double Null and Snowflake configurations will be shown.

In *Chapter 5* conclusions and future work will be presented.

Sommario

La modellistica elettromagnetica delle macchine di tipo tokamak assume ancora oggi un ruolo cruciale nella ricerca scientifica sia per lo studio dei dispositivi attualmente in funzione che per il design dei futuri reattori. Disporre di modelli affidabili è fondamentale al fine di progettare sistemi di controllo model-based in grado di garantire la stabilità verticale del plasma confinato e di offrire buone performance in termini di controllo di posizione, forma e corrente di plasma. Inoltre, è possibile utilizzare tali modelli per l'ottimizzazione della configurazione geometrica e del sistema di PF coils per i dispositivi di futura generazione.

Le mie attività durante il dottorato sono state incentrate sullo sviluppo di equilibri di plasma e modelli elettromagnetici dinamici per il tokamak EAST, sito ad Hefei, in Cina e per i tokamak di futura generazione DEMO e DTT. I codici di calcolo CREATE-NL e CREATE-L sono stati utilizzati per eseguire le analisi elettromagnetiche.

Una parte importante del presente elaborato sarà inoltre dedicata allo studio delle configurazioni di plasma alternative quali Double Null, Super-X, Snowflake e X-Divertor. Tali configurazioni sono attualmente considerate promettenti dalla comunità fusionistica per affrontare il problema del power exhaust in vista della costruzione del reattore di futura generazione DEMO.

I contenuti del lavoro di tesi verranno di seguito elencati in breve.

Nel *capitolo 1* verrà introdotto il concetto di fusione nucleare analizzando le principali reazioni di fusione che coinvolgono l'Idrogeno e i suoi isotopi illustrando approfonditamente la reazione Deuterio-Trizio in quanto riconosciuta come la più efficiente alle temperature tipiche di un reattore a fusione. Di seguito, verrà introdotto il concetto di plasma e verranno presentate le varie tecniche di confinamento ponendo particolare enfasi sul confinamento magnetico.

Nel *capitolo 2* verrà introdotta la teoria magnetoidrodinamica (MHD). Partendo dall'introduzione delle equazioni MHD, si illustrerà il concetto di equilibrio di plasma pervenendo infine alla ben nota equazione di Grad-Shafranov in geometrie toroidali assialsimmetriche. Infine, verrà introdotto il codice agli elementi finiti CREATE-NL

ampiamente utilizzato nella comunità scientifica per il calcolo degli equilibri di plasma in macchine di tipo tokamak.

Nel *capitolo 3* verranno introdotti i dispositivi tokamak partendo dalla descrizione delle principali componenti del reattore (PF coils, Blanket, Vacuum Vessel, ecc.) illustrando in seguito i principali limiti fisici che limitano lo spazio operazionale della macchina. Verrà inoltre effettuata una panoramica generale delle principali tecniche di riscaldamento (ICRH, ECHR e NBI) e delle diagnostiche che vengono tipicamente utilizzate in un tokamak. Infine, verrà fornita una breve descrizione delle macchine sulle quali è stata incentrata l'attività di ricerca precedentemente menzionati.

Nel *capitolo 4* verrà presentata l'attività di ricerca svolta durante il triennio di dottorato su EAST, DEMO e DTT. Le attività di modellistica su EAST sono state principalmente incentrate sulla modellistica agli elementi finiti della macchina e sullo sviluppo di una piattaforma di simulazione affidabile in grado di riprodurre gli spari sperimentali. Sono stati inoltre sviluppati modelli linearizzati degli equilibri di plasma di EAST in differenti fasi dello scenario di plasma al fine di sviluppare un controllore a ciclo chiuso model-based per il controllo dell'instabilità verticale e della forma di plasma. Le attività relative a DEMO sono state principalmente incentrate sulla definizione e l'ottimizzazione delle configurazioni di plasma alternative. Per ognuna di tali configurazioni sono stati progettati un sistema di PF coil ed una opportuna geometria. Inoltre, verrà fornita un'analisi preliminare di stabilità verticale delle configurazioni. Infine, verranno presentate le principali attività svolte sul tokamak di futura generazione DTT utilizzando l'ultima versione (Agosto 2018) della geometrica con raggio maggiore di 2.10m. Per DTT, il breakdown e gli scenari di riferimento per le configurazioni Single Null, Dobule Null e Snowflake verranno mostrati.

Nel *capitolo 5* verranno presentate le conclusioni e i possibili sviluppi futuri.

Resumò

A modelagem eletromagnética das máquinas tokamak ainda hoje desempenha um papel crucial na pesquisa científica tanto para o estudo de dispositivos atualmente em operação quanto para o projeto de futuros reatores. Ter modelos confiáveis é essencial para projetar sistemas de controle capazes de garantir as propriedades de estabilidade vertical do plasma confinado e oferecer um bom desempenho em termos de controle de posição, forma e corrente de plasma. Além disso, é possível usar esses modelos para a otimização da configuração geométrica e do sistema de PF coils para os futuros dispositivos de geração.

Minhas atividades durante o PhD foram focadas no desenvolvimento de equilíbrios de plasma e modelos eletromagnéticos dinâmicos para tokamak EAST, em Hefei, China e para a futura geração tokamaks DEMO e DTT. Os códigos de cálculo CREATE-NL e CREATE-L foram usados para realizar análises eletromagnéticas

Uma parte importante do presente trabalho também será dedicada ao estudo de configurações alternativas de plasma, como Double Null, Super-X, Snowflake e X-Divertor. Essas configurações são atualmente consideradas promissoras pela comunidade de fusão para resolver o problema de exaustão de energia tendo em vista a construção do reator DEMO de próxima geração.

O conteúdo do trabalho da tese será listado abaixo em breve.

No *capítulo 1*, o conceito de fusão nuclear será introduzido pela análise das principais reações de fusão envolvendo Hidrogênio e seus isótopos, mostrando em detalhes a reação de Deutério-Trítio, reconhecida como a mais eficiente nas temperaturas típicas de um reator de fusão. A seguir, o conceito de plasma será introduzido e as várias técnicas de confinamento serão apresentadas com ênfase particular no confinamento magnético.

No *capítulo 2*, a teoria magneto-hidrodinâmica (MHD) será introduzida. A partir da introdução das equações de MHD, ilustraremos o conceito de equilíbrio de plasma, chegando finalmente à conhecida equação de Grad-Shafranov em geometrias toroidais axial-simétricas. Finalmente, o código de elementos finitos CREATE-NL será introduzido, amplamente utilizado na comunidade científica para o cálculo do balanço de plasma em máquinas tokamak.

No *capítulo 3*, os dispositivos tokamak serão introduzidos a partir da descrição dos principais componentes do reator (PF coils, Blanket, Vacuum Vessel, etc…) ilustrando abaixo os principais limites físicos que delimitam o espaço operacional da máquina. Uma visão geral das principais técnicas de aquecimento (ICRH, ECHR e NBI) e diagnósticos que são tipicamente usados em um tokamak também será realizada. Finalmente, uma breve descrição das máquinas nas quais a atividade de pesquisa mencionada anteriormente foi.

No *capítulo 4*, será apresentada a atividade de pesquisa realizada durante o curso de três anos de doutorado em EAST, DEMO e DTT. As atividades de modelagem no EAST foram focadas principalmente na modelagem de elementos finitos da máquina e no desenvolvimento de uma plataforma de simulação confiável capaz de reproduzir imagens experimentais. Além disso, modelos linearizados do balanço plasmático EAST em diferentes fases do cenário de plasma foram desenvolvidos com o objetivo de desenvolver um controlador baseado em modelo de malha fechada para o controle da instabilidade vertical e da forma do plasma. As atividades relacionadas ao DEMO foram principalmente focadas na definição e otimização das configurações de plasma alternativo. Para cada uma dessas configurações, um sistema de bobina PF e uma geometria adequada foram projetados. Além disso, uma análise preliminar da estabilidade vertical das configurações será fornecida. Finalmente, as principais atividades realizadas no tokamak de próxima geração da DTT serão apresentadas usando a última versão (agosto de 2018) da geometria com um raio maior que 2.10m. Para DTT, os cenários de quebra e referência para as configurações Single Null, Dobule Null e Snowflake serão mostrados.

No *capítulo 5*, as conclusões e possíveis desenvolvimentos futuros serão apresentados.

Chapter 1: Introduction to nuclear fusion

"When we look up at night and view the stars, everything we see is shining because of distant nuclear fusion"

Carl Sagan

In this first chapter the concept of nuclear fusion will be introduced. we will start giving a description of world energy scenario; then, we will analyze the main fusion reactions which involve the Hydrogen and his isotopes with particular emphasis on the Deuterium-Tritium reaction. Finally, the concepts of plasma will be introduced.

1.1 World energy scenario

Since the humankind dawn, welfare and development have been closely related to the availability of energy. Throughout history, starting from the pre-history up to our era, the consumption of energy grew up with a very high rate, especially in the last three centuries:

- In the prehistory, man consumed only the energy needed to feed on, about 2500 kcal (i.e. a glass of oil), which is equivalent to the energy still used today to feed on;
- With the discovery of fire and thus the beginning of cooked foods, consumption doubled, reaching 5000 kcal per day;
- With the beginning and development of the agricultural age, it was necessary to transport goods over significant distances and to use oxen to plough fields, arriving to an energy consumption per person of about 4 times the one needed to just feed on (10000 kcal/day).

The great leap was made with the industrial revolution (between the end of 1700 and beginning of 1800), after which, with the discovery of the steam engine, the consumption increased by a factor of twenty compared to the one needed only to eat (50000 kcal/day). Within less than two centuries, the exponential growth resulted, at

least in the industrialized countries, in an average consumption of 150000 kcal/day per person (approximately 600 MJ/day). The most recent estimates state that in 2012 the total annual energy consumption reached almost 12 Gtoe; dividing these 12 billion tons of oil equivalent for nearly 7 billion (the world population), we get a consumption of about 1.8 toe/inhabitant per year (or about 18 million kcal). If the whole requirement would be covered with oil consumption, it would correspond to the load of about 100 supertankers per day (each one carrying 2 million barrels).

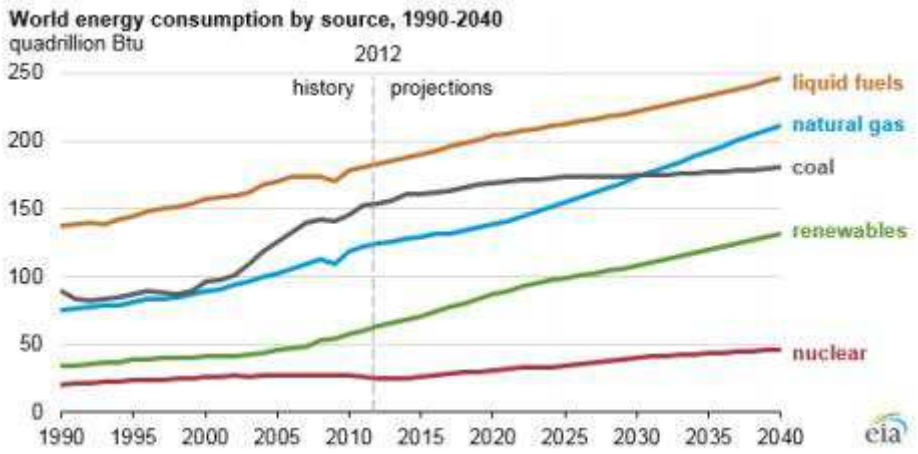

Fig. 1.1 – World energy consumption by EIA [1]

The energy demand per person is increasing due to the constant increase of both the world population and the demand per person.

In particular, according to the International Energy Outlook 2013 (IEO 2013), published on 25 of July 2013 by the Energy Information Administration (EIA) of the US government, "…over the next three decades, the world energy consumption is expected to increase by 56%, driven by growth in the developing world." Currently, the basic sources used worldwide for the supply of such energy are represented by coal, around 28%, and especially by oil, for about 34%; natural gas is the third source, in order of importance, and it is interesting to note that its contribution has steadily and rapidly grown over the past two decades (Fig 1.1). Therefore, the three main primary sources are all fossil and hence non-renewable ("nonrenewable" means that the sources are exploited at a rate higher than the natural renewal rate) and the deposits of these fossil fuels are

continuing decrease. The most optimistic estimates predict that the availability of non-renewable energy sources (such as coal, oil and natural gas) can last at most a few hundred years. Next to the non-renewable sources, there are the so-called "renewable" sources. Among these sources, there is the nuclear power that matches a great demand for energy, about 5%, being the source grown faster in the last thirty years, with a very large penetration, until the early 80's, reducing, in the same period, the use of oil by about 10%. Later, this development has almost stopped and even now, many European countries (such as Germany) are planning to abandon their nuclear power plants, because of the management problems, especially related to the waste (these problems affect widely nuclear fission power plants). The remaining percentage, related to the renewable sources, is unfortunately less significant (Fig. 1.2). These sources are very abundant, non-polluting and inexhaustible but it is difficult to put them at the base of the energy supply, both for their lack of constancy, and because the current technologies suited to exploit them are expensive and do not allow to have a good energy efficiency. Among these sources, there are biomass, 4%, hydropower, 3%, solar energy, 0.5%, and so on towards even smaller percentage. To face a world energy demand constantly growing and to deal with the extinction, at even more rapid rate, of all major fossil energy (non-renewable) sources, research is focusing more and more on renewables and on new fields as the nuclear fusion.

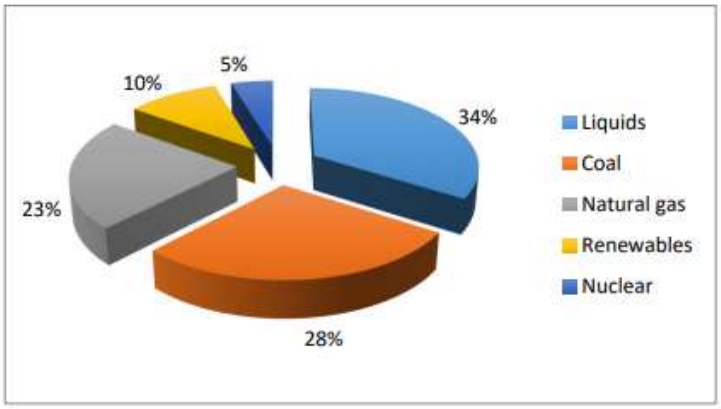

Fig. 1.2 – Energy consumption based on source type

Nuclear fusion is seen as one of the answers to the worldwide energy issues: it is clean, safe and sustainable and does only produce short-living radioactive waste: it is the energy source of the Sun and stars. The scientific results and continue progress achieved so far

in the experimental nuclear fusion field suggest that it will be possible to produce fusion power since the middle of this century. In particular, Europe has become the world leader in the field of fusion through the construction of several experimental machines.

1.2 A brief history of nuclear fusion

The history of nuclear fusion has its roots in the late 20s of the XX° century [2]. Sir Arthur Stanley Eddington, an English astrophysicist, was the first scientist who theorized that the energy coming from the sun was the result of nuclear fusion reactions which take place in the core of the star. Atkinson and Houtermans published a scientific work regarding this subject. Their theory was successively improved by Weizsäker, by Teller and by Bethe (who won the Nobel Prize for Physics in 1967 *"for his contributions to the theory of nuclear reactions, especially his discoveries concerning the energy production in stars"*). In 1930s scientists started to consider the chance to obtain energy from fusion reactions even on Earth. However, fusion reactions which take place in the core of the stars have characteristic times in the order of billions of years and the power per mass unit released is very small. The huge total power released by the stars is mainly related to their gigantic masses. It's therefore evident that, in order to reproduce nuclear fusion on Earth, reactions with smaller characteristic times must be considered. Furthermore, since reacting nuclei must be taken to very high energies, it seemed to be impossible to reproduce such reactions. However, scientific progresses achieved in the development of nuclear fission energy had a strong impact on the chance to obtain energy from nuclear fusion reactions. Indeed in 1945 the first atomic bomb was realized and later, in 1952, the H-bomb was developed by a group of scientists headed by Edward Teller.

It's hence evident that the aim of scientific research about nuclear fusion was to develop nuclear weapons. For this reason, scientific research programs on nuclear fusion were classified as top-secret in countries like USSR, USA and Great Britain. Moreover, in order to protect their research, particular code-names were used to hide the real meaning of the documents. For example, the words *"goo", "altitude"* and *"jet"* were used to code the words *"plasma", "temperature"* and *"magnetic field"* so the phrase *"high altitude goo in a jet"* means *"high temperature plasma in a magnetic field"*.

In 1953 USA president Eisenhower proposed to the *"United Nations General Assembly"* (Fig. 1.3) the creation of an organization to support a peaceful use of nuclear energy and to prevent the development of nuclear weapons (known as *"Atoms for peace"* speech). In 1955 during conference in Genève, USSR presented the idea of a toroidal machine to magnetically confine high temperature plasmas developed by Russian physicists Andrej Sakharov (Fig. 1.4) and Igor Tamm. In 1968 during the third "IAEA" in Novosibirsk [3], Russian scientists announced the T-3 tokamak was producing an electron temperature of $1keV$ (equivalent to 10 million of Celsius degrees). Lyman Spitzer remained skeptical, noting that the temperature measurements were still based on the indirect calculations from the magnetic properties of the plasma. Many concluded they were due to an effect known as runaway electrons, and that the Soviets were measuring only those extremely energetic electrons and not the bulk temperature. After this initial skepticism, the results presented by Russian scientists were confirmed, giving a strong pulse towards the tokamak research.

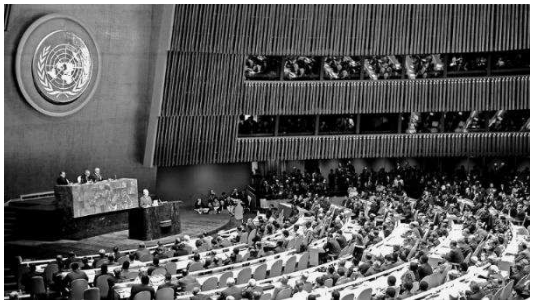

Fig. 1.3 – USA President Eisenhower's speech to the UN General Assembly

Fig. 1.4 – Russian physicist Andrej Sakharov. In 1975 he was awarded with the Nobel Prize for Peace "[*for his] struggle for human rights, for disarmament, and for cooperation between all nations*"

1.3 The nuclear fusion reaction

Nuclear fusion (from the Latin word *"fusio"*, which means "to merge") can be described as "a nuclear reaction in which atomic nuclei of low atomic number fuse to form a heavier nucleus with the release of energy" as shown in Fig 1.5.

The energy produced by means of nuclear fusion reactions can be computed making use of the well-known Einstein's relation:

$$E = (m_r - m_p)c^2$$

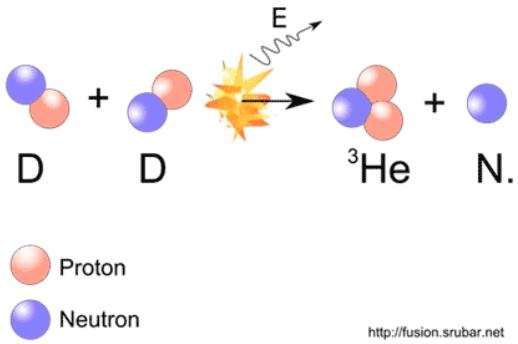

Fig. 1.5 – Nuclear fusion reaction which involves 2 Deuterium nuclei. The reaction results consist in a "light" Helium nucleus, a neutron and an amount of energy

where

- E = Energy released from the nuclear reaction;
- m_r = Total mass of reacting nuclei;
- m_p = Total mass of the products;
- c = Speed of light.

It's hence evident that thermonuclear reactions exploit the mass defect between reactants and products in order to produce energy. The main problem related to the realization of a nuclear fusion reaction is to place near the reacting nuclei in order to start the nuclear process. Indeed, according to the electromagnetism physics, if we try to approach two electric charges equal in sign, a repulsion force (known as Coulomb force) appears. The general form of the Coulomb force is:

$$F = \frac{1}{4\pi\varepsilon_0}\frac{|Q_1|\,|Q_2|}{r^2}$$

where

- F = Repulsive force between the charges;

- ε_0 = Dielectric constant in vacuum equal to $8{,}85418782 \cdot 10^{-12}\ \frac{C^2}{m^2 N}$;
- $|Q_1|$ e $|Q_2|$ = Absolute charge values;
- r = Geometric distance between the charges.

In order to realize the nuclear fusion process, reacting nuclei must be taken at a distance such that the Strong Nuclear Force (one of the four fundamental forces of nature) prevails on coulombian repulsion, this distance is around $10^{-15}\ m$.

1.4 Analysis of the main Hydrogen fusion reactions

In this section, the main fusion reactions involving Hydrogen and his isotopes Deuterium and Tritium will be analyzed. The reasons why these reactions are of interest are mainly related to the wide availability on Earth. Indeed, Hydrogen is the most common chemical element on Earth, Deuterium is present in the water in quantities equal to $25{,}5\ mg/l$ and Tritium can be easily produced through chemical reactions which involve Lithium and neutrons. The *cross-section* (σ) can be seen as measure of the probability that a fusion reaction occurs or, alternatively, it can be interpreted as the area surrounding a *target particle* in which the presence of a second particle (*bullet particle*) leads to an interaction between the particles. In Fig. 1.6, are reported the *cross-sections* of the main reactions involving Hydrogen and his isotopes as function of particle energy.
Let us now introduce and analyze the fusion reactions above mentioned:

1.1) $^2H + {}^3H \rightarrow {}^4He + n + 17{,}6\ MeV$;

1.2) $^2H + {}^2H \rightarrow {}^3He + n + 3{,}3\ MeV$;

1.3) $^2H + {}^2H \rightarrow {}^3H + {}^1H + 4{,}0\ MeV$;

1.4) $^2H + {}^3He \rightarrow {}^4He + {}^1H + 18{,}3\ MeV$.

If we compare the *cross-section* of Deuterium-Tritium reaction with the other ones, it results a higher efficiency of Deuterium-Tritium reaction in the low temperature region respect to the other reactions above listed.

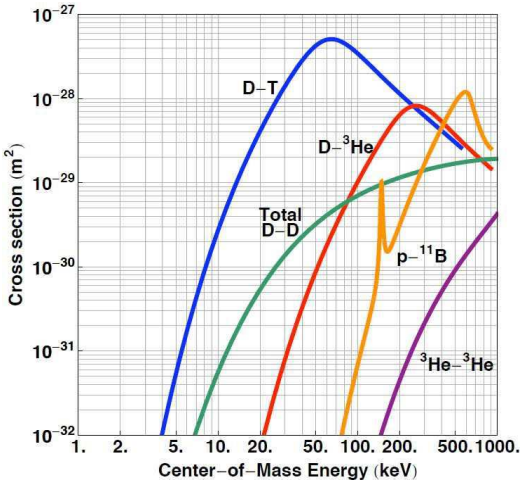

Fig. 1.6 – The *cross-sections* of the main reactions involving hydrogen and his isotopes.

Reactions 1.2 and 1.3 have the same probability to happen and they involve the same reacting atoms. Let us now explicit, for reactions 1.2 and 1.3, how the energy is shared between products:

1.2) $^2H + \ ^2H \ \rightarrow \ ^3He\ (0{,}67\ MeV) + n\ (2{,}63\ MeV)$

1.3) $^2H + \ ^2H \ \rightarrow \ ^3H\ (3\ MeV) + \ ^1H\ (1\ MeV)$

For what concerns reaction 1.2, it's evident that almost all the energy developed by the reaction (about 87%) is absorbed by the neutron which, being lack of electric charge, cannot be confined in the fusion reactor through magnetic fields developed by the coil system. The confinement of the energy in a fusion reactor represents one of the most challenging problem in the design of a fusion device.

To confine most of the energy produced by fusion reactions implies a lesser employment of auxiliary heating systems to keep the temperature at high levels with a resulting benefit in terms of energy balance of the whole system. Furthermore, one of the problems related to neutron's energy is the radio-activation of metallic structures of the device due to the neutron-walls collisions.

Unlike 1.2, reaction 1.3 does not show the same problems, indeed: it does not produce neutrons and the products of the reaction can ben confined through magnetic fields. However, if we compare 1.3 with Deuterium-Tritium and Deuterium-Helium-3 reactions,

it results to be the less efficient both in terms of energy produced and in terms of efficiency at low energies.

For what concerns reaction 1.4, it's easy to note that Deuterium-Helium-3 has a lot of advantages if compared to the other reactions mentioned. Firstly, the reaction does not produce neutrons and the products of the reaction can be easily confined in the reactor chamber. Furthermore, if we compare reaction 1.4 with the other above mentioned, it comes out that Deuterium-Helium-3 reaction is capable to produce the largest quantity of energy that can be confined. Indeed, Deuterium-Helium-3 reaction produces an amount of energy 5 times greater than Deuterium-Tritium reaction since in this reaction about the 80% of the energy developed is absorbed by the neutron that cannot be confined. The main problem related to Deuterium-Helium-3 reaction is the high energy barrier (*Coulomb barrier*) due to electrostatic interaction that the two nuclei need to overcome so they can get close enough to undergo a nuclear reaction. It's also worth to mention that Helium-3 is very rare in nature which leads to the non-trivial problem of searching the fuel for reactions.

1.5 The Deuterium-Tritium reaction

Let us now focus our attention on the Deuterium-Tritium reaction reported in Fig. 1.7. Deuterium is broadly present in water ($25{,}5\ mg/l$) while Tritium (radioactive material with a half-life of 12.3 years) can be easily produced through the following reactions (we indicate with n^* a "slow" neutron):

1.5) $n + {}^{6}Li \rightarrow {}^{4}He + {}^{3}H + 4{,}86\ MeV$;

1.6) $n + {}^{7}Li \rightarrow {}^{4}He + {}^{3}H + n^* - 2{,}5\ MeV$.

The sign '-' in the equation expresses the need to provide energy from the outside. Since Lithium is very abundant on Earth, the production of Tritium can be implemented making use of the neutrons produced by reaction 1.1 coating with Lithium the internal side of the chamber (this concept is known as *"Breeding Blanket"*). However, it is not possible to design the blanket so that all neutrons undergo such a reaction. In order to overcome this

lack and create an overall breeding ratio higher than one, a neutron multiplier as Beryllium or Lead has to be used. The neutron flux from nuclear reactions decays in the blanket; a blanket thickness between 0.6 and 1.0 m is usually sufficient to absorb most of the neutrons. The flow of neutron energy passing through the outer wall of the blanket in the form of heat must be reduced by a factor of 106 ÷ 107 before reaching the superconducting coils to prevent both the radiation damage and the heating of such coils. This protection is obtained by placing a shield of about 1 m thick of material, such as the steel, between the blanket and the coils.

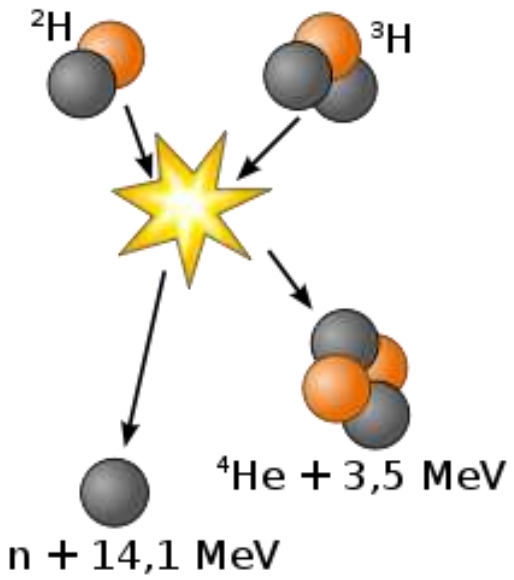

Fig. 1.7 – Deuterium-Tritium nuclear fusion process. The results of the reaction are: a "fast" neutron, a Helium isotope (^4He) and an amount of energy equals to 17,6 MeV

Among the various reactions presented in the previous paragraph, the Deuterium-Tritium reaction results the most efficient at low energies/temperatures since it's characterized by the highest *cross-section*. Let us now examine the partition of energy in reaction 1.1:

1.7) $$^2H + {}^3H \rightarrow {}^4He\ (3{,}53\ MeV) + n\ (14{,}07\ MeV).$$

If we analyze the reaction it results the almost totality of the energy developed (about 80%) is absorbed by the neutron produced. This amount of energy can be retrieved by means of the *blanket* in fact, one of the main tasks of this component is to convert the

kinetic energy of colliding neutrons into thermal energy through wall-neutrons elastic collisions. The heat produced in the fusion power plant *blanket* should be removed through a suitable liquid or gaseous coolant and then transformed into electricity by conventional means, as shown in Figure 1.8. The remaining 20% of the energy developed is absorbed by the Helium-4 isotope which can be easily confined in the chamber. It is hence evident that Deuterium-Tritium reaction appear to be the most promising reaction in order to produce energy from nuclear fusion process

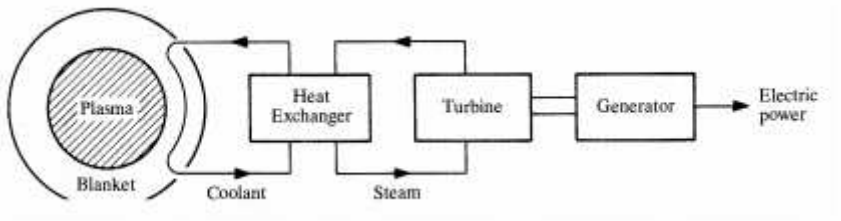

Fig. 1.8 – How thermonuclear power absorbed by the blanket could be converted into electrical power by conventional means (in the example, a steam turbine). [4]

1.6 Coulomb barrier

In order to realize the nuclear fusion process, reacting nuclei must be taken at a distance such that the Strong Nuclear Force (one of the four fundamental forces of nature) prevails on Coulomb repulsion, this distance is around $10^{-15}\ m$. In Fig. 1.9 is shown the behavior of repelling electric potential as function of distance between the reacting nuclei.
Supposing the Deuterium atom as *bullet particle* and the Tritium atom as *target particle* it's evident, from Fig. 1.9, that more the *bullet particle* gets closer to *target particle* more the Coulomb repulsion increase. However, if the *bullet particle* has sufficient energy, it can overcome the *Coulomb barrier* reaching the region where the reactants start the fusion process. The peak of the *Coulomb barrier* can be computed as follows:

$$V(r_n) = \frac{1}{4\pi\varepsilon_0}\frac{Z_1 Z_2 e^2}{r_n}.$$

where:

- ε_0 = Dielectric constant in the vacuum equals to $8{,}85418782 \cdot 10^{-12}\,\frac{C^2}{m^2 N}$;

- e = Electron charge equals to $-1{,}60217653 \cdot 10^{-19}\ C$;
- Z_1 and Z_2 = Atomic numbers of reactants;
- $r_n = 1{,}44 \cdot \left(A_1^{1/3} + A_2^{1/3}\right) \cdot 10^{-15}\ [m]$ where A_1 and A_2 are the mass number of reacting nuclei;

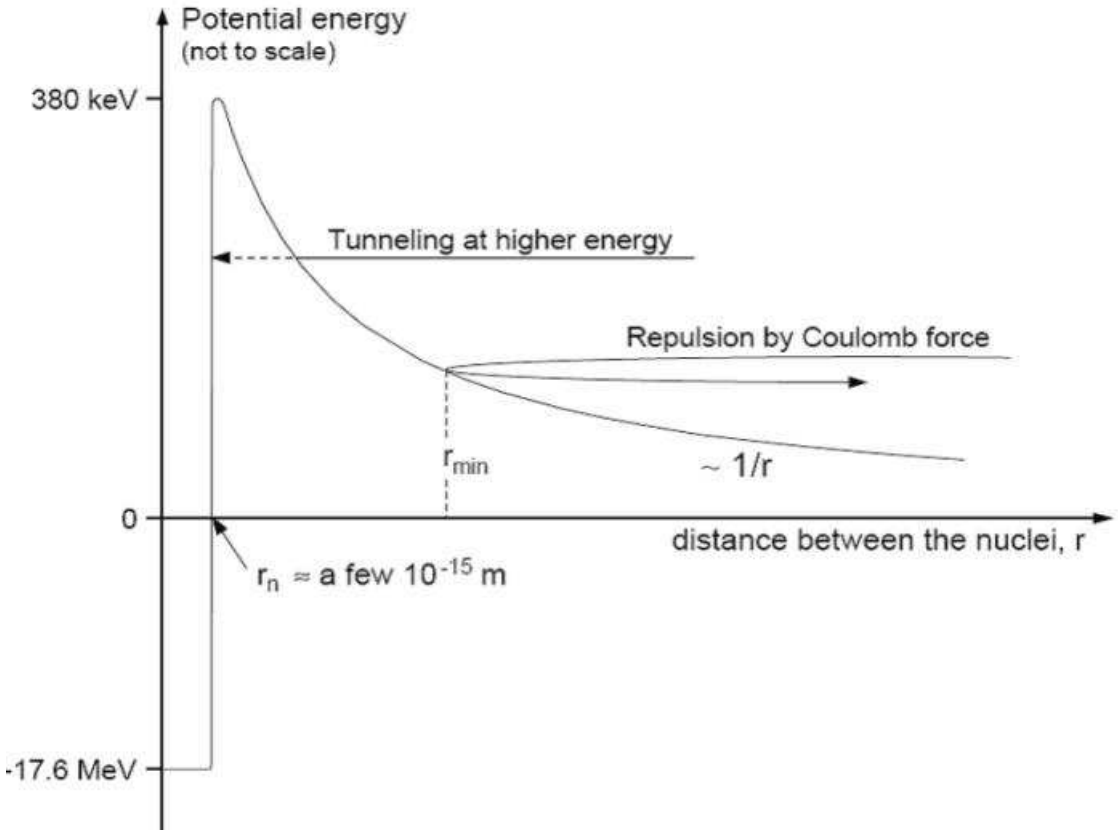

Fig. 1.9 – Repelling electric potential for Deuterium-Tritium reaction as function of distance

For Deuterium-Tritium reaction the peak value is around $0.38\ MeV\ \approx 4.4 * 10^{10}\ K$. No nuclear reactor could work whit this operative temperature, however, it's possible to overcome the *Coulomb barrier* thanks to a physical phenomenon known as *quantum tunneling*, according to which it is possible for a particle to overcome the potential barrier despite a non-sufficient kinetic energy (the author invite the interested reader to refer to specific books of quantum mechanics for a better understanding of *quantum tunneling*).

It is then possible to realize thermonuclear fusion at lower temperatures; the operating temperature of a fusion device is around 10 keV/20 keV.

1.7 The fourth state of matter: The plasma state

In order to star the nuclear fusion process, it is necessary to heat a mixture of Deuterium-Tritium at extremely high temperatures, around 100 million Kelvin degrees (more than six times the temperature of the solar core!). At such temperature, the fuel is fully ionized, and this is the reason why it is no longer called gas but instead *plasma*. In a gas at ordinary temperature, the particles are neutral; vice versa, at temperatures higher than a few eV, since the particles tend to split into their components (ions and electrons) the gas is transformed into a mixture of charged particles, called plasma, even if it still remains globally neutral.

The plasma constitutes the 99% of the matter of Universe being often defined as the fourth state of matter (substantially resorting the theories of Empedocles) and it is, also, the main constituent of the stars. Today everyone commonly deals with plasmas, e.g. the neon or the fluorescent lamps. In Fig. 1.10 are reported some examples of plasmas. The density of plasmas varies from $10^3\ m^{-3}$ (interstellar space) to $10^{33}\ m^{-3}$ (solar core).

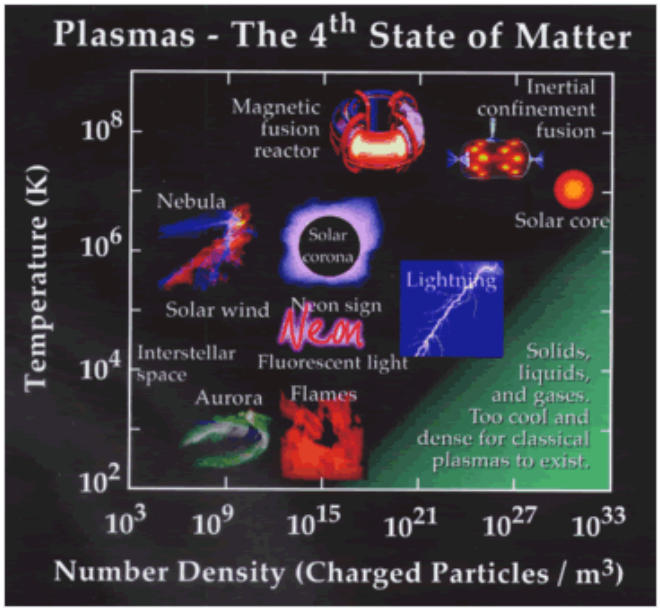

Fig. 1.10 – Examples of different types of plasmas

Since plasma is a conglomerate of neutrals, positive atoms and electrons free to move in the plasma volume, it is possible, through electromagnetic fields generated externally, not only to confine the charged particles inside the chamber but also to control the plasma current. The complex set of equations describing plasma behavior is given by the union of Maxwell equations and fluid dynamic equations. The study of the Magnetohydrodynamic theory will be faced in the following chapter of the present PhD thesis.

It is hence evident that the problem of plasma confinement is not trivial in fact, it must be kept confined in a limited space, with a confinement good enough to provide time for a sufficiently large number of reactions, allowing the energy released by the fusion reactions to compensate both the losses and the external energy. In the following an energy balance of fusion devices will be presented, stating the well-known Lawson criteria formulated by the English engineer and physicist John D. Lawson around 1955 that defines the conditions needed for a fusion reactor to reach *plasma ignition*.

1.8 Energy balance and Lawson criteria

The energy balance for the plasma can be determined by considering the energy sources that feed it and the losses that lower the temperature. In order to keep plasma in stationary conditions, the sources must balance the losses. The fusion power P_{fusion} produced by the Deuterium-Tritium reactions is given by the sum of the power of reaction products: neutrons and alpha particles (or Helium-3 nuclei).

$$P_{fusion} = P_{alpha} + P_{neut}$$

The charged alpha particles are affected by the magnetic field applied to achieve the confinement, remaining within the plasma and transferring energy to the other particles through collisions. Conversely, the neutrons not undergoing the action of the field move quickly away without being able to transfer their energy to the plasma reaching the plasma facing components and penetrating their volume. The magnetic confinement of the plasma is not perfect; therefore, particles and heat diffuse outside from the plasma core.

The losses due to heat and particles transport are considerable. If the energy produced by the reaction is not sufficient to compensate the losses, it is necessary to introduce external energy to maintain the plasma in its state. The power supplied from the outside will be indicated with $P_{external}$ whereas P_{losses} will indicate the leaks. The energy balance could be written as:

$$\frac{dW}{dt} = P_{alpha} + P_{external} - P_{losses}$$

The Left-Hand Side (LHS) term of the equations represents the plasma energy W time variation. If applied power exceeds the losses $\left(\frac{dW}{dt} > 0\right)$ the plasma energy increases, instead $\left(\frac{dW}{dt} < 0\right)$ it decreases. If the sources perfectly compensate the losses $\left(\frac{dW}{dt} = 0\right)$, the steady state regime has been reached.

Following, the definition of some plasma physics relevant parameters is provided:

- The *energy confinement time* (τ_E) is the average time taken for the energy to escape the plasma, usually defined as the total amount of energy stored in the plasma divided by the rate at which energy is lost. It can be defined as follows:

$$\tau_E = \frac{W}{P_{losses}}$$

- the *fusion energy gain factor* (Q), is the ratio of fusion power produced in a nuclear fusion reactor to the power required to maintain the plasma in steady state:

$$Q = \frac{P_{fusion}}{P_{external}}$$

Three distinct situations may occur depending on the value of the fusion energy gain factor:

- $Q < 1$: fusion power is less than the external power; this situation summarizes the current state of the art in thermonuclear fusion, whose best result was achieved at

JET with 16 MW of fusion power produced from about 24 MW input power and $Q \cong 0.7$;

- $Q = 1$: this condition, known as *breakeven*, the power developed by fusion reactions equal the additional power supplied from additional heating systems;
- $Q > 1$: fusion power is higher than the external power. At the limit, Q could become also infinite; at this condition, the fusion reaction is self-sustaining since the plasma heats itself by fusion energy without any external input ($P_{external} = 0$). In such conditions, the so-called *"plasma ignition"* takes place: the alpha particles, confined by the magnetic field, transfer their energy to the plasma allowing it to reach, after the initial heating by external sources, the ignition point; from this point the thermonuclear reaction goes on alone. Meanwhile, neutrons transfer their energy to the reactor shell, generating tritium, and transforming their kinetic energy into heat exploitable to produce electricity.

Let us now introduce the Lawson criteria [5]. It states that, in order to obtain from fusion reactions an amount of power greater than the input power, the *triple product* between plasma density (n), the confinement time (τ_E) and plasma temperature (T) has to exceed a certain threshold. In Fig. 1.11 are reported the *triple product* behaviors of several nuclear reactions as function of plasma temperature.

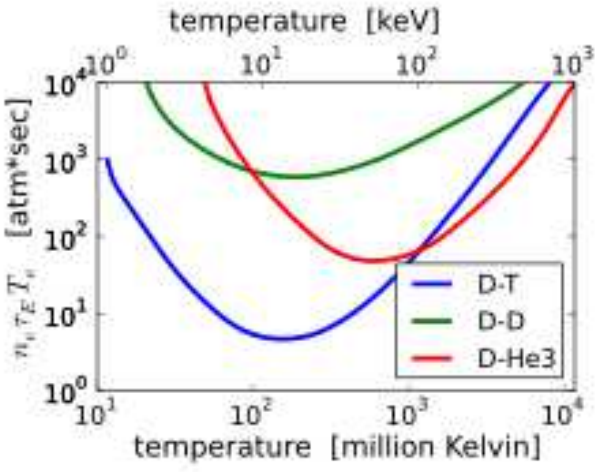

Fig. 1.11 – Triple product for different nuclear reactions

For Deuterium-Tritium reaction the minimum value of *triple product* is around $T = 20\ keV$ which leads to the following relationship:

$$n \cdot T \cdot \tau_E > 3 * 10^{21}\ keV\ s\ m^{-3}$$

According to Lawson criteria, in order to reach *plasma ignition*, the particles must be many (high density), very energetic (high temperature), and stay together for a sufficient time (high confinement time) to give a sufficient amount of fusion power. Although obtaining significant values of one of the three parameters has been achieved in present day devices, getting all three at the same time is a difficult task.

1.9 Plasma confinement techniques

The key problem in achieving thermonuclear fusion is how to confine the hot plasma. Due to the high temperature ($\approx 10^8\ K$), the plasma can not be in direct contact with any solid material, so it has to be located in vacuum. Also, high temperatures imply high pressures. The plasma tends to expand immediately, and some force is necessary to act against it. This force can take one of three forms: gravitation in stars, magnetic forces in magnetic confinement fusion reactors, or inertial as the fusion reaction may occur before the plasma starts to expand, so the plasma's inertia is keeping the material together. Let us now focus our attention on these three techniques to confine plasma:

- Gravitational confinement: A most spectacular display of fusion energy is associated with stars, where confinement comes about because of the gravitational pressure of an enormous mass. High density and temperature thereby result toward the stellar center enabling the ions to burn. While energy leakage and particle escape occur from the star's surface, the interior retains most of the reaction power and prevails against the occurrent radiation pressure through the deep gravitational potential wells, thus assuring stable confinement for times long enough to burn most of the stellar fuel. Since fusion-powered stars possess dimensions and masses of such enormity, it is evident that confinement by gravity cannot be attained in our terrestrial environment.

- Inertial confinement: Inertial confinement attempts to initiate nuclear fusion reactions by heating and compressing a fuel target, typically in the form of a Deuterium-Tritium pellet. To compress and heat the fuel, energy is delivered to the outer layer of the target using high-energy beams of laser. The heated outer layer explodes outward, producing a reaction force against the remainder of the target, accelerating it inwards, compressing the target. This process is designed to create shock waves that travel inward through the target. A sufficiently powerful set of shock waves can compress and heat the fuel at the center so much that fusion reactions occur. The energy released by these reactions will then heat the surrounding fuel, and if the heating is strong enough this could also begin to undergo fusion.
- Magnetic confinement: Since plasma is a good electric conductor, it can be confined making use of magnetic fields generated by means of external coils. The particles motion in a plasma would be unpredictable indeed, they could reach the walls of the container, cooling the plasma and inhibiting the fusion reaction. Thanks to the effect of magnetic field it is possible to trap charged particles guaranteeing plasma confinement. Now days, magnetic confinement is the most promising way to confine plasma.

The physic principle on which is based magnetic confinement is *Lorentz law* according to which, a particle of charge q moving with velocity v in the presence of a magnetic field B experiences a force:

$$F = q(v \times B)$$

Notice that the direction of the force is given by the cross product of the velocity and magnetic field. Thus, the Lorentz force will always act perpendicular to the direction of motion, causing the particle to gyrate, or move in a circle. The radius of this circle, ρ (known as *Larmor radius* or *gyroradius*), can be determined by equating the magnitude of the Lorentz force to the centripetal force as:

$$\frac{mv_{\perp}^2}{\rho} = |q|v_{\perp} B \Rightarrow \rho = \frac{mv_{\perp}}{|q|B}$$

where:

- m = mass of the particle;
- q = charge of the particle;
- B = magnetic field;
- $v_{\perp}$ = velocity component perpendicular to magnetic field;

The angular frequency of this circular motion is known as the *gyrofrequency*, or *cyclotron frequency*, and can be expressed as:

$$\omega_c = \frac{|q|B}{m}$$

Hence, from what said before, it results that the particles are forced to follow a helical path around magnetic field lines known as *cyclotronic motion* as shown in Fig. 1.12.

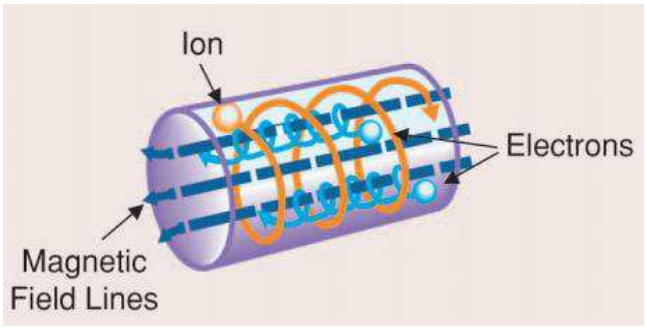

Fig. 1.12 – Cyclotronic motion of charged particles in a magnetically confined plasma

Analyzing Larmor radius expression it comes out that to a stronger the magnetic field corresponds a smaller Larmor radius which means a particle very close to magnetic field line. Moreover, the electrons, much lighter than the ions, have a much smaller Larmor

radius for the same energy (as shown in Fig. 1.12). Finally, very energetic particles have a much larger Larmor radius than low energy particles and are therefore more difficult to confine. The Larmor radius may typically vary from several millimeters for not very energetic particles with an intense magnetic field to tens of centimeters for very energetic particles.

The confinement solution thus consists in closing the magnetic field line on itself to trap the particle. This is the concept on which *tokamak* devices (axisymmetric toroidal devices) are based. An exhaustive analysis of these devices will be performed in Chapter 3 of the present work.

Chapter 2: MHD theory

"[...] for fundamental work and discoveries in magneto-hydrodynamic theory with fruitful applications in different parts of plasma physics "

Rationale for Nobel Prize in Physics given to Hannes Alfvén in 1970

In this chapter, the Magnetohydrodynamic theory will be introduced. Starting from Maxwell's and fluid dynamic equations which compose the *MHD model* we will derive the well-kwon Grad-Shafranov equation for toroidal axisymmetric geometries. In order to solve numerically Grad-Shafranov equation, the CREATE-NL+, a free boundary plasma equilibrium solver, will be presented.

2.1 Equations of MHD model

Magnetohydrodynamic (usually abbreviated whit MHD) is the study of the magnetic properties of electrically conducting fluids. Examples of such magnetofluids include plasmas, liquid metals, salt water, and electrolytes. The word "magnetohydro-dynamics" is derived from the words *magneto-* which mean magnetic, *hydro-* meaning water and *dynamics-* which refers to something in movement.

The field of MHD was initiated by Hannes Alfvén, for which he received the Nobel Prize in Physics in 1970.The fundamental concept behind MHD is that magnetic fields can induce currents in a moving conductive fluid, which in turn polarizes the fluid and reciprocally changes the magnetic field itself. The set of equations that describe MHD are a combination of the Navier–Stokes equations of fluid dynamics and Maxwell's equations of electromagnetism. Before introducing the complex MHD equations set it's worth to mention the main assumptions usually adopted in MHD theory [6],[7]:

- Displacement currents can be neglected in Maxwell's equations. In order to verify this assumption, it is required that the electromagnetic waves of interest have

phase velocities much slower than the speed of light $\frac{\omega}{k} \ll c$ and that the characteristic thermal velocities be non-relativistic;

- Net charges can be neglected. This assumption restricts attention to plasma behavior whose characteristic frequency is much less than the electron plasma frequency $\omega \ll \omega_{pe}$, $\omega_{pe} = \sqrt{\frac{n_o e^2}{m_e \varepsilon_0}}$. This hypothesis leads to the quasi-neutrality of the plasma:

$$n_e = n_i = n$$

where we indicated with n_e and n_i electron and ion density respectively;

- Electron mass can be neglected. This requires that the frequencies of interest are small compared to the response of the electrons;

The set of electromagnetic equations that constitute MHD model are:

(2.1) $\nabla \times \boldsymbol{H} = \boldsymbol{J}$

(2.2) $\nabla \times \boldsymbol{E} = -\frac{\partial \boldsymbol{B}}{\partial t}$

(2.3) $\nabla \cdot \boldsymbol{B} = 0$

where

- $\boldsymbol{J}$ = Current density;
- $\boldsymbol{B}$ = Magnetic flux density;
- $\boldsymbol{E}$ = Electric field;
- $\boldsymbol{H}$ = Magnetic field;

Equations (2.1) is Ampere's law in which, according to the assumptions previously stated, the displacement currents $\frac{\partial(\varepsilon \boldsymbol{E})}{\partial t}$ have been neglected. Equations (2.2) and (2.3) are Faraday-Neumann law and Gauss's law respectively.

The two following constitutive laws must be coupled with the previous equations:

(2.5) $\boldsymbol{B} = \mu_0 \boldsymbol{H}$;

(2.6) $\bar{\bar{\eta}}\boldsymbol{J} = \boldsymbol{E} + \boldsymbol{v} \times \boldsymbol{B} + \boldsymbol{E_{ext}}$;

Equation (2.5) is the magnetic constitutive relation, linear in vacuum and in linear media such as air and plasma where $\mu = \mu_0$, nonlinear in ferromagnetic media where μ is a function of $\boldsymbol{B}$. Equation (2.6) is the general form of Ohm's law where $\bar{\bar{\eta}}$ represents plasma resistance and $\boldsymbol{E_{ext}}$ represents the electric field generated by means of external sources and $\boldsymbol{v}$ is particle speed. Assuming plasma as a *perfect electric conductor* ($\bar{\bar{\eta}} = 0$ or $\sigma = \infty$, where σ is plasma electric conductivity) we obtain the *ideal MHD model*. In this case, the MHD model requires that magnetic field lines are frozen into the plasma and have to move along with it: this result is also known as Alfvén's Theorem.To close the MHD model, let us now introduce the fluid dynamics equations. In order to have an exhaustive fluid description of plasmas, starting from Boltzmann equation, the moments corresponding to mass, momentum and energy should be derived obtaining the well-known *two fluid model* description. However, it is possible to simplify the equations of two fluid model making use of the assumptions previously stated introducing the *single fluid model*. Let us now introduce the fluid variables of interest which are: the mass density ρ, the fluid velocity $\boldsymbol{v}$ and current density $\boldsymbol{J}$. The definition of the fluid variables previously introduced is presented in the following:

(2.7) $\rho = m_e n_e + m_i n_i \approx m_i n_i$ (Since $m_e \ll m_i$);

(2.8) $\boldsymbol{v} = \frac{1}{\rho}\left(m_i n_i \boldsymbol{v_i} + m_e n_e \boldsymbol{v_e}\right) \approx \boldsymbol{v_i}$ (According to (2.7));

(2.9) $\boldsymbol{J} = en(\boldsymbol{v_i} - \boldsymbol{v_e}) \approx en(\boldsymbol{v} - \boldsymbol{v_e})$ (According to (2.8));

The final definitions required are the total pressure p and temperature T:

(2.10) $p = nT = p_e + p_i$;

(2.11) $T = T_e + T_i$;

Once introduced all the fluid variables of interest let us now present the set of fluid dynamics equations in order to close the MHD model:

(2.12) $\frac{d\rho}{dt} + \rho \nabla \cdot \boldsymbol{v} = 0;$

(2.13) $\rho \frac{d\boldsymbol{v}}{dt} = -\nabla p + \boldsymbol{J} \times \boldsymbol{B};$

(2.14) $\frac{d}{dt}\frac{p}{\rho^{\gamma}} = 0;$

The operator $\frac{d}{dt}(\cdot) = \frac{\partial(\cdot)}{\partial t} + \boldsymbol{v} \cdot \nabla(\cdot)$ represents the *material derivative* which describes the time rate of change of some physical quantity (like heat or momentum) of a material element that is subjected to a space-and-time-dependent macroscopic velocity field variations of that physical quantity. The material derivative can serve as a link between Eulerian and Lagrangian descriptions of continuum deformation.

Equation (2.12) is the mass continuity equation which is approximately verified in a plasma since in a fusion reactor the energy is produced exploiting the mass defect therefore, the mass intentionally does not have to be conserved. If we compute the material derivative in equation (2.12) we get the term $\boldsymbol{v} \cdot \nabla \rho$ which represents the effect of the expansion while the term $\rho \nabla \cdot \boldsymbol{v}$ represents the effect of convection.

Equation (2.13) is the momentum conservation and states that the variation of plasma momentum density is due to the overall force density which is the sum of electromagnetic force density ($\boldsymbol{J} \times \boldsymbol{B}$) and pressure gradient ($-\nabla p$).

Equation (2.14) is the adiabatic equation of state (the term γ is the ration between the specific heats), supposing no heat exchanges and assuming that the processes take place rapidly so that the entropy is conserved.

2.2 Plasma equilibrium problem

Plasma equilibrium problem refers to the solution of ideal MHD model equations under the following conditions:

- Stationary conditions: $\frac{\partial}{\partial t} = 0;$
- Static conditions: $\boldsymbol{v} = \boldsymbol{0};$

Under these hypotheses the equilibrium problem can be expressed though the following set of equations:

(2.15) $\nabla p = \boldsymbol{J} \times \boldsymbol{B}$;

(2.16) $\nabla \cdot \boldsymbol{B} = 0$;

(2.17) $\nabla \times \boldsymbol{H} = \boldsymbol{J}$;

According to equation (2.15) at equilibrium condition, pressure gradient tends to balance the effect of electromagnetic force density (Fig. 2.1). Furthermore, performing a scalar multiplication of equation (2.15) with $\boldsymbol{J}$ and $\boldsymbol{B}$ we have:

(2.18) $\boldsymbol{J} \cdot \nabla p = 0$;

(2.19) $\boldsymbol{B} \cdot \nabla p = 0$;

Equations (2.18) and (2.19) state that magnetic field lines and current field lines lie on isobaric surfaces as shown in Fig. 2.1

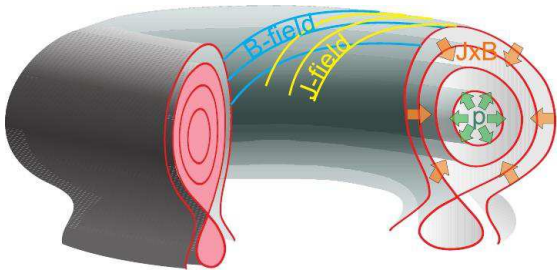

Fig. 2. 1 – Isobaric surfaces in a plasma equilibrium configuration

The ideal MHD model presented represents an approximate model to describe all the phenomena which take place in a plasma. It is also applied to complex geometries for which more sophisticated models cannot be applied. However, for toroidal axisymmetric geometries (such as a tokamak device), the precision of the model above introduced is very accurate and provides reliable predictions for what concerns plasma behavior. In the following paragraph, the equilibrium problem for axisymmetric geometries will be tackled, obtaining the well-known *Grad-Shafranov equation*.

2.3 Equilibrium problem in toroidal axisymmetric geometries

In order to study plasma equilibrium problem in axisymmetric toroidal geometries such as tokamak devices, a cylindrical reference system (Fig. 2.2) can be used. Coordinates r and z are known as *poloidal coordinates* while ϕ coordinate is called *toroidal coordinate*. Axisymmetric hypothesis implies that all variables depends only on poloidal coordinates:

$$\frac{\partial}{\partial \phi} = 0$$

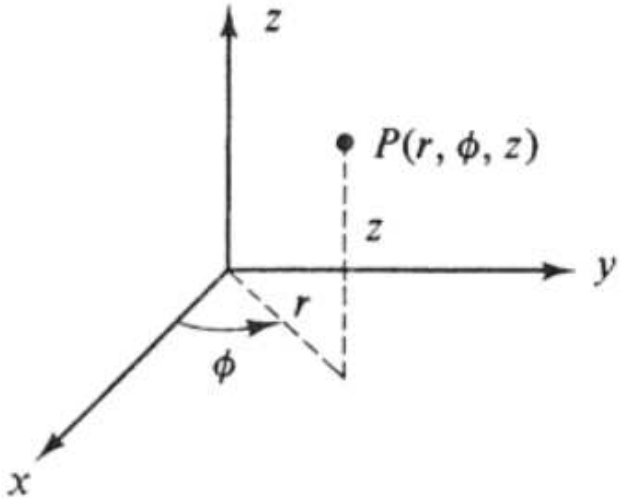

Fig. 2.2 – Cylindrical coordinate system

Let us now introduce the *poloidal magnetic flux* $\Psi(r,z)$ and the *poloidal current* $I_{pol}(r,z)$ respectively defined as follows:

- Poloidal magnetic flux $\Psi(r,z)$ is defined as the poloidal flux linked with the circumference obtained by revolving the (r,z) around the z-axis. According to the previous definition, the expression of poloidal magnetic flux is: $\Psi(r,z) = \int_0^r B_z(r',z')2\pi r' dr'$. In order to simplify future equations *poloidal magnetic flux per radian* $\psi(r,z) = \frac{\Psi(r,z)}{2\pi}$ is introduced;

- Poloidal current $I_{pol}(r,z)$ is defined as the poloidal current linked with the circumference obtained by revolving the (r,z) around the z-axis. Expression of poloidal current can be easily derived making use of: Ampere law's [equation (2.17)], magnetic constitutive relation [equation (2.5)] and Stokes theorem $I_{pol}(r,z) = \frac{2\pi r B_\phi}{\mu_0}$. In order to simplify future equations *poloidal current function* $f(r,z) = \frac{\mu_0 I_{pol}(r,z)}{2\pi} = rB_\phi$ is introduced.

Making use of the previous definitions it is possible the obtain the expressions of radial and vertical coordinates of magnetic field $\boldsymbol{B}$ and current density $\boldsymbol{J}$.

Indeed, the infinitesimal flux linked with the circular crown having r and $r+dr$ as internal and external radius respectively (Fig. 2.3a) is:

(2.20) $d\Psi = B_z 2\pi r dr \Rightarrow B_z = \frac{1}{r}\frac{\partial \psi}{\partial r}$;

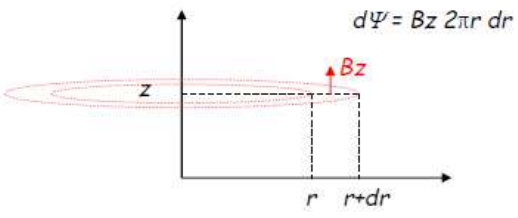

Fig. 2.3a – Vertical coordinate of magnetic field [8]

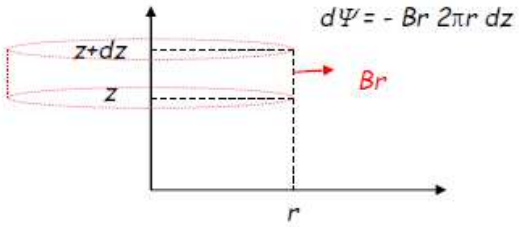

Fig. 2.3b – Radial coordinate of magnetic field [8]

Making use of divergence free condition of magnetic field $\boldsymbol{B}$, it is possible to calculate the flux variation which cross the side surface of an infinitesimal cylinder indicating with dz and r the height of the cylinder and the radius of the basis circumference (Fig. 2.3b) respectively:

(2.21) $d\Psi = -B_r 2\pi r dz \Rightarrow B_r = -\frac{1}{r}\frac{\partial \psi}{\partial z}$;

For what concerns current density $\boldsymbol{J}$, it is possible to apply a similar procedure in order to obtain vertical and radial components.

Calculating the current density for an infinitesimal circular crown (Fig. 2.4a) and computing the current density crossing the side surface of an infinitesimal cylinder (Fig. 2.4b) We get:

(2.22) $d\mathrm{I}_{\mathrm{pol}} = J_z 2\pi r dr \Rightarrow J_z = \frac{1}{r}\frac{\partial(f/\mu_0)}{\partial r}$;

(2.23) $d\mathrm{I}_{\mathrm{pol}} = -J_r 2\pi r dz \Rightarrow J_r = -\frac{1}{r}\frac{\partial\left(\frac{f}{\mu_0}\right)}{\partial z}$;

In Equations (2.22) and (2.23) the definition of poloidal current functions has been used. Therefore, the total magnetic field can be expressed as the sum between the poloidal field $B_{pol} = \sqrt{B_r^2 + B_z^2}$ and toroidal field B_ϕ:

(2.24) $\boldsymbol{B} = \frac{1}{r}\nabla\psi \times \boldsymbol{i}_\phi + \frac{f}{r}\boldsymbol{i}_\phi$;

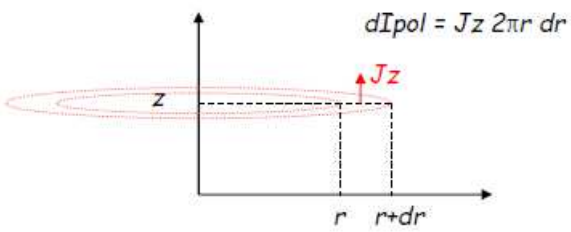

Fig. 2.4a – Vertical coordinate of current density [8]

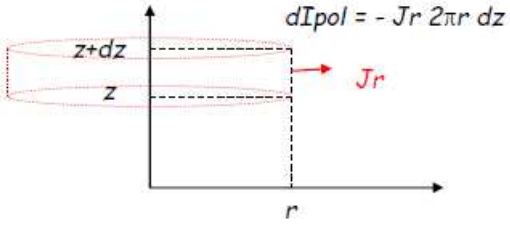

Fig. 2.4b – Radial coordinate of current density [8]

Where We indicated with $\boldsymbol{i}_\phi$ the vector unit for toroidal direction. Similarly, the current density is the sum between the poloidal component $\boldsymbol{J}_{pol} = \sqrt{J_r^2 + J_z^2}$ and the toroidal component J_ϕ. It is possible to have an expression of the toroidal component making use of Ampere's law:

(2.25) $J_\phi = \nabla \times \left(\frac{\boldsymbol{B}}{\mu}\right) \cdot \boldsymbol{i}_\phi = -\frac{\partial}{\partial r}\left(\frac{1}{\mu r}\frac{\partial\psi}{\partial r}\right) - \frac{\partial}{\partial z}\left(\frac{1}{\mu r}\frac{\partial\psi}{\partial z}\right)$;

Let us now introduce the *Shafranov operator* (elliptical second order operator):

(2.26) $\Delta^*\psi = r^2\nabla\cdot\left(\frac{\nabla\psi}{\mu_r r^2}\right) = r\frac{\partial}{\partial r}\left(\frac{1}{\mu_r r}\frac{\partial\psi}{\partial r}\right)+\frac{\partial}{\partial z}\left(\frac{1}{\mu_r r}\frac{\partial\psi}{\partial z}\right) = -\mu_0 r J_\phi;$

The final expression for total current density $\boldsymbol{J}$ is:

(2.27) $\boldsymbol{J} = \boldsymbol{J}_{pol} + J_\phi \boldsymbol{i}_\phi = \frac{1}{r}\nabla\left(\frac{f}{\mu_0}\right)\times\boldsymbol{i}_\phi - \frac{\Delta^*\psi}{\mu_0 r}\boldsymbol{i}_\phi;$

Performing a scalar multiplication of equations (2.24) and (2.27) for ∇p (under the axisymmetric hypothesis we have $\frac{\partial p}{\partial\phi} = 0$) We get:

(2.28) $\boldsymbol{B}\cdot\nabla p = \frac{1}{r}\nabla\psi\cdot\boldsymbol{i}_\phi\cdot\nabla p = \frac{1}{r}\boldsymbol{i}_\phi\cdot\nabla p\times\nabla\psi = 0;$ [According to Eq. (2.18)]

(2.29) $\boldsymbol{J}\cdot\nabla p = \frac{1}{r}\nabla\left(\frac{f}{\mu_0}\right)\times\boldsymbol{i}_\phi\cdot\nabla p = \frac{1}{r\mu_0} i_\phi\cdot\nabla p\times\nabla f = 0$; [According to Eq. (2.19)]

According to equations (2.28) and (2.29):

(2.30) $\nabla p\times\nabla\psi = \nabla p\times\nabla f \Rightarrow \nabla\psi\times\nabla f = 0 \Rightarrow \nabla p\,//\,\nabla\psi\,//\,\nabla f$

Since the gradients of ψ, p and f are parallel it turns out that $p = p(\psi)$ and $f = f(\psi)$. Therefore:

(2.31) $\nabla p = \frac{dp}{d\psi}\nabla\psi;$

(2.32) $\nabla f = \frac{df}{d\psi}\nabla\psi;$

At plasma equilibrium condition the plasma momentum balance [equation (2.15)] can be rewritten making use of equations (2.24) and (2.27) as follow:

(2.33) $\boldsymbol{J}\times\boldsymbol{B} = \nabla p \Rightarrow -\frac{\Delta^*\psi}{\mu_0 r^2}\nabla\psi - \frac{f}{\mu_0 r^2}\nabla f = \nabla p;$

According to equations (2.31) and (2.32) equilibrium equation (2.33) can be recast as:

(2.34) $\Delta^*\psi = -f\frac{df}{d\psi} - \mu_0 r^2\frac{dp}{d\psi};$

Equations (2.34) is the well-known Grad-Shafranov equation [9] which describes the equilibrium for an isotropic plasma given a particular choice of p and f, which also set

boundary conditions at the coordinate frame origin $r = 0$ and at infinity. This formulation can be extended to various domains, where magnetic flux is present. To begin with, it can be observed that, according to Poisson's equation, the term $\Delta^*\psi$ is equal to zero in the vacuum region. Moreover, $\Delta^*\psi$ is proportional to the toroidal current density $\boldsymbol{J}_{ext}$ in the external conductors and coils. To summarize, the following PDE (Partial Differential Equation) problem has been defined:

$$\Delta^*\psi = \begin{cases} -f\frac{df}{d\psi} - \mu_0 r^2 \frac{dp}{d\psi} & (r,z) \in \Omega_p \\ -\mu_0 r \boldsymbol{J}_{ext} & (r,z) \in \Omega_i \ \forall i = 1 \dots n \\ 0 & (r,z) \in \Omega_a \cup \Omega_v \end{cases} \tag{2.35}$$

with the following initial and boundary conditions:

$$\begin{cases} \psi(r,z,t)|_{t=0} = \psi_0(r,z) \\ \psi(r,z,t)|_{r=0} = 0 \\ \lim_{r^2+z^2} \psi(r,z,t) = 0 \end{cases} . \tag{2.36}$$

According to Fig. 2.5 we indicated:

- Ω_p: Plasma region;
- Ω_c: Conducting structures region;
- Ω_i $(i = 1 \dots n)$: Poloidal field coils region;
- Ω_a: Air region;
- Ω_v: Vacuum region.

From an analysis problem (2.35) it turns out that the problem itself results to be ill posed since, in order to calculate the poloidal magnetic flux ψ at an arbitrary time instant t, the knowledge of poloidal current function f and pressure p is mandatory but both f and p are function of ψ and their spatial dependence with ψ is not known a-priori.

2.4 Free/fixed boundary plasma equilibrium problem

According to problem equations (2.35) the model describing the electromagnetic

behavior of a tokamak device in absence of plasma results to be linear. The presence of plasma inside the chamber makes the model nonlinear. The sources of nonlinearities are basically two: plasma current density, which is function of ψ, and *plasma boundary* $\partial\Omega_p$ which is unknown.

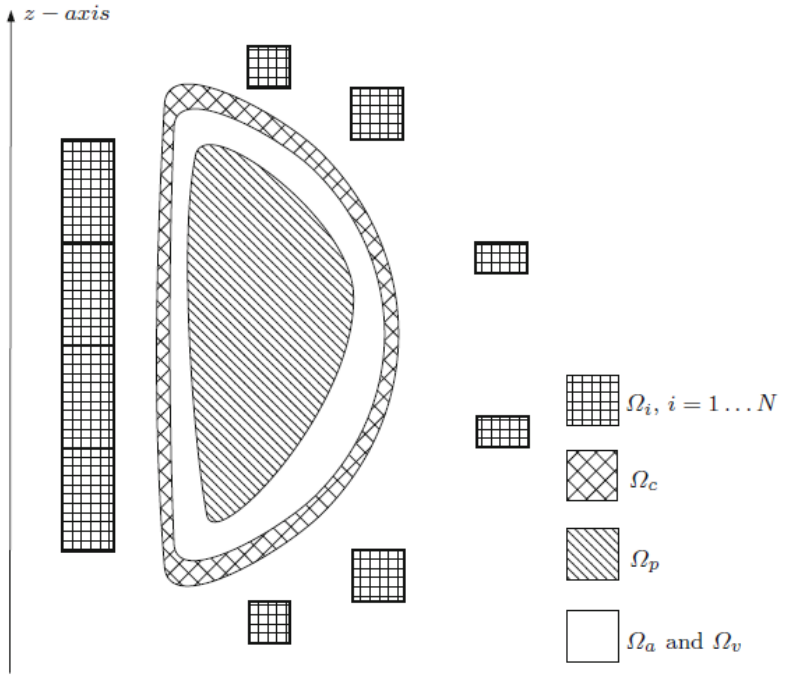

Fig. 2.5 – The poloidal cross-section of a tokamak machine can be partitioned into regions occupied by the plasma (Ω_p), by the conducting structure (Ω_c), by the poloidal field coils ($\Omega_i\ \forall\ i=1\dots n$), by the air ($\Omega_a$) and by the vacuum ($\Omega_v$) [52]

Plasma boundary can be defined as the largest poloidal flux surface closed inside the vacuum vessel (blue solid lines in Fig. 2.5) and is determined by a numerical calculation. Particles inside plasma boundary are confined and describe an helicoidal path around magnetic field lines as described in Section 1.9. Topologically, the boundary is either the outermost flux contour not intersecting any solid object, or it is a separatrix, that is, a surface containing an X point, which is a point at which the poloidal magnetic field is zero. Since the plasma boundary is not known a priori, problem (2.35) is also note as *free boundary problem* because its solution implies also the definition of plasma boundary $\partial\Omega_p$. Inversely, a *fixed boundary problem* consists in defining the combination of external currents $\boldsymbol{J}_{ext}$ in order to have a desired plasma boundary $\partial\Omega_p$. In this case, Grad-Shafranov equation is used as constraint. To solve problem free boundary problem (2.35) iterative procedures based on finite difference method or finite elements method (FEM) can be used. In particular, using FEM, it is possible to convert the nonlinear PDE problem

into an algebraic nonlinear set of equations that can be solved using numerical methods such as Newton-Raphson method or Picard's method. In the following Section, the CREATE-NL+ code, a numerical FEM free boundary plasma equilibrium solver, will be presented.

2.5 CREATE-NL+ code

CREATE-NL+ code [37], implemented in Matlab, is a FEM code simulating the time evolution of 2D axisymmetric plasmas in toroidal nuclear fusion devices in the presence of current and/or voltage driven active circuits, currents induced in the passive conductors, and iron components. The first version of CREATE-NL code was developed in 2002 with the objective of simulating JET plasmas in order to design and test innovative multivariable controllers like the XSC [10], although never systematically presented to the scientific community. Since that date, it was used for several activities including vertical stabilization studies on JET and ITER, shape controllability analyses on ITER, EAST, MAST, ASDEX-U, TCV, FTU, preliminary studies on FAST, DTT and DEMO. The code requires as inputs a set of machine configuration data (geometry, active coils and passive structures configuration, first wall definition, etc.) and a set of input signals related to the plasma profiles and PF coils currents/voltages. PF coils voltages can be then generated by a feedback control law, whereas plasma related quantities can be generated by a detailed transport simulation code including heating and current drive systems (see Fig. 2.6). The CREATE-NL numerical solver was formulated to deal with a different number of equations and variables since the core solve is based on a pseudo-inverse procedure. In facts CREATE-NL was used also to solve shape and profile identification problems.

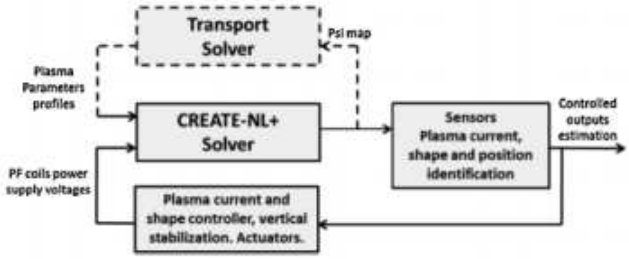

Fig. 2.6 –The CREATE-NL+ solver in interaction with a feedback control block, a transport equation solver and a plasma shape, position and current identification block

From a numerical point of view, the increased robustness of CREATE-NL+ is guaranteed by a robust numerical procedure for the plasma boundary search, and by a reliable numerical solution of the nonlinear algebraic equations arising from the FEM formulation. These equations are solved with a Newton-Raphson Method approach where the calculation and inversion of the Jacobian matrix plays an important role both for the computational time and the numerical stability. Let us now consider the Grad-Shafranov equation:

$$(2.35)\ \Delta^{*}\psi = \begin{cases} -f\frac{df}{d\psi} - \mu_0 r^2 \frac{dp}{d\psi} & (r,z) \in \Omega_p \\ -\mu_0 r \boldsymbol{J}_{ext} & (r,z) \in \Omega_c \\ 0 & \text{elsewhere} \end{cases}$$

With the and boundary conditions:

$$(2.36)\begin{cases} \psi(r,z,t)|_{t=0} = \psi_0(r,z) \\ \psi(r,z,t)|_{r=0} = 0 \\ \lim_{r^2+z^2} \psi(r,z,t) = 0 \end{cases}$$

The above equations are used to calculate the poloidal flux function at time t provided that the plasma boundary can be determined, the toroidal current density in the PF coils is known, and the functions $p(\psi)$ and $f(\psi)$ are assigned within the plasma. Under simplifying assumptions, functions $p(\psi)$ and $f(\psi)$ can be expressed in terms of few plasma parameters, for example poloidal beta β_p and internal inductance l_i which can be defined as follows:

$$(2.37)\quad \beta_p = \frac{4}{\mu_0 r_c I_p^2}\int_{V_P} p\, dV;$$

$$(2.38)\quad l_i = \frac{4}{\mu_0 r_c I_p^2}\int_{V_P} \frac{\|\boldsymbol{B}_{pol}\|^2}{2\mu_0} dV;$$

Where r_c is radial coordinate of plasma centroid, V_P is plasma volume obtained by means of a toroidal revolution of Ω_P domain and I_P is plasma current defined as:

$$(2.39)\quad I_p = \int_{\Omega_P} J_\phi\, dS;$$

Poloidal beta can be seen as a measure of the efficiency of plasma confinement since it is computed as the ration between the pressure energy and the magnetic energy confined inside plasma volume. Internal inductance is a dimensionless parameter and it is related the magnetic energy stored inside plasma region. It characterizes how a current density profile is peaked along radial direction. In general, much bigger is the value of l_i, more the current profile is spiked.

$\boldsymbol{J}_{ext}$ can be expressed as a linear combination of the circuit currents. Therefore, the magnetic flux and the plasma configuration can be determined when prescribing the vector of currents $\boldsymbol{I}$ (including poloidal field coils, passive structures and plasma currents) along with functions $p(\psi)$ and $f(\psi)$. The time evolution of these currents is given by plasma-circuit equation:

(2.40) $\dot{\Psi} + RI = V - L_E \dot{w}$;

where:

- $\Psi = LI$ is the vector of magnetic fluxes linked with the circuits;
- L is the mutual inductance matrix among active coils, passive structures and plasma;
- L_E is the disturbances matrix used to take into account possible profile variations;
- $w = [\beta_p \; l_i]$;
- R is the resistance matrix;
- V is the vector of applied voltages.

The flux vector Ψ is defined as the integral of the flux function over the conductor regions. The relationship between the toroidal current density in the control circuits and the poloidal flux can be obtained from Faraday's and Ohm's laws. In principle, the active powered coils and the passive conductors can be treated in the same way. The only difference is in the applied voltage, which is zero in the passive conductors. It can be shown that:

(2.41) $\boldsymbol{J}_{ext} = -\frac{\sigma}{r}\frac{\partial \psi}{\partial t} + \frac{\sigma}{2\pi r}u$;

Where u is the voltage applied to the coils. Equation (2.41) must then be integrated over the conductor regions.

In order to recast the PDE equilibrium problem to a finite dimensional problem a first order FEM is adopted. Plasma current density can be assigned in terms of $p(\psi)$ and $f(\psi)$ functions or described by means of a finite number of parameters using the following relationships:

(2.42) $\boldsymbol{J}_{pl}(r,\psi) = r\sum_{k=1}^{M_a} a_k \chi_{ak}(\bar{\psi},\alpha) + \left(\frac{1}{r}\right)\sum_{k=1}^{M_b} b_k \chi_{bk}(\bar{\psi},\alpha)$;

(2.43) $\bar{\psi} = \frac{\psi - \psi_{axis}}{\psi_{boundary} - \psi_{axis}}$;

where χ are basis function of the normalized flux and of a parameter vector α. In this case additional equations are needed to close the problem, e.g. β_p, l_i and plasma current fixed to a prescribed value. FEM approach finally requires the solution of a nonlinear set of equations in the form:

(2.44) $\boldsymbol{F}(\boldsymbol{\psi},\boldsymbol{\pi}) = \boldsymbol{F}(\boldsymbol{x_1},\boldsymbol{x_2}) = 0$;

in the n_1 unknowns $\boldsymbol{\psi}$, which is the vector of fluxes in the spatial discretization nodes, and n_2 unknowns $\boldsymbol{\pi} = [\boldsymbol{I}^T\ \boldsymbol{\alpha}^T]^T$, which is a vector of variables including coil currents and profile parameters. It is worth to notice that currents become unknowns if circuits are voltage driven.

Problem (2.44) is solved with an iterative Newton based method where boundary conditions in (2.36) are treated via a suitable coupling with boundary integral equations [11]. The calculation and inversion of the $\boldsymbol{F}$ Jacobian matrix is the core of the solver. The candidate solution update in the iterative algorithm is:

(2.45) $\boldsymbol{x}^{k+1} = \boldsymbol{x}^k - \left(\frac{\partial \boldsymbol{F}(\boldsymbol{x}^k)}{\partial \boldsymbol{x}}\right)^{-1} \boldsymbol{F}(\boldsymbol{x}^k)$;

Where $\boldsymbol{x} = [\boldsymbol{\psi}^T\ \boldsymbol{\pi}^T]^T$ and k denotes the iteration step.

Once computed plasma equilibrium, it is possible, by means of CREATE-L code [12], to produce a linearized open loop plasma response model through a linearization procedure around the equilibrium point found. Plasma linearized model can be used for the design of the plasma current, position and shape control system or for the optimization of PF coil system as will be shown in Section 4.3.

The derivation of linearized model can be obtained from plasma-circuit equation (2.40). Choosing the vector of the currents as state variables $x(t) = I$ and the applied voltages as inputs $u(t) = V$ We obtain:

(2.46) $\dot{x}(t) = Ax(t) + Bu(t) + E\dot{w}(t)$;

Where:

- $A = L^{-1}R$; $B = L^{-1}$; $E = L^{-1}L_E$;

To complete the state space model (2.46) the output equation must be introduced:

(2.47) $y(t) = Cx(t) + Du(t) + Fw(t)$;

The output variables contained in $y(t)$ include plasma centroid position, boundary flux, plasma current, gaps and other physical quantities that can be used to design new controllers or to optimize the performances of existing control system.

Chapter 3: Overview on tokamak devices

"We say that we will put the sun into a box. The idea is great. The problem is, we don't know how to make the box."

Pierre-Gilles de Gennes, Nobel laureate in physics in 1991

In this chapter a general overview on tokamak devices will be provided. We will start introducing the general structure of a tokamak reactor illustrating the main components of the machine and how the plasma is magnetically confined. Particular emphasis will be dedicated to additional heating systems and magnetic diagnostics which are typically employed. Finally, we will introduce the three devices on which the research activity has been focused: the Chinese tokamak EAST site in Hefei, P.R. China and the future generation tokamaks DTT and DEMO.

3.1 Structure of a tokamak device

A tokamak device, from the Russian acronym TOroidalnaya KAmera ee MAgnitnaya Katushka ("тороидальная камера с магнитными катушками") which means "toroidal chamber with magnetic coils" is nowadays the most promising configuration for plasma magnetic confinement which is realized by means of a superposition of a poloidal and a toroidal magnetic field.

In Fig. 3.1 it has been reported the typical structure of a tokamak (ITER structure has been reported) in the poloidal plane, highlighting the main components of the device.

Let us now focus on the analysis of the main components of a tokamak device:

- Central Solenoid: Central Solenoid (in the following CS) is the winding located in the center of the tokamak, more precisely on the torus axis. The CS main task is to develop plasma current through transformer effect where the CS plays the role of primary coil while the plasma acts like secondary coil;

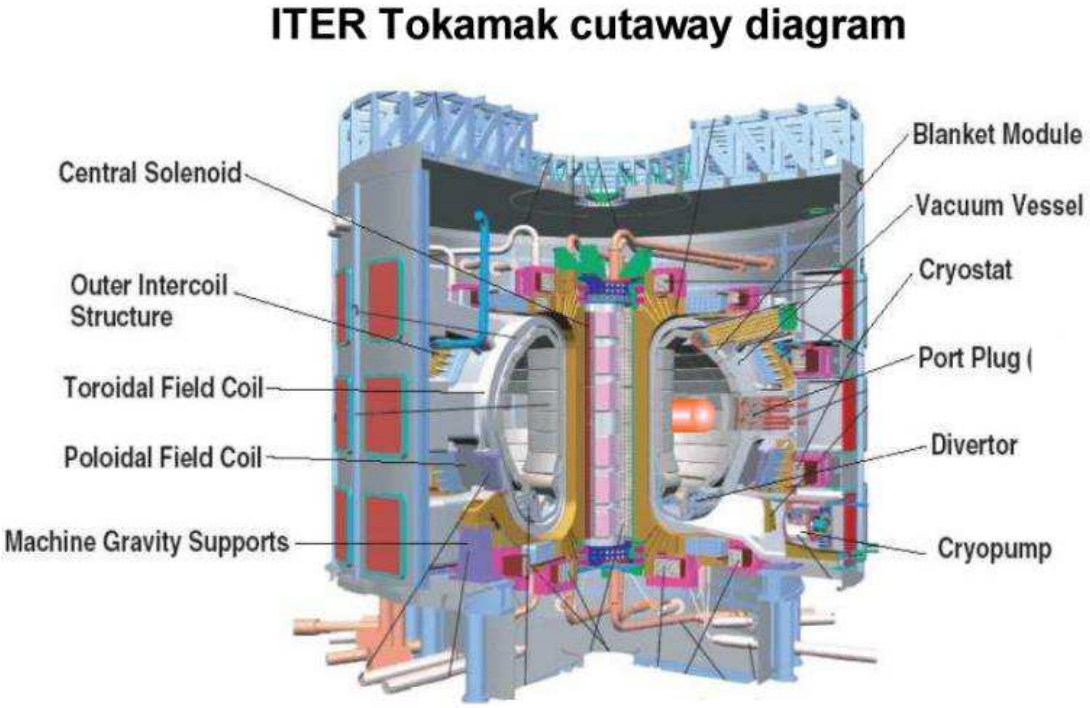

Fig. 3.1 – The structure of a Tokamak device. In this figure, ITER structure has been reported

- Toroidal Field Coils (TFCs): TFC's task is to generate the toroidal magnetic field component in order to confine particles inside the chamber;
- Poloidal Field Coils (PFCs): PFCs are windings that surround toroidally the Tokamak. Electromagnetic control actions are implemented regulating opportunely the current in these coils;
- Cryostat: Cryostat is a vacuum tight container which surround the tokamak machine. Its task it to provide a vacuum insulation environment for the magnets;
- Vacuum Vessel: Vacuum Vessel is a hermetically sealed steel container that houses the fusion reactions and acts as a first safety containment barrier. The Vacuum Vessel provides a high-vacuum environment for the plasma, improves radiation shielding and plasma stability, acts as the primary confinement barrier for radioactivity, and provides support for in-vessel components such as the blanket and the divertor. The heat generated during operation can be removed by means of cooling fluids circulating through vessel's wall.

- Blanket: It is the layer which cover the first wall and the divertor. The blanket has a double task: absorbing kinetic energy of neutrons developed in fusion reactions and Tritium production (*breeding blanket*).
- Divertor: Situated at the bottom of the Vacuum Vessel, the divertor's goal is the extraction of heat and ash produced by the fusion reaction, minimizing plasma contamination, and protecting the surrounding walls from thermal and neutronic loads.

3.2 Plasma confinement in a tokamak

Plasma confinement in a tokamak device is realized by means of a superposition of a toroidal magnetic field, generated through TFCs, and a poloidal magnetic field generated by plasma current itself and PFCs. It is possible to obtain a simple expression of the toroidal field B_{tor} considering a torus on which N turns are wound, as shown in Fig. 3.2. If I is the current flowing through them, by applying the Ampère's law to the generic concentric circumference with r radius, chosen as a closed line, and making use of Stoke's theorem we have:

(3.1) $B_{tor} 2\pi r = \mu_0 NI \Rightarrow B_{tor} = \frac{\mu_0 NI}{2\pi r}$

The toroidal magnetic field B_{tor} is inversely proportional to the distance r from the center of the torus. According to what said in Section 1.9, plasma charged particles, under the effect of toroidal field which lead to Lorentz force, are hence forced to describe a helical path around toroidal magnetic field lines. However, the toroidal field itself it is not sufficient to guarantee particles confinement because of the drift gradient of the magnetic field $\nabla B \times B$. The effect of $\nabla B \times B$ term is a vertical separation of ion and electrons in plasma column with a resulting electric field E that entails a $E \times B$ drift which pushes the plasma outward. Therefore, to compensate this effect the idea is to stabilize the configuration by adding a poloidal component to the toroidal magnetic field. In a tokamak this field, with closed force lines lying in planes perpendicular to the toroidal direction, is produced mainly by a current flowing in the plasma.

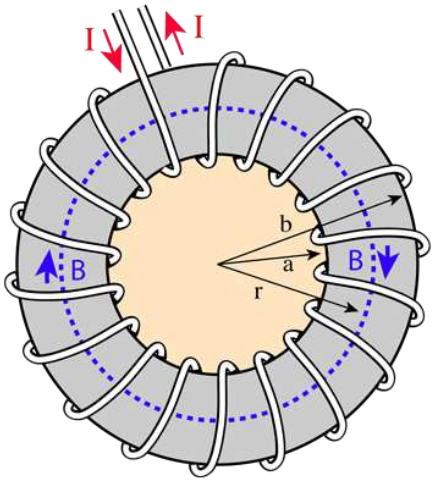

Fig. 3.2 – Solenoid wound on a toroidal core

The superposition of toroidal and poloidal magnetic fields produces magnetic field lines that are helixes twisted round stacked toroidal surfaces having a helical path around the torus as shown in Fig. 3.3. Finally, a vertical component of the poloidal magnetic field, B_z, fixes the position of the current in the plasma and prevent a drifting of the plasma due to the magnetic field gradient from the region of high magnetic field on the inside of the toroid to the region of lower magnetic field on its outside. Vertical magnetic field is generated by means of PFCs.

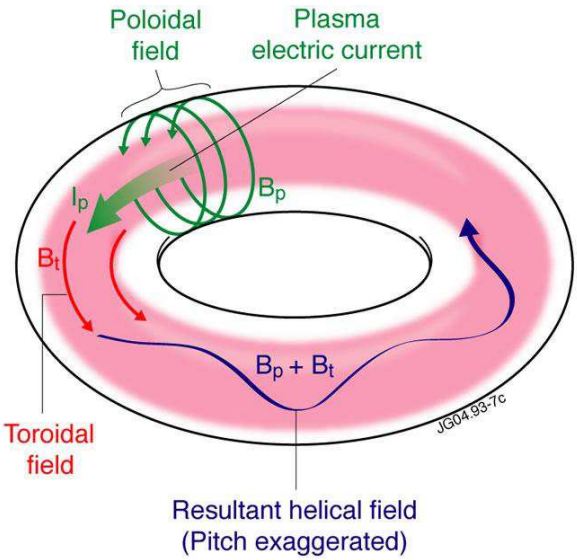

Fig. 3.3 – Total magnetic field in a Tokamak (blue solid line) given by the superposition of toroidal field (red solid line) and poloidal field (green solid lines)

3.3 Tokamak operational limits

In order to optimize fusion performance, the triple product $n \cdot T \cdot \tau_e$ must be take as close as possible to the ignition threshold. However, plasma parameters which appear in Lawson's relationship cannot be increased arbitrarily since MHD instabilities could occur which lead to the loss of plasma confinement. Since plasma temperature T is fixed at a value of $20\,keV$ to maximize the cross-section of Deuterium-Tritium reaction, the parameters to be optimized are plasma density n and confinement time τ_e [13], [14].

For what concerns plasma density, the maximum value of density achievable in a tokamak is limited by the *Greenwald limit*:

(3.2) $n_G = I_p/\pi a^2$

where I_p is plasma current and a is minor radius of the device.

When the line average density exceeds this value, a rapid loss of confinement (*disruption*) occurs. The origin of the density limit is not yet fully understood, but the main findings show strong connection to the edge plasma physics [15]. The density limit involves the cooling of the plasma edge, followed by a steepening of the current profile. For example, the presence of impurities at the plasma edge may increase the line radiation, leading to a local temperature and current density decrease. The resulting steep current profile triggers current-driven instabilities, such as tearing and kink modes, which lead to disruption. The density limit can be extended by reducing the impurities at the edge, for example by means of wall conditioning, or by fueling the plasma core with particle pellets.

The confinement time τ_e cannot be easily increased as well. A direct measurement of τ_e cannot be done, however, it can be deduced from particle and energy transport. Empirical scaling laws have shown that τ_e scales almost linearly with the plasma current I_p, therefore high current operations are necessary to increase the confinement performances of fusion devices. However also the maximum achievable plasma current in a tokamak is limited by the growth of disruptive external ideal kink modes. To be precise, the current

limit is a limit on the minimum value of the safety factor at the edge q_a, in fact the latter can be written, in cylindrical approximation, in terms of the plasma current as:

(3.3) $q_a \cong \frac{2\pi a^2 B_z}{\mu_0 R I_p}$

where:

- B_z: Vertical magnetic field;
- R: Major radius of the device;

By means of energy principles, it is possible to show that, in order to have stable operation, the condition $q_a > 1$ must be fulfilled. This condition is known as *Kruskal-Shafranov limit*. In reality, stable operations require higher values of the edge safety factor ($q_a \geq 3$) and the maximum plasma current is strongly limited.

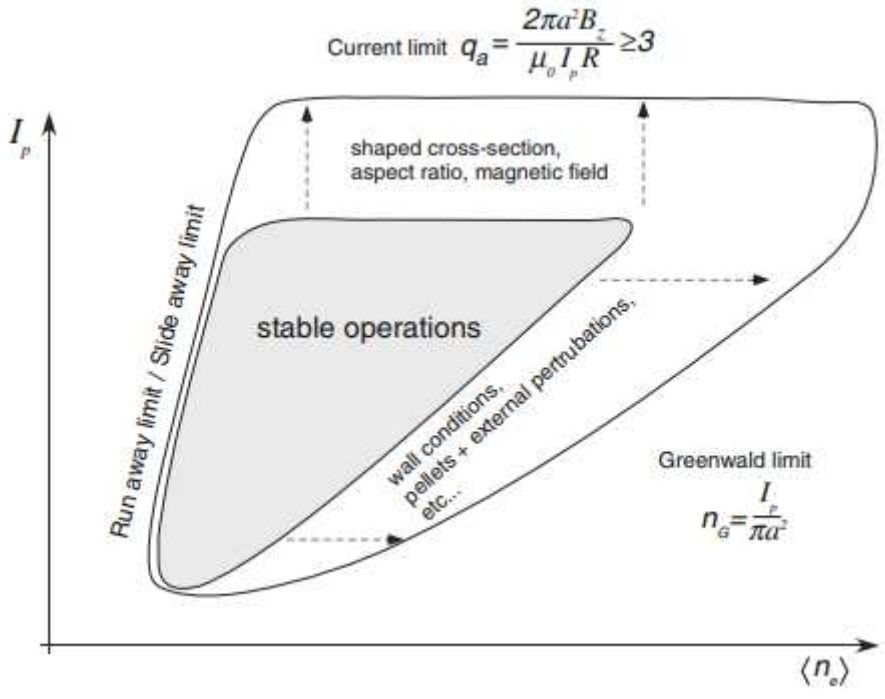

Fig. 3.4 – The Hughill diagram and the main limits for plasma operations [13]

Furthermore, an additional limit exists, involving the maximum attainable kinetic pressure which limits the maximum $\beta = \beta_N$ (this value is known as *normalized beta* and

represents an alternative definition of classic poloidal beta). Actually, the maximum beta value changes assuming a plasma without an external wall or in presence of an ideal wall. In the first case, an external ideal kink mode grows if beta crosses a threshold called no wall limit (β no−wall). In the presence of an ideal external wall, the instability threshold is higher, and the β can be further increased up to the so-called ideal wall limit (β ideal−wall). If these limits are crossed, the external kink modes grow at a rate that cannot be controlled by the feedback system. The operational regime of a tokamak can be represented as a limited area in the (I_p,$\langle n_e \rangle$) plane, where $\langle n_e \rangle$ is the averaged electron density. This is summarized by the so-called Hugill diagram, schematized in Fig. 3.4. This diagram shows three main stability limits, beyond which an abrupt plasma termination occurs (disruption) or the confinement is lost in a longer time (soft limit). It shows also how the boundary of the stable operational region can be enlarged through appropriate operations on the plasma and on the external walls.

3.4 Additional heating systems in Tokamak devices

In order to reach ignition temperature of $10\ keV/20\ keV$, additional heating systems need to be used in tokamak device. A first source of heating is the plasma itself since it can be imagined as an electric conductor and plasma toroidal current can self-heats the plasma through ohmic effect. This effect is known as *ohmic heating*. The power dissipated per unit volume by means of ohmic heating can be expressed as follows:

(3.3) $P_\Omega = \eta J^2$

where η is plasma resistivity and J is current density. Thanks to ohmic heating is possible to increase plasma temperature till a maximum value of about $3\ keV$. Higher temperature values cannot be achieved by means of ohmic heating because plasma resistivity η decreases with increasing temperatures according to *Spitzer's law* $\eta \sim T^{-3/2}$. Furthermore, plasma current value is also limited to a maximum acceptable value since it could trigger MHD instabilities which could lead to disruption events.

In order to obtain higher temperature values additional heating systems are hence mandatory. The main techniques employed to increase plasma temperature are:

- Neutral Beam Injection (NBI);
- Radiofrequency Heating (RF);

3.4.1 Neutral Beam Injection (NBI)

NBI heating technique consists in injecting highly energetic neutral particles in order to heat plasma through the production of fast ions. The main advantage of this system is that the neutral atoms produced are able to overcome the confining magnetic field of a tokamak. In Fig. 3.5 the production process of the neutral beam to be injected is shown. The generation of fast neutral atoms occurs in the following steps:

- Generation of ions within an ion source;
- Extraction of ions and their acceleration by means of electrostatic grids;
- Neutralization of ion beam by passing through a thin neutralizer gas;
- Deflection of the non-neutralized ions to a so-called ion dump;
- Transportation of the neutral atoms produced to the torus;

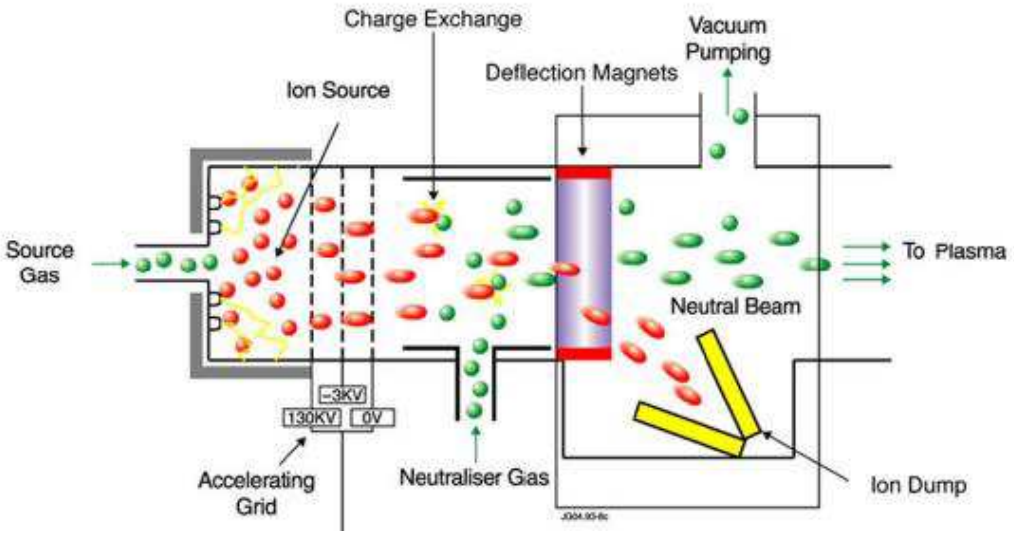

Fig. 3.4 – Main components of an NBI System [16]

Once the neutrals enter the plasma, they can be ionized through the following processes (underlined terms represent the fast particles):

(3.4) $\underline{H}^0 + H^+ \rightarrow \underline{H}^+ + H^0$ (Charge-Exchange);

(3.5) $\underline{H}^0 + H^+ \rightarrow \underline{H}^+ + H^+ + e^-$ (Ionization by ions);

(3.6) $\underline{H}^0 + e^- \rightarrow \underline{H}^+ + 2e^-$ (Ionization by electrons).

All of these processes have a different characteristic cross section, which depends on the relative velocity of the particles involved. The dominant process at low energy is the Charge-Exchange process, while at high energies it is the Ionization by ions. Ionization by electrons is usually quite ineffective.

Once the fast ions have been formed, they can be confined by the magnetic field and can transfer energy to the plasma by thermalization processes [17].

The design of an NBI system has to be realized in order to optimize the system efficiency reducing the losses in particular, for NBIs some of the main losses are:

- The not ionization of neutral particles of the beam (this phenomenon is known as *shine-though*). Since neutral particles are highly energetic, if the amount of neutral particles passing through the plasma is large, serious damage to the first wall could be caused;
- Charge-Exchange losses due to the interaction between fast ions produced and background neutrals $\underline{H}^+ + H^0 \rightarrow \underline{H}^0 + H^+$

3.4.2 Radiofrequency Heating (RF)

Radiofrequency heating consists in sending a high frequency electromagnetic wave to plasma. Since plasma charged particles spiralize around magnetic field lines describing cyclotronic motion, if an electromagnetic wave with a frequency correspondent to *cyclotronic resonant frequency* of a given particle species, is lunched into plasma, the wave transfers energy to the targeted particles, resulting into an effective heating. Since

the energy is transferred to the plasma at the exact location where radio waves resonate with the ion/electron rotation, the antennas, which produce the waves responsible for the heating, are mounted inside the vacuum chamber. The system design must be such as to allow the waves to propagate in the central region of the plasma where the absorption is improved. The two main cyclotronic resonance heating systems are:

- Electron Cyclotron Resonance Heating (ECRH);
- Ion Cyclotron Resonance Heating (ICRH);

The ECRH frequency can be computed as:

(3.7) $\omega_{EC} = \frac{eB}{m_e} \Rightarrow f_{EC} = 28 \frac{GHz}{T} \cdot B.$

It is evident that ECRH frequency depends only on the magnetic field intensity B since m_e and e are fixed. For positive ions instead, the cyclotronic resonant frequency can be expressed as:

(3.8) $\omega_{IC} = \frac{qB}{m_i}.$

In this case, it results that ICRH frequency depends on magnetic field B but also on the mass of the particular ion species. If H^+ ions are considered ($m_i = 1840\, m_e$) then $f_{IC} = 15.2 \frac{MHz}{T} \cdot B$. The main components of a general scheme of a cyclotronic heating system (Fig. 3.5) is composed by [18],[19]:

- High power generator sources;
- Transmission lines;
- Launchers or Antennas;

For what concerns the sources, the most suitable power generators in ICRH frequency range $(10 - 100\, MHz)$ are *high power tetrodes* which are high vacuum electronic devices with four electrodes used as signal amplifiers.

In ECRH systems the power source used is the *gyrotron*, a type of free-electron maser which generates high-frequency electromagnetic radiation by stimulated cyclotron resonance of electrons moving through a strong magnetic field. The frequency range of gyrotrons is typically from $20\ GHz$ to $245\ GHz$. The output of the power generator is then sent to launchers through transmission lines which must be designed on the base of some fundamental characteristics which are: to transmit power with lower losses; to ensure stable and safe operations for the source; to match the delivered power with the plasma.

In the frequency range of ICRH systems the most suitable medium for guided transmission is the *coaxial cable* while in ECRH system the transmission lines used are simple *circular waveguides* transmitting the TE_{01} mode which is proved to be the less attenuated mode of propagation.

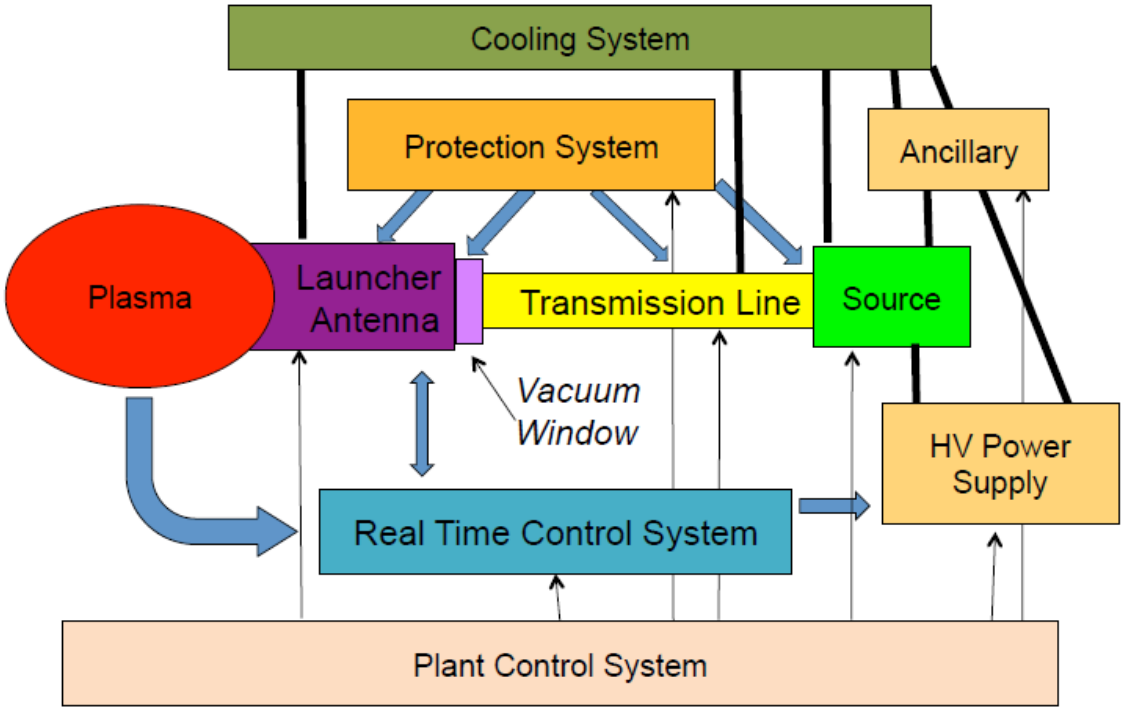

Fig. 3.5 – General scheme of a cyclotronic heating system [18]

The coupling between the power delivered by transmission lines and plasma is guaranteed by means of suitable launchers designed in order to maximize plasma-wave coupling. In ICRH systems, launchers are arrays of *current straps* fed by coaxial cables. From an

electrical point of view, a strap can be seen as a very short transmission line terminated on a short circuit, that is directly connected to the ground. The protection of the straps from plasma interaction is realized by mean of a *Faraday shield*, a structure made by conducting metallic rods positioned in front of the strap.

In ECRH systems the launchers are typically *truncated waveguides* propagating the delivered mode. To reduce the divergence of the beam, it is possible by increasing the waveguide diameter or the frequency of the propagating wave.

3.5 Plasma diagnostics in Tokamak devices

Plasma diagnostic plays nowadays an important role in fusion experiments. The main tasks of plasma diagnostics can be summarized as follows [20]:

- *Machine protection and basic plasma control*: Measurements in real-time of specific plasma and machine parameters are necessary to prevent damage to machine components (for instance divertor and first wall);
- *Advanced plasma control*: Measurements of the main plasma parameters are needed to achieve high plasma performances (good energy confinement time, control of impurities…) in advanced operating scenarios;
- *Physics studies and performance optimization*: Further measurements are desirable to improve the understanding of plasma behavior (transport studies, plasma instabilities…) and to optimize the fusion reaction performances;

Commonly, plasma diagnostics are classified in *active* and *passive* diagnostics. While passive diagnostics measure what plasma spontaneously emits, active diagnostics require the injection of light beams, particles or probes measuring the induced effect. Examples of passive diagnostics [21] are: Mirnov coils and Rogowski coils.

Mirnov coils (Fig. 3.6) are magnetic sensors which are able to measure magnetic field. In a uniform magnetic field varying with time $B(t)$, the induced voltage in the coil, according to Faraday-Neumann's law, is:

(3.9) $V = NA\frac{dB}{dt}$;

where N is the number of turns in the coils of area A.

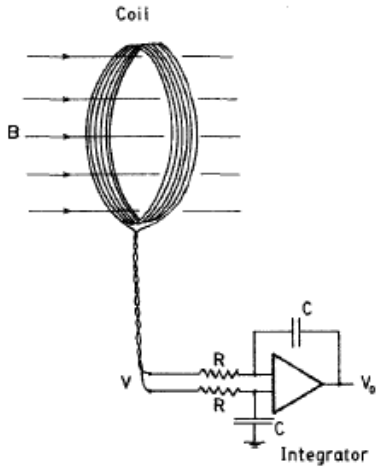

Fig. 3.6 – Example of Mirnov coil [21]

Making use of a simple analog integrator it possible to obtain a voltage signal directly proportional to B:

(3.10) $V_0 = \frac{NAB}{RC}$;

Where RC is the time constant of the integrator.

Rogowski coil is a solenoidal coil whose ends are brought together to form a torus (as illustrated in Fig. 3.7). Consider a coil of uniform cross-sectional area A with constant turns per unit length n. Provided that the magnetic field varies little over one turn spacing, that is, if $\frac{|\nabla B|}{B} \ll n$, the total flux linkage by the coil can be written as an integral rather than a sum over individual turns:

(3.11) $\Phi = n \int_A \left(\oint_l \boldsymbol{B} \cdot d\boldsymbol{l} \right) dA$.

According to Ampere's law:

(3.12) $\oint_l \boldsymbol{B} \cdot d\boldsymbol{l} = \mu I$

where I is the total current encircled by l and μ is the magnetic permeability of the medium in the solenoid. Thus:

(3.13) $\Phi = nA\mu I$

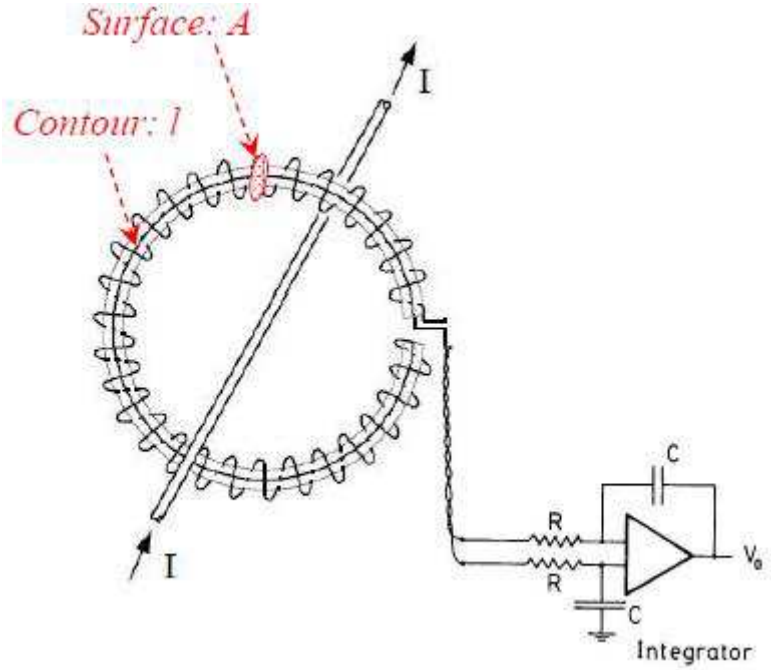

Fig. 3.7 – Example of Rogowski coil [20]

and the voltage out of the Rogowski coil is

(3.14) $V = nA\mu \frac{dI}{dt}$.

A measure of current I can be easily obtained by means of a simple integrator circuit.

In nuclear fusions applications Rogowski coils are often used to measure plasma current. Concerning active diagnostics, some examples of them are:

- Thomson scattering: Scattering of laser light from the electrons in a plasma is known as Thomson scattering. The electron temperature can be determined very reliably from the Doppler broadening of the laser line. The electron density can be determined from the intensity of the scattered light, but a careful absolute calibration is required. Although Thomson scattering is dominated by scattering from electrons, since the electrons interact with the ions, in some circumstances information on the ion temperature can also be extracted;
- Langmuir probes: Langmuir probe measurements are based on the estimation of current versus voltage characteristics of a circuit consisting of two metallic electrodes that are both immersed in the plasma under study. Conventional Langmuir probe theory assumes collision less movement of charge carriers in the space charge sheath around the probe. Further it is assumed that the sheath boundary is well-defined and that beyond this boundary the plasma is completely undisturbed by the presence of the probe. This means that the electric field caused by the difference between the potential of the probe and the plasma potential at the place where the probe is located is limited to the volume inside the probe sheath boundary. Langmuir probes can be used to determine ion saturation temperature or plasma potential;
- Interferometry, polarimetry and reflectometry:
    1. The basic principle of interferometry is that an electromagnetic wave which travels inside plasma experience a phase shift compared to the case of vacuum. The measure of this phase shift between reference (vacuum case) and plasma beams allows measurements of line-average electron density;
    2. The polarization of an electromagnetic wave probe is altered upon propagation through the plasma in a way that depends on the magnetic field. The measure of the change of polarization of the wave allow to measure parallel and perpendicular components of magnetic field;
    3. Reflectometry is a method well suited for measurements of local electron densities. This can be done by sending microwaves radially into

the plasma that are reflected at a certain distance when the electron density is high enough. It is possible to retrieve the radial profile of electron density modulating the frequency of microwaves sent to plasma;

3.6 Overview on existing and future devices

In this chapter a general overview on fusion devices on which my research and experimental activities has been performed will be provided. The details of the main activities and results provided during the PhD will be presented in details in Chapter 4.

3.6.1 EAST

EAST (Experimental Advanced Superconducting Tokamak) project was approved by the National Development and Reform Commission in July 1998. Construction started in October 2000; assembly was finished at the end of 2005, and commissioning was completed in March 2006. The 28th September 2006, the first plasma has been successfully produced. Its design, R&D, construction and assembly have been done mainly by scientists, engineers and technicians in the ASIPP.

EAST tokamak (in Fig. 3.8 an image of the vacuum chamber is reported) is designed on the basis of the latest tokamak achievements of the last century, aiming at the world fusion research forefront. Its mission is to conduct fundamental physics and engineering researches on advanced tokamak fusion reactors with a steady, safe and high performance operations, to provide a scientific base for experimental reactor design and construction, and to promote the development of plasma physics and related disciplines and technologies. EAST device has three distinct features: non-circular cross-section, fully superconducting magnets and fully actively water-cooled plasma facing components which will be beneficial to explore the advanced steady-state plasma operation modes. EAST construction and physics research will provide direct experience for the construction of International Thermonuclear Experimental Reactor project (ITER) and play a leading role in high-performance steady-state plasma physics research in the world, and ultimately contribute to the development of ITER and the fusion energy. Compared

with ITER, although smaller, EAST is similar to ITER in shape and equilibrium, yet more flexible. During ITER construction, EAST will be one of a few international devices that can be an important experimental test bench for conducting ITER related steady-state advanced plasma science and technology research.

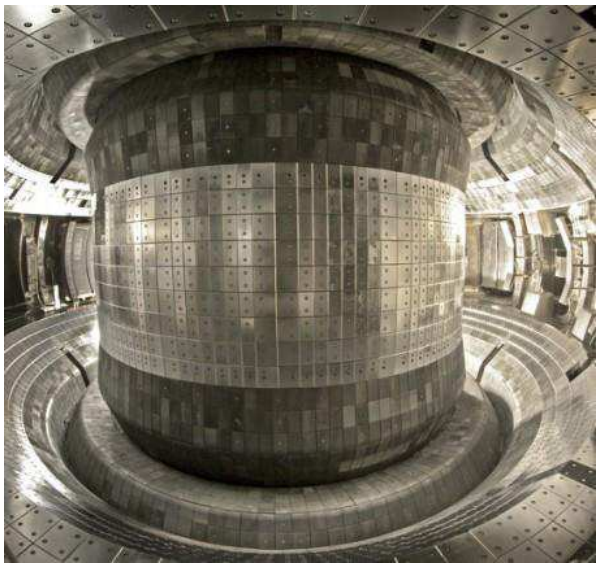

Fig. 3.8 – Internal view of EAST Tokamak

EAST electromagnetic system (in Fig. 3.9 a 2-D poloidal plane has been reported) has been designed with 14 PFCs and 16 TFCs both realized in NbTi/Cu. Concerning the poloidal system the 14 PFCs are driven by 12 individual power supplies each of the coil pairs PF7/PF9 and PF8/PF10 are connected in series and treated as one single coil. The PFCs have been designed with the intent of combining plasma heating and shaping/equilibrium control. In order to provide fast response for plasma vertical instability control, two normal copper coils (IC1 and IC2) connected in anti-series are installed inside the vacuum vessel [22]. A double-wall vacuum vessel was designed with 316L stainless steel. The space of 30 mm inboard and 80 mm outboard between the two walls of the vacuum vessel will be filled with 100 °C borated water that is effective as neutron shield during Deuterium-Deuterium operations [23]. Aiming at long pulse plasma discharges, a series of experimental techniques have been developed or improved on EAST in recent years, such as ion cyclotron heating, plasma diagnostics and control, lithium wall conditioning; the effective heating and current drive were realized under a

variety of plasma configurations; and the divertor operation were explored in steady-state mode.

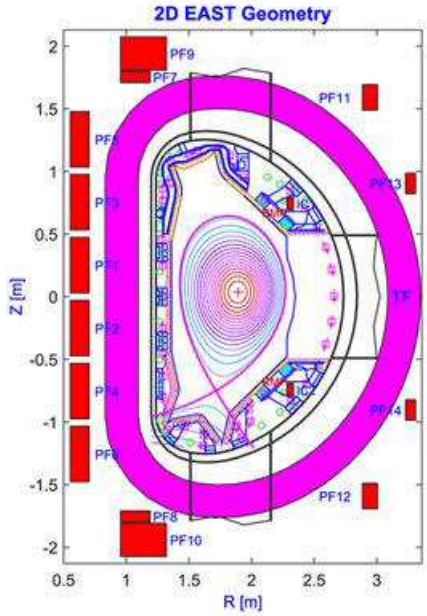

Fig. 3.9 – Poloidal plane view of EAST Tokamak [24]

These contributed to a lot of achievements on EAST experiments: obtainment of repeatable plasma current of 1 MA, the highest parameter on all existing superconducting devices, realizing EAST first scientific goal. Long-pulse diverted plasma discharges of 0.25 MA and 100 s duration under the central electron temperature of 15 million degrees were realized. This is the longest diverted plasma discharge in the world up to now. H-mode plasma discharge were successfully obtained; Through the further optimization of the operation mode, H-mode plasma discharge reaches 6.4 s, with a duration more than 60 times of energy confinement time, realizing quasi-steady state; Important progress has been made on the study of plasma spontaneous rotation experiment and mechanism research of L-H mode conversion [25].

3.6.2 DTT

In 2012 EFDA published "Fusion Electricity – A roadmap to the realization of fusion energy" [26], which sets out a strategic vision toward the generation of electrical power

by a Demonstration Fusion Power Plant (DEMO) by 2050. The roadmap elaborates 8 strategic missions to tackle the main challenges in achieving this overall goal. In particular, mission 2 related to the development of an adequate solution for the plasma heat exhaust of DEMO, is one of the most challenging among the roadmap missions. The current strategy, to be tested on the ITER device, foresees optimizing plasma operations with a conventional divertor based on detached plasma conditions. However, the risk exists that the baseline strategy (conventional divertor solution) pursued in ITER cannot be extrapolated to a fusion power plant. In addition, even if ITER divertor will prove to be successful, it will be difficult to extrapolate to DEMO, because of its additional requirements (more nuclear aspects and thus limited use of some materials, requirements in terms of life expectancy of reactor components and thus need of keeping the temperature low in the divertor region with nearly zero erosion, etc…). Therefore, a specific project has been launched to investigate alternative power exhaust solutions for DEMO, aimed at the definition and the design of a Divertor Tokamak Test facility (DTT). The role of the DTT facility is to bridge the gap between today's proof-of-principle experiments and DEMO. The DTT facility will test the physics and technology of various alternative divertor concepts under integrated physics and technical conditions that can confidently be extrapolated to DEMO. The tests must show that the alternative concept can be developed into a controllable exhaust solution for DEMO, including Plasma Facing Components (PFCs), diagnostics and actuators, which can be integrated with all other aspects of a power plant. In the following are briefly reported the main objectives of DTT [27]:

- Demonstrate a heat exhaust system capable of withstanding the large load of DEMO in case of inadequate radiated power fraction;
- Close the gaps in the exhaust area that cannot be addressed by present devices;
- Demonstrate that the possible (alternative or complementary) solutions (e.g., advanced divertor configurations or liquid metals) can be integrated in a DEMO device, e.g. via demonstration that:
    1. An alternative divertor magnetic configuration is viable in terms of the exhaust problems as well as of the plasma bulk performances;

2. An alternative divertor magnetic configuration is viable in terms of poloidal coils constraint (i.e., currents, forces,…) as well as of the plasma bulk performances;
3. A geometry divertor (compatible with an alternative divertor magnetic configuration) is viable in terms the DEMO technology (materials, space for the blanket, …);
4. A closed loop liquid metal heat removal system is viable in a tokamak at relevant edge and Scrape Off Layer parameters;
5. Liquid metals are applicable to DEMO (impurities, MHD, etc.);
6. An integrated exhaust scenario is viable;

DTT will operate in parallel with ITER therefore, it could support and complement the ITER experimental program, paying particular attention to high priority issues like disruption avoidance/mitigation, ELM mitigation and plasma control [28].

3.6.3 DEMO

In the European strategy DEMO is the only step between ITER and a commercial fusion power plant. Its general goals are [26],[29]:

- Produce net electricity for the grid at the level of a few hundred MWs;
- Breed the amount of tritium needed to close its fuel cycle;
- Demonstrate all the technologies for the construction of a commercial FPP (Fusion Power Plant), including an adequate level of availability.

DEMO requires a significant amount of innovation in critical areas such as heat exhaust, materials and tritium breeding. On the other hand, to design DEMO on the basis of the ultimate technical solutions in each area would postpone the realization of fusion indefinitely. For this reason, a pragmatic approach is needed. To meet its general goals, DEMO will have to rely on simple and robust technical solutions and well established and reliable regimes of operation, as far as possible extrapolated from ITER, and on the use of materials adequate for the expected level of neutron fluence. In addition, DEMO must be capable of addressing goal also through the test of the advanced components and

technical solutions that will be developed in parallel for application in a fully-fledged FPP, thus playing the role of a component test facility as part of its mission.

The experience gained in the ITER construction will be used directly for the integrated DEMO design, but specific system development will be required in some areas. Above all, special emphasis will have to be given to the maintainability and reliability of components, in particular:

- The development of the remote maintenance system for DEMO is driven by the need to maximize the overall plant availability and minimize the plant down time for maintenance;
- The need for a self-sufficient tritium fuel cycle and pulses of a few hours demands systems based on either a cryopump or continuously working pumps with an effective tritium separation and recycle function of the exhaust;
- It will be necessary to develop new diagnostic techniques that are DEMO relevant since many existing diagnostic techniques will not be applicable in the harsh environment of DEMO and the number of diagnostics and actuators available for plasma control will be reduced significantly.

During the initial period of operation DEMO is expected to test components, collecting directly data on their reliability. For example, it may be acceptable to utilize a ‘starter’ breeding blanket configuration using moderate-performance materials and then switch to blankets with a more advanced-performance material. This type of approach has been used for the fuel cladding in fission reactors for many years, by limiting the maximum exposure level of the replaceable cladding to below the regulatory limit while data for higher exposure operation is generated in test reactors or load test assemblies. This approach benefits from the multiple-barrier safety approach in fission reactors, including the pressure vessel as a key safety boundary for regulatory approval. Similarly, for a fusion DEMO, operation up to moderate exposures could be envisaged for the ‘starter’ blanket, while high-dose engineering data for a more advanced-materials blanket was being generated in a dedicated 14 MeV neutron source. A similar philosophy should be applied to the divertor, with the possibility of a ‘starter’ divertor. The replacement of blankets or divertors cannot be accompanied by a complete change of the balance of plant, as this is clearly unfeasible. Thus, either the series of blanket concepts and divertor

concepts each assume the same coolant (although the divertor and blanket coolants could, in principle, be different) or the new components are tested in dedicated ports (in the same spirit of the ITER TBM test). During the second phase of operation DEMO will progress towards the demonstration of high plant availability.

Chapter 4: Research activity – EAST – DEMO – DTT

"The important thing in science is not so much to obtain new facts as to discover new ways of thinking about them"

William Lawrence Bragg, Nobel laureate in physics in 1915

In this chapter the research activity carried out during the three PhD years will be presented. The research activity focuses on the development of equivalent plasma-circuit axisymmetric models for fusion devices. The presence of an accurate plasma-circuits model plays an important role both for the study of existing tokamak and for the design of future tokamaks. Indeed, an accurate plasma-circuits model is the basis for the definition of feedback control strategies for plasma shape and vertical stability control. On the other hand, it is widely used for the optimization of the geometrical configuration and the PF coil system of future tokamaks. The main research activities carried out during the PhD have been focused of electromagnetic studies on EAST, DTT and DEMO tokamaks. They can be summarized as follows:

- EAST: Definition and experimental validation of a 2D axisymmetric dynamical model for EAST plasma discharges
- DEMO: Design of reference scenarios in case of Single Null (SN), Double Null (DN) and alternative plasma configurations; additional effort has been dedicated to the Vertical Stability Analysis (VSA) for SN and alternative configurations.
- DTT: Definition and optimization of PF coil system and plasma scenarios for DTT tokamak in case SN, DN and alternative plasma configurations

To introduce the points regarding experimental activity, the definition and the analysis of Alternative or Advanced Magnetic Configurations will be provided in the following section.

4.1 Alternative magnetic configurations

A reliable solution to the problem of heat exhaust is probably the main challenge towards the realization of magnetic confinement fusion [26]. The main risk is that the baseline strategy pursued in ITER cannot be extrapolated to a fusion power plant. Hence, in parallel to the programme in support of the baseline strategy, a dedicated research programme on alternative solutions for the divertor was promoted by EFDA and represents one of the key points in the European roadmap pursued by EUROfusion, EFDA successor. Some concepts have already been tested at proof-of-principle level and their technical feasibility in a fusion power plant is being assessed.

One possible solution to the power exhaust problem is represented by the so called Advanced or Alternative Magnetic Configurations whose fundamental aim is to produce magnetic fields by which the charged particles, following the field lines, spread their energy on a broader area once they reach the plasma-facing components or dissipate great part of their energy before reaching the solid surfaces. Conventionally, the "Alternative" or "Advanced" configurations are defined as magnetic geometries characterized by a magnetic topology different from the standard Single Null [30]. Since the extrapolation from proof-of-principle devices to ITER/DEMO based on modelling alone is considered too large, a dedicated test on specifically upgraded existing facilities or on a dedicated Divertor Tokamak Test (DTT) facility [27] will be necessary.

In the following, the main characteristics of the fundamental magnetic alternative configurations will be described.

4.1.1 Double Null (DN) configuration

The Double Null (DN) configuration (Fig. 4.1) produces a second first order null point in the poloidal magnetic field in the upper part of the main chamber. This diverts a significant fraction of the heat load to the inner divertor of a SN to a second target at larger radius, which increases the wall interaction area and decreases the peak heat load reaching the targets. However, it also decreases the connection length to the target.

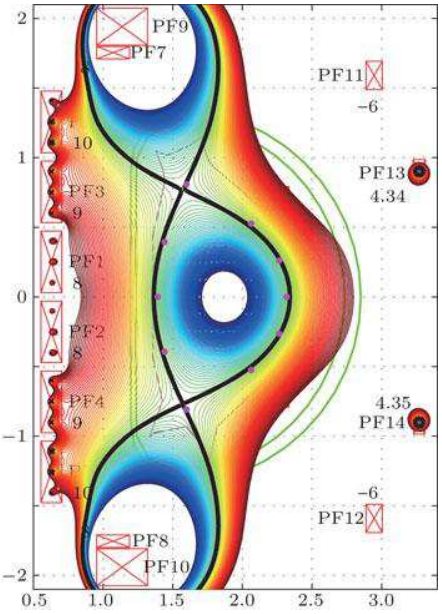

Fig. 4.1 – Example of Double Null (DN) configuration [31]

4.1.2 X-Divertor (XD) configuration

The X divertor concept (Fig.4.2) [35] seeks to flare the flux surfaces, i.e. increase the poloidal flux expansion, near the divertor targets.

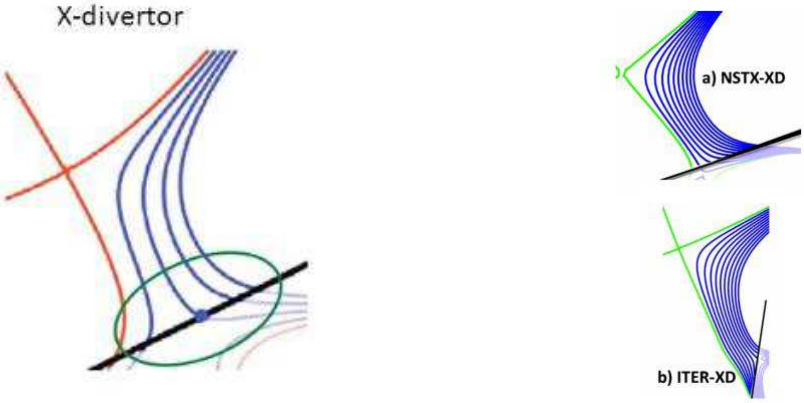

Fig. 4.2 – Example of X-Divertor (XD) configuration [30]

The flaring is obtained by decreasing the poloidal magnetic field at the target, albeit at

the cost of a lower grazing angle of the field line at the target. Typically, two dedicated divertor coils are used for each target. The flaring may introduce a mechanism that counteracts the upward movement of the detachment front and result in a more robust detachment [30]. The lower poloidal field also leads to an increase in the connection length. In addition, the flaring improves the potential of including gas baffles in the divertor concept. The XD is usually only considered as a solution for the outer leg. If the merits of the XD are confirmed, it may also be considered for the inner leg or as part of a double null. The flaring of the flux on the inboard leg, however, poses a greater challenge for the coil configuration design.

4.1.3 SnowFlake Divertor (SFD) configuration

The snowflake divertor concept seeks to decrease the poloidal field in the vicinity of the null point by introducing a second order null point [32]. This splits the separatrix around the null into six legs with two enclosing the confined plasma and four divertor legs. Since the exact SFD (Fig. 4.3a) is only a point in the operational plane any real configuration is characterized by two nearby X-points [33].

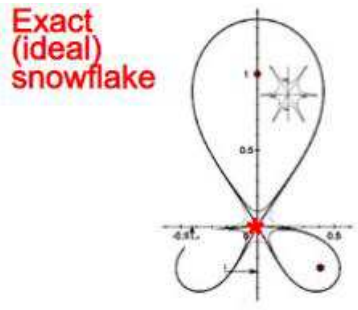

Fig. 4.3a – Example of exact Snowflake configuration [34]

Fig. 4.3b – Example of Snowflakee minus configuration [34]

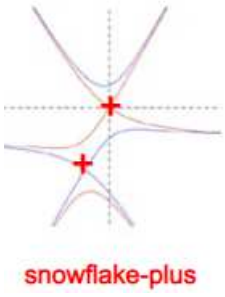

Fig. 4.3c – Example of Snowflake plus configuration [34]

The resulting configuration may have different topologies referred to snowflake plus

(SFD+) (Fig.4.3c) and snowflake minus (SFD-) (Fig. 4.3b) depending on whether the second x-point is located in the private or common flux region of the primary, active x-point, respectively. The flux expansion is greatly increased in the region near the core X-point, but rapidly decreases downstream so that the Scrape Off Layer is strongly convergent (even more than for a Standard Divertor). A potentially undesirable consequence is an increase of the poloidal flux compression towards the target (in contrast to the XD). The lower poloidal field in the null point region leads to a longer connection length and divertor volume and is expected to generate large volumetric losses.

4.1.4 Super-X (SXD) configuration

The Super-X Divertor (SXD) (Fig. 4.4) concept seeks to increase the total flux expansion towards the target. This is achieved by increasing the major radius of the divertor targets, R_t [36]. The maximum value is usually limited by the toroidal field coils. The increase of R_t may be combined with an increase of flux expansion f_{exp} as proposed in the XD concept, leading to the name "Super-X divertor". Increasing R_t allows for an increase of the wetted area, without decreasing the grazing angle of the field lines at the target or invoking plasma physics. The increase of the total flux expansion introduces a decrease of the parallel heat flux, $q_{\parallel}$, towards the target, which is predicted to stabilise the location of the radiation fronts.

4.2 EAST Modelling activity

In this Section, modelling activity carried out on EAST Tokamak will be presented. In order to develop advanced plasma magnetic controllers and to design plasma scenarios of both standard and alternative configurations (such as DN and SF), a reliable 2-D axisymmetric plasma linearized model of EAST Tokamak is needed. The equilibria and linearized models have been developed with CREATE-NL and CREATE-L codes [37]-[12] and the validation of the models produced has been done on experimental plasma shots. The definition of the linearized dynamic simulator of EAST discharges has

requested the developments of additional routine for the linearized code.

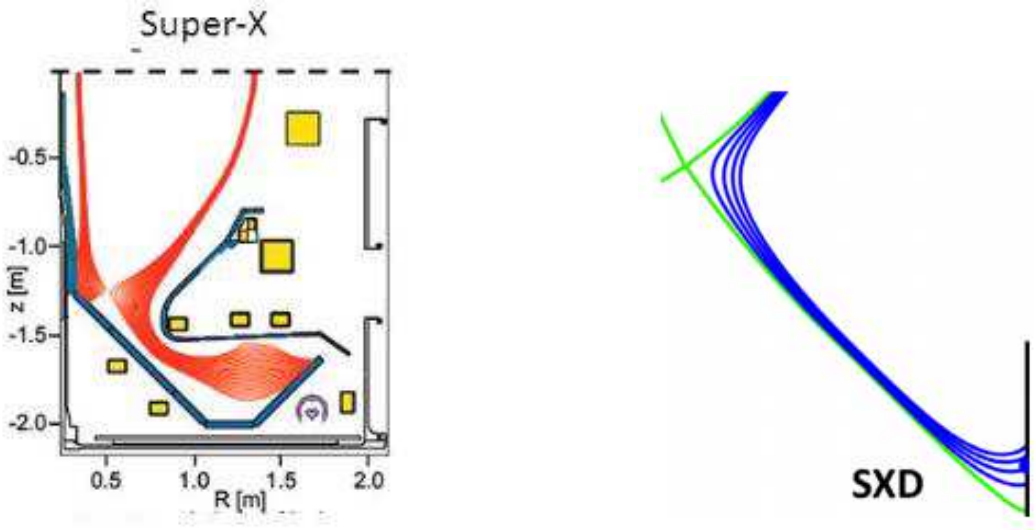

Fig. 4.4 – Example of Super-X Divertor (SXD) configuration [30]

Indeed, in Section 4.2.1, a change of variables of the linearized model will be shown in order to have the PF coils in current driven mode; in Section 4.2.2, a procedure for the identification and linearization of flux and position of non-active X-point will be proposed [38]. Finally, in section 4.2.3 a validation of the linearized models will be carried out performing open loop simulations using as inputs experimental signals and comparing the model outputs with experimental data. In order to perform the validation analysis, a set of routines to automatically download these signals from a dedicated MDSPlus [39] database has been developed.

4.2.1 Hybrid driven Poloidal Field Coils

The linear model presented in (2.46) and (2.47) is the standard output of CREATE-L code. In this model it is assumed that all the coils are voltage driven. However, the Vertical Stabilization (VS) system adopted in the EAST PCS exploits the In-Vessel circuits in current-driven mode. Furthermore, the experimental current signals resulted to be more reliable than the measured voltages on active circuits. For these reasons, a change

of variable was needed in order to have a subset of coils in current driven mode. First of all, let us split the current vector split as follows:

(4.1) $I(t) = [I_{VD}(t)^T \; I_{CD}(t)^T]^T$;

Where I_{VD} and I_{CD} indicate the currents in the voltage driven and current driven circuits respectively. The voltage driven circuits also include the plasma and the passive elements where $V = 0$. Plasma-circuit equation (2.40) can be then rewritten as:

(4.2) $\begin{bmatrix} L_{11} & L_{12} \\ L_{21} & L_{22} \end{bmatrix} \begin{bmatrix} \dot{I}_{VC} \\ \dot{I}_{CD} \end{bmatrix} = - \begin{bmatrix} R_{11} & 0 \\ 0 & R_{22} \end{bmatrix} \begin{bmatrix} I_{VC} \\ I_{CD} \end{bmatrix} + \begin{bmatrix} V_{VC} \\ V_{CD} \end{bmatrix}$;

For the sake of simplicity, the disturbances have been neglected however, they can easily be included in the input vector applying simple matrix algebra. Experimental traces of β_P and l_i reconstructed during EAST experiments are available in EFIT database [40]. Choosing magnetic fluxes $\Psi = LI$ as new state variables, it is possible to rewrite Ψ as follows:

(4.3) $\Psi = L_{11} I_{CD} + L_{12} I_{VD} \;\Rightarrow\; I_{VD} = L_{11}^{-1}\Psi - L_{11}^{-1} L_{12} I_{CD}$;

Substituting equation (5.3) in equation (5.2) we get:

(4.4) $\dot{\Psi} = \; -R_{11} L_{11}^{-1}\Psi + \; R_{11} L_{11}^{-1} L_{12} I_{CD} + V_{VD} \;\Rightarrow\; \dot{\Psi} = A\Psi + B \begin{bmatrix} U_{VD} \\ I_{CD} \end{bmatrix}$

where:

- $A = -R_{11} L_{11}^{-1}$;
- $B = [I \; R_{11} L_{11}^{-1} L_{12}]$ where I is the identity matrix;

For the output equation, substituting (5.3) in (2.47) we get:

(4.5) $y(t) = C_1 I_{VD} + C_2 I_{CD} + D_1 V_{VD} \Rightarrow y(t) = C\Psi + D\begin{bmatrix} V_{VD} \\ I_{CD} \end{bmatrix}$

where:

- $C = C_1 L_{11}$;
- $D = [D_1\ C_2 - C_1 L_{11}^{-1} L_{12}]$.

In order to have a good estimation of plasma current behavior in the time simulation interval, an equivalent plasma resistance can be obtained by means of experimental flux measurements and making use of Faraday-Neumann's law. Once computed equivalent plasma resistance, it's possible to apply to the plasma circuit an equivalent voltage in order to take into account also possible current drive effects.

4.2.2 Identification of flux and position of non-active X-point

EAST control system implements two different control logics for the shape control, namely RZIP and Isoflux (for a detailed description see [22]). In particular, the Isoflux control logic aims at taking to zero the poloidal flux differences between the active X-point and some specific points, defined as the intersections between some control segments and the desired plasma boundary. For this reason, a good reconstruction of the fluxes on these segments is essential. To achieve this purpose, a set of 10 evenly spaced virtual flux sensors has been placed on each of the segments available for shape control as shown in Fig. 4.5. The flux in the actual control points (whose positions can be retrieved from the EFIT dedicated database) is then obtained interpolating. The isoflux control logic includes also a direct control of the position of the null-points, either only the active one or both active and non-active, depending on the configuration. Furthermore, the knowledge of the flux at the X-point is necessary for the shape control. For these reasons, a procedure for an accurate identification of the X-points dynamics in terms of radial and vertical position and poloidal flux has been implemented. The starting

assumption is that the X-point is a stationary point for the poloidal flux. Hence, a quadratic function to estimate the flux in a desired region of the poloidal plane containing the X-point has been considered:

(4.6) $\Psi(r,z) = ar^2 + brz + cz^2 + dr + ez + f$;

To determine the vector coefficients $[a\ b\ c\ ...\ f]^T$, two grids of $n \times n$ virtual flux sensors surrounding the expected X-point positions have been considered. The measurements of the virtual flux sensors are derived by a reconstructed flux map. Since the magnetic fluxes in the points of the grids are known, the vector coefficients can be calculated as:

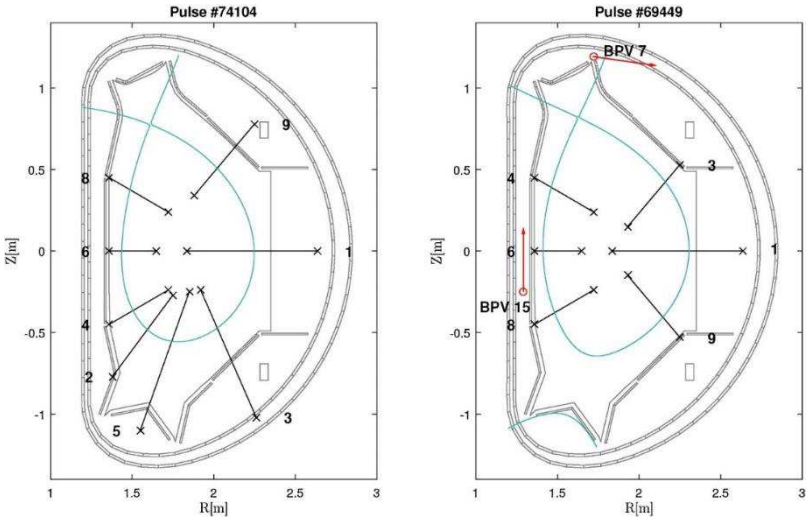

Fig. 4.5 – Virtual flux sensors placed on active control segments for upper single null pulse #74104 (left) and for double null shot #69449 (right). In blue is reported plasma boundary reconstructed using EFIT database. For double null shot #69449 the position in the poloidal plane of magnetic probes BPV 7 and BPV 15 (red circles), which are oriented tangentially with respect to the vessel, has also been reported.

$$(4.7)\quad \begin{bmatrix} r_1^2 & r_1 z_1 & z_1^2 & r_1 & z_1 & 1 \\ r_2^2 & r_2 z_2 & z_2^2 & r_2 & z_2 & 1 \\ & & \dots & & & \\ r_n^2 & r_n z_n & z_n^2 & r_n & z_n & 1 \end{bmatrix} \begin{bmatrix} a \\ b \\ c \\ d \\ e \\ f \end{bmatrix} = \begin{bmatrix} \Psi_1(r_1, z_1) \\ \Psi_2(r_2, z_2) \\ \dots \\ \Psi_n(r_n, z_n) \end{bmatrix} \Rightarrow$$

$$\Rightarrow \begin{bmatrix} a \\ b \\ c \\ d \\ e \\ f \end{bmatrix} = \begin{bmatrix} r_1^2 & r_1 z_1 & z_1^2 & r_1 & z_1 & 1 \\ r_2^2 & r_2 z_2 & z_2^2 & r_2 & z_2 & 1 \\ & & \dots & & & \\ r_n^2 & r_n z_n & z_n^2 & r_n & z_n & 1 \end{bmatrix}^{\dagger} \begin{bmatrix} \Psi_1(r_1, z_1) \\ \Psi_2(r_2, z_2) \\ \dots \\ \Psi_n(r_n, z_n) \end{bmatrix}$$

Where $[\dots]^{\dagger}$ denotes the Moore-Penrose pseudoinverse matrix. Once the vector coefficients are computed, position and flux of X-point can be evaluated. Since X-points are stationary points, it is:

$$(4.8)\ \nabla\Psi(r_{xp}, z_{xp}) = \left.\frac{\partial\Psi}{\partial r}\right|_{\substack{r=r_{xp}\\z=z_{xp}}} \hat{r} + \left.\frac{\partial\Psi}{\partial z}\right|_{\substack{r=r_{xp}\\z=z_{xp}}} \hat{z} = 0$$

Where r_{xp} and z_{xp} indicate radial and vertical position of X-point respectively. Computing the magnetic flux gradient in (r_{xp}, z_{xp}) we have:

$$(4.9)\ \begin{bmatrix} 2a & b \\ b & 2c \end{bmatrix} \begin{bmatrix} r_{xp} \\ z_{xp} \end{bmatrix} + \begin{bmatrix} d \\ e \end{bmatrix} = \begin{bmatrix} 0 \\ 0 \end{bmatrix} \Rightarrow \begin{bmatrix} r_{xp} \\ z_{xp} \end{bmatrix} = -\begin{bmatrix} 2a & b \\ b & 2c \end{bmatrix}^{-1} \begin{bmatrix} d \\ e \end{bmatrix};$$

Finally, the X-point flux can be computed by means of equation (5.6). In Fig. 4.6 are shown the results of the procedure applied to DN pulse #46530. Indeed, in this case, starting from the EFIT flux map reconstruction, a $n \times n$ grid of virtual sensor with $n = 5$ and a distance of around 5 cm between two adjacent sensors has been considered, as shown in Fig. 4.7. The error between EFIT reconstruction (blue solid line) and the estimation (blue circle) is less than 1 mm for both the active and non-active X-points, hence proving the goodness of the method. It is worth to mention that the proposed method can be applied to divertor configurations without close null points.

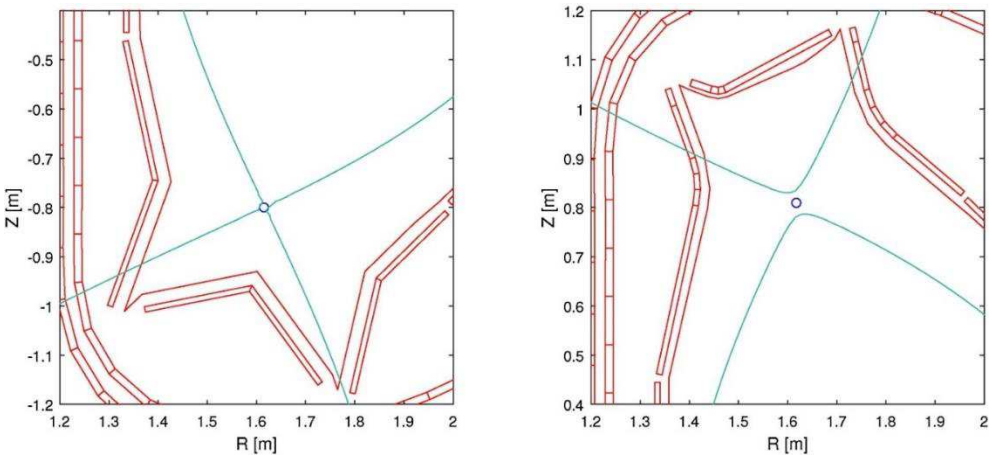

Fig. 4.6 – Static identification of active (left figure) and non-active (right figure) X-point for DN pulse #46530. In blue is reported plasma boundary reconstructed using EFIT database.

In case of alternative configurations with close null points, such as Snowflake, a quadratic expansion is not sufficient to properly fit the flux map in the vicinity of the null points and alternative solutions might entail a higher order polynomial fitting or a numerical estimate of the poloidal flux gradient over a finer grid.

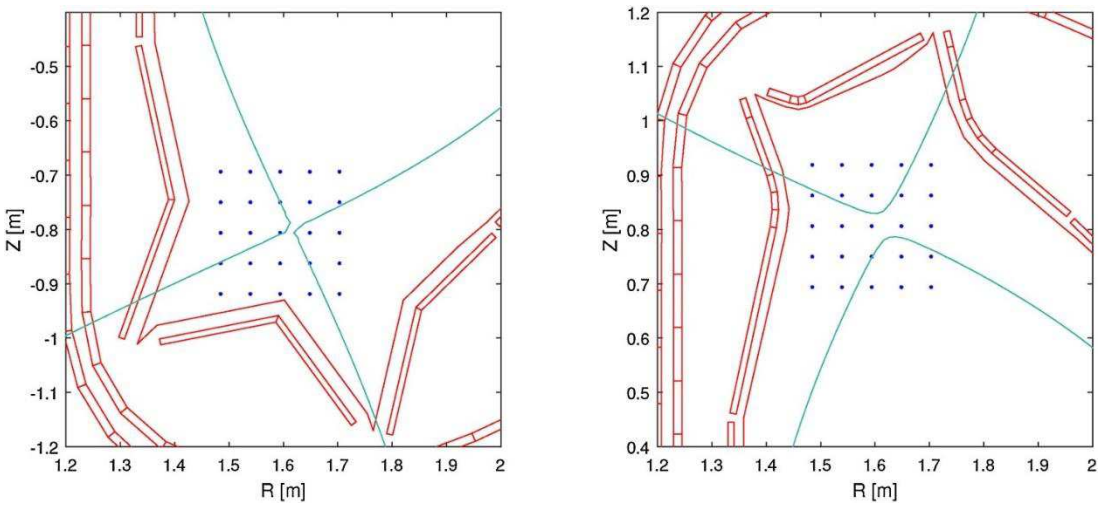

Fig. 4.7 – Box of virtual flux sensors used to estimate position and flux of lower X-point (left) and upper X-point (right). The reconstruction of plasma boundary for DN pulse #46530 at 3 s from EFIT database is reported in blue color.

4.2.3 Open loop validation

In this section, comparison between experimental and open loop simulated data in terms of plasma current, radial and vertical position of plasma centroid, radial and vertical position and flux of both active and non-active X-point, magnetic field and flux measurements and fluxes on control segments will be presented. Since elongated plasmas are vertically unstable, a procedure to simulate backward in time the unstable eigenvalue has been employed (more references can be found in [41]) using as inputs the currents on active circuits, an equivalent plasma voltage and the profile parameters poloidal beta and internal inductance (treated as disturbances). The simulations have been performed using Matlab software. Figs. 4.8 – 4.13 report the results of the comparisons. The slight mismatch between simulated and experimental results is related to the estimation of the eddy currents in the passive structures and hence to the estimated resistivity of the discretized vessel elements [42].

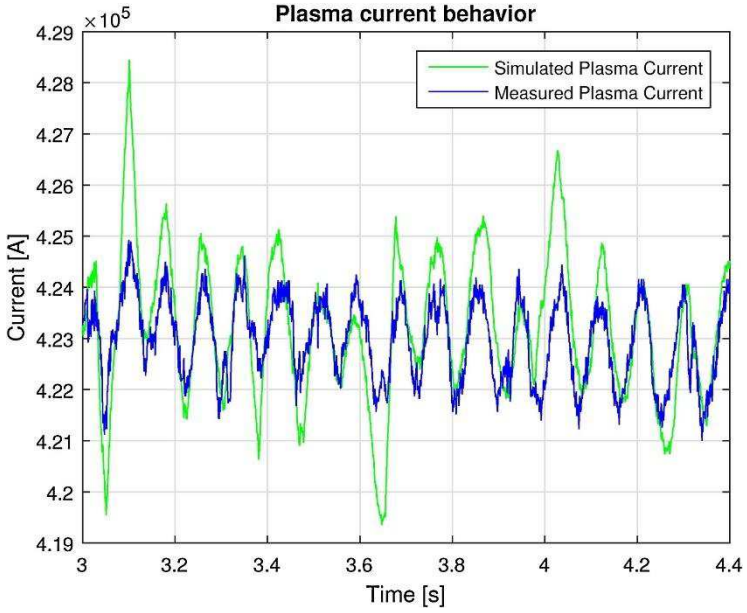

Fig. 4.8 – Comparison between simulated plasma current (green solid line) and experimental plasma current (blue solid line) for pulse #69449.

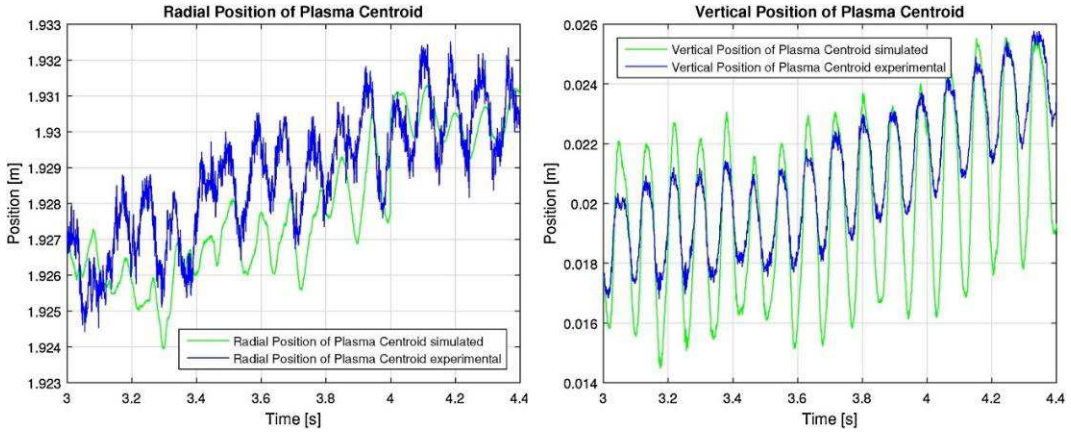

Fig. 4.9 – Comparison between simulated (green solid line) and experimental (blue solid line) plasma centroid radial (left figure) and vertical (right figure) position for pulse #69449

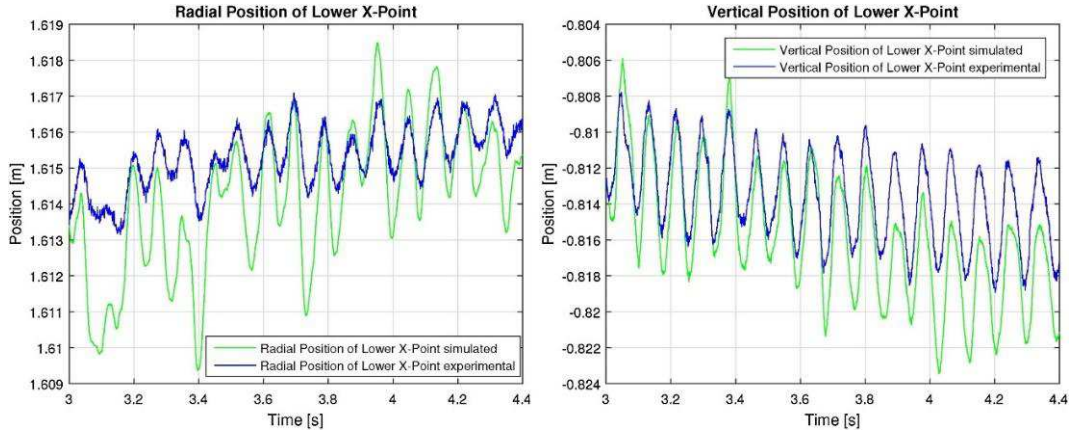

Fig. 4.10 – Comparison between simulated (green solid line) and experimental (blue solid line) plasma Lower X-point radial (left figure) and vertical (right figure) position for pulse #69449.

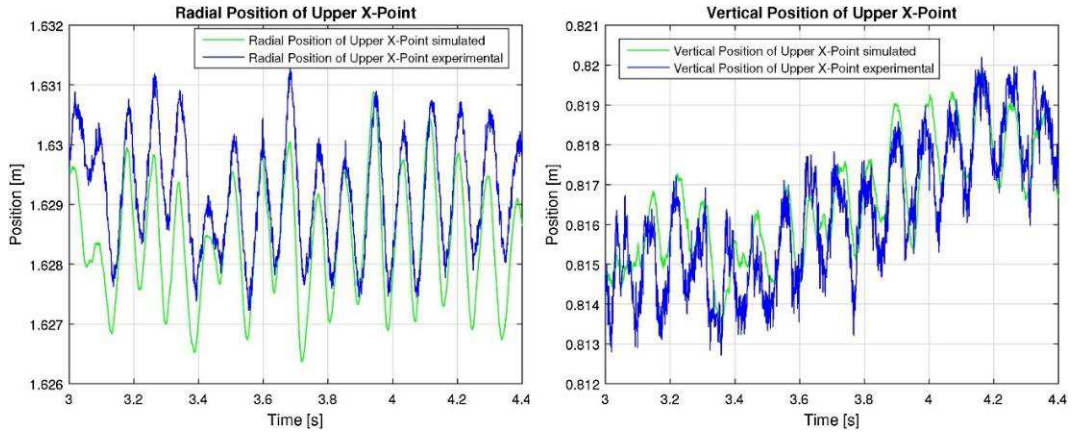

Fig. 4.11 – Comparison between simulated (green solid line) and experimental (blue solid line) plasma Upper X-point radial (left figure) and vertical (right figure) position for pulse #69449.

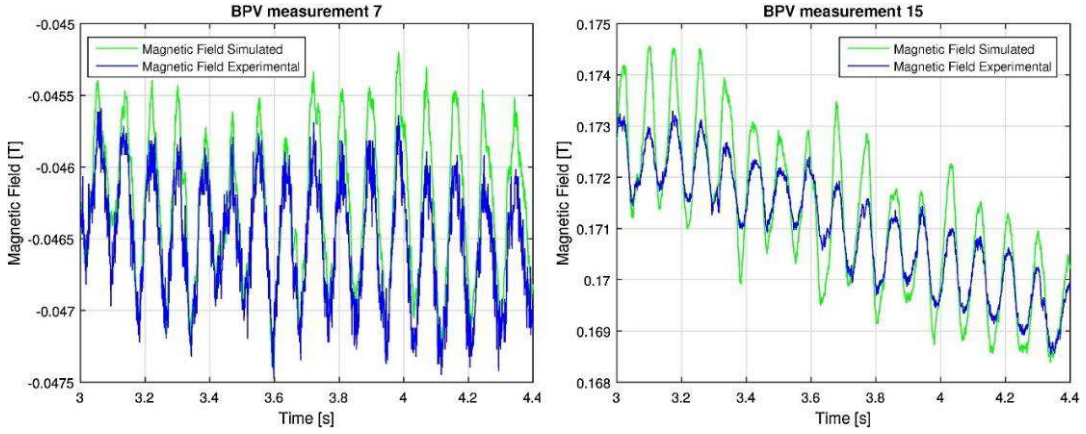

Fig. 4.12 – Comparison between simulated (green solid line) and experimental (blue solid line) magnetic measurements BPV 7 (left figure) and BPV 15 (right figure) for pulse #69449.

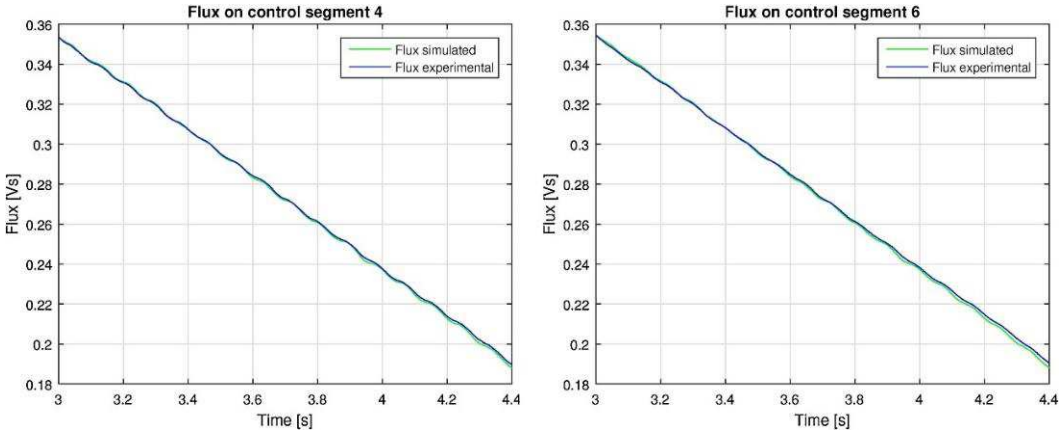

Fig. 4.13 – Comparison between simulated (green solid line) and experimental (blue solid line) magnetic flux for control segment 4 (left figure) and 6 (right figure) for pulse #69449.

4.3 DEMO research activity

In this Section, the research activity carried out on DEMO device will be presented. The main activities performed on DEMO device can be summarized as follows:

- Definition of a procedure for the PF coil system optimization;
- Design of reference and alternative magnetic configurations;
- Preliminary vertical stability analysis of reference and alternative magnetic configurations;

4.3.1 Optimization procedure for the design of the PF coil system for DEMO

The design of the CS/PF coil system of a tokamak is a complex problem due to the nonlinear relation between the plasma shape variation and the currents in the CS/PF coils [53]. Moreover, a set of geometrical and technological constraints related to the port locations, the maximum current density, magnetic fields and vertical forces on the coils must be satisfied. The previous considerations make the optimization of the number, position and dimension of the PF coils a challenging task in the design of the next generation fusion reactors. Different methods have been proposed in the literature for the

optimization of the currents of the PF coils while keeping their positions fixed [43-46]. Other methods try to optimize also the coil positions using nonlinear optimization procedures based on Newton's methods ([47-49]) or genetic algorithms.

In this section, an optimization procedure of the PF/CS coil system is proposed. Given a reference plasma scenario, the procedure focuses on the most critical configurations, typically those at start (SOF) and end of flat top (EOF), assuming that all the remaining equilibria are less demanding in terms of forces, currents and fields. This assumption should therefore be verified a-posteriori. The procedure is able to optimize PF coils number, position and dimension guarantying all the machine technological constraints. This approach is an extension of the procedure used for the optimization of the PF coil currents in existing devices [50-51] and it is based on linearized plasma model (2.46-2.47) presented in Section 2.5. Starting from plasma linearized model, a quadratic optimization problem with linear and quadratic constraints is solved. The proposed procedure simplifies the nonlinear computations needed for Tokamak design and has been successfully applied to the DEMO case. In Section 4.3.1.1 the method proposed will be accurately described while in Section 4.3.1.2 the constraints to be met will be presented. In Section 4.3.1.3 The optimization procedure, which is employed to choose the best PF coil system candidate, will be shown while in Section 4.3.1.4 the proposed technique will be applied to DEMO Single Null case.

4.3.1.1 Method description

The design of the PF coil system consists in the selection of an optimized number, position and cross-section of the PF coils suitable to produce a desired plasma scenario (plasma current profile and shape in different phases of a plasma shot). The optimized PF coils system has to guarantee a set of geometric constraints posed by the mechanical structures, the access specifications (e.g., ports, interference with the toroidal field (TF) coil system, etc.) and the plasma scenario operational constraints (e.g., bounds on the possible variations of the plasma parameters). As stated in the previous Section, the procedure considers on the most critical configurations, typically those at start (SOF) and end of flat top (EOF), assuming that all the remaining equilibria are less demanding in

terms of forces, currents and fields however, the procedure can be easily applied on an increased number of plasma snapshots, such as ramp-up and ramp-down equilibria or possible outliers of the reference plasma scenario.

4.3.1.2 Constraints definition

In the following, a detailed description of the main constraints considered for the design of a tokamak PF coil systems is proposed.

PF coil currents

The cross-sections of the PF coils are determined by the maximum current density J_{max} $[A/m^2]$ in the coils. This limit is a gross value that takes into account the conductor jacket and the winding packs. In the optimization procedure, the PF coil current limits turn out into linear constraints on the optimization variables $I_{CS/PF}$ in the form:

(4.10) $I^i_{CS/PF} \leq I^i_{max} \qquad i = 1 \dots N_{CS/PF}$

Where $I_{CS/PF}$ is vector of currents in Central Solenoid (CS) and PF coils; $N_{CS/PF}$ indicates the total number of PF and CS coils; I^i_{max} is the current limits in the i-th coil whose value depends on the current density limit J_{max} and the maximum area imposed for the coil. For DEMO, the current density limit in DEMO is $J_{max} = 12.5\ MA/m^2$ for all the CS/PF coils. The dimension and position of the CS stack has been fixed accordingly to the maximum magnetic field constraint [54], while the maximum area of the PF coils has been imposed equal to $4\ m^2$, corresponding to a maximum current in a single PF coil of $50\ MA\ turns$.

Magnetic fields

For a safe design of the conductors and the winding packs, a constraint on the maximum poloidal magnetic field B^{max}_{pol} at the location of the PF and CS coils needs to be imposed. For an almost fixed plasma shape and current, the variation of the poloidal magnetic field

in the CS/PF coil locations δB_{pol} during a plasma scenario depends linearly on the variation of the currents flowing in the coils $\delta I_{CS/PF}$, that is:

(4.11) $\delta B_{pol} = C_{B_{pol}} \delta I_{CS/PF}$

where $C_{B_{pol}} \in R^{N_{CS/PF} \times N_{CS/PF}}$ is part the output matrix in the linearized model in (2.47). Concerning the CS stack, as matter of fact, the maximum operating magnetic field is found at the premagnetization, that is the initial instant of a plasma scenario when the CS modules carry the maximum current needed for the inductive plasma heating. Indeed, the width and position of the CS stack is usually done with an analytic premagnetization analysis able to guarantee the constraint of the maximum poloidal magnetic field [55]. For DEMO, the maximum magnetic field at the location of the PF and CS coils for a safe design of the conductors and the winding packs shall not exceed $12.5\ T$.

Vertical forces on the PF/CS coils

The independently fed PF/CS coils create large electromagnetic forces on the mechanical structures that pull in different directions. While the radial component of the electromagnetic force is balanced in axisymmetric tokamak, the vertical component needs to be bounded to lead the mechanical loads to acceptable values. Vertical forces on the coils are proportional to the currents flowing in the coils and to the radial magnetic field in the coil location. Hence, for an almost fixed plasma shape and current, a quadratic dependence of the vertical forces on the PF/CS currents can be imposed. Vertical force constraints can be distinguished in:

- Maximum vertical force on a single PF coil

(4.12) $\left|F_{PF}^{i}\right| \leq F_{PFmax}^{i} \qquad i = 1 \dots N_{PF}$

where N_{PF} indicates the number of PF coils and F_{PFmax}^{i} indicates the vertical force limit

on the i-th PF coil. For DEMO, the maximum vertical force on a single PF shall not exceed $450\ MN$;

- Maximum vertical force on the CS stack

(4.13) $\left|\sum_{i=1}^{N_{CS}} F_{CS}^{i}\right| \leq F_{max}^{CS}$

where N_{CS} indicates the number of PF coils and F_{max}^{CS} indicates the vertical force limit on the CS. For DEMO, the maximum vertical force on the CS stack shall not exceed $300\ MN$;

- Maximum separation force among the CS elements. Assuming the CS coils ordered from the top to the bottom, the separation force constraints are defined as:

(4.14) $\sum_{i=1}^{k} F_{CS}^{i} \leq F_{sep\_up\_max}^{CS} \qquad i = 1 \dots N_{CS}$

(4.15) $\sum_{i=1}^{k} F_{CS}^{N_{CS}-i+1} \geq -F_{sep\_down\_max}^{CS} \qquad i = 1 \dots N_{CS}$

where $F_{sep\_up\_max}^{CS}$ and $F_{sep\_down\_max}^{CS}$ indicate the absolute value of the vertical up and down separation force limits among the CS elements. For DEMO, the maximum separation force in the CS stack shall not exceed $350\ MN$.

Plasma separatrix

Constraints on the plasma separatrix need to be imposed in order to ensure safe conditions for the plasma electromagnetic control and to reduce the power load on the plasma facing components. Indeed:

- To reduce the power load on the plasma facing components (PFCs) and to allow safe transient conditions in case of minor disruptions and L/H-H/L transitions, a minimum plasma-wall distance d_{min} needs to be guaranteed. Once the reference

plasma shape is fixed, as stated in equation (2.47), a linear relation between the variation of the gaps δg and the variation of the currents $\delta I_{CS/PF}$ can be used to fulfill this constraint. For DEMO, the minimum plasma-wall distance should be $0.225\ m$;

- To limit the power load on the divertor plate the grazing angle θ_g of the magnetic field at the strike points should be minimized [56]. However, for the divertor safe conditions, the minimum grazing angle in experimental fusion devices is around 1.5°;
- To maximize the fusion power performance, certain bounds are also imposed on the plasma triangularity and elongation and on the minimum flux swing at flat-top [57]. For DEMO, reference plasma triangularity and elongation at 95% of the separatrix are set to $\delta_{95\%} = 0.33$ and $\delta_{95\%} = 1.65$ respectively while the reference flat-top flux swing is set to about $300\ Vs$.

4.3.1.3 Optimization procedure

In the following, it is assumed that the poloidal geometry of the device (first wall, divertor structure, vessel shells and TF coil shells) is already fixed. Moreover, the position and dimension of the CS stack has been already optimized in order to guarantee the poloidal magnetic field constraint at the premagnetization phase [55]. The proposed optimization procedure can be summarized as follows:

- Definition of a preliminary redundant PF coils system compatible with the available space, as shown in Fig. 4.14;
- Design the MHD equilibrium and linearized model for the set of the most critical plasma snapshots to be considered in the optimization using the redundant PF coils system;
- For each of the plasma snapshots, implement an exhaustive analysis of the candidate PF coil systems composed by a fixed number n of external PF coils, chosen from the redundant system, able to guarantee the currents and forces constraints while maintaining the desired plasma shape within a certain tolerance;
- Select the best candidate PF coil system compatible with all the plasma snapshots;

The procedure is implemented in terms of a quadratic optimization problem with linear and quadratic constraints. The idea beneath the optimization procedure is the definition of a linearized model that relates the variation of the currents in the redundant CS/PF coil system $\delta I_{CS/PF}$ to the variation of the quantities related to the constraints listed in the previous Section. Therefore, the analysis of the i-th candidate PF coil systems turns out into an optimization problem over the linearized model implemented on a selected subset of the redundant coils:

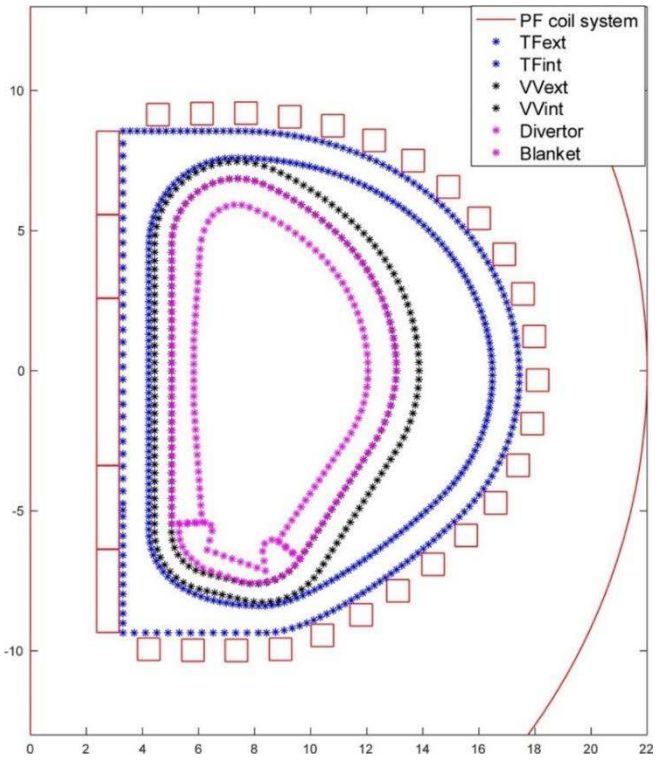

Fig. 4.14 – Redundant PF coils systems compatible with the 2017 DEMO device geometrical description

$$(4.16)\quad \min_{\delta I^i_{CS/PF}} \left(I^i_{eq} + \delta I^i_{CS/PF}\right)^T \left(I^i_{eq} + \delta I^i_{CS/PF}\right)$$

subject to:

$$(4.17)\quad \left\| C_G S_i^T \delta I^i_{CS/PF} \right\| < \Delta g$$

$$(4.18)\quad \left\| B^i_{eq} + C_{B_{pol}} S_i^T \delta I^i_{CS/PF} \right\| < B^i_{max}$$

$$(4.19)\quad \left\| I^i_{eq} + \delta I^i_{CS/PF} \right\| < I^i_{max}$$

(4.20) $\left\| C_{\Psi_b(t)} S_i^T \delta I_{CS/PF}^i \right\| < \varepsilon$

and the vertical force constraints (4.12) – (4.15) where:

- $S_i \in R^{n \times N_{CS/PF}}$ is a selection matrix picking the coils of the i-th candidate PF coil system among all the PF coils of the redundant system;
- $I_{eq}^i \in R^n$ is the vector of CS/PF currents in the coils of the i-th candidate PF coil system at the reference equilibrium evaluated as $I_{eq}^i = (C_G S_i^T)^\dagger C_G I_{eq}$ with $I_{eq} \in R^{N_{CS/PF}}$ the vector of CS/PF currents in the redundant PF coil system at the reference equilibrium;
- $\delta I_{CS/PF}^i$ are the optimized CS/PF current variations in the coils of the i-th candidate PF coil system. The total optimized currents are $I_{opt}^i = I_{eq}^i + \delta I_{CS/PF}^i$;
- $B_{eq}^i \in R^n$ is the vector of the poloidal magnetic field in the coil locations of the i-th candidate PF coil system;
- Δg indicates the maximum acceptable variation of the gaps with respect to the reference configuration;
- $C_{\Psi_b(t)}$ is the output matrix related to the magnetic flux at the plasma boundary and ε indicate the admissible variation of the boundary flux in the optimization problem (ideally $\varepsilon \to 0$ in order to maintain the boundary flux of the reference configuration)

Note that the inequalities (4.17) - (4.20) can be easily converted into linear constraints with respect to the optimization variables $\delta I_{CS/PF}$ defining, with the quadratic objective function (4.16), a convex LQ optimization problem [58]-[59].

Concerning the vertical force constraints, it is possible to express the vector of the vertical forces on the PF coils of the i-th candidate PF coil systems as:

(4.21) $F_{CS/PF}^i = \left(B_{eq}^i + C_{B_{pol}} S_i^T \delta I_{CS/PF} \right) \circ \left(I_{eq}^i + \delta I^i{}_{CS/PF} \right)$

where ∘ indicates the Hadamard product. Therefore, the inequalities (4.12) - (4.15) define quadratic constraints that are not compatible with the LQ formulation and hence give rise

to the definition of a non-convex optimization problem whose solution is strongly affected by the initial condition. The proposed strategy for the definition of the optimized PF coil system is therefore divided in two steps. A preliminary optimization phase where the LQ optimization problem (4.16) - (4.20) is solved for all the candidates PF coil systems. This phase allows a drastic reduction of the cases among which the optimal PF coil system could be determined with a huge reduction of the computing time. A second phase where the non-convex quadratic optimization problem with quadratic constraints is then implemented on the remaining PF coils system candidates assuming as initial condition the solution of the LQ optimization problems.

4.3.1.4 Application to DEMO Single Null case

The design of a fusion device is usually performed using systems codes able to assess the engineering and economic viability of a hypothetical fusion power station using simple models of all parts of a reactor system. For DEMO device, the systems code PROCESS [60] is used to identify the relevant parameters assuming a net-electric power output of $500\ MW$. In the present Section the proposed PF coil optimization algorithm is applied on the DEMO Single Null baseline 2017 whose main parameters defined by PROCESS [54] are reported in Table 4.1. Once the DEMO relevant parameters have been identified, a reference plasma shape is defined geometrically. Then, the geometry of the machine, i.e. first wall, divertor structure, vessel and TF coil shells, is designed; dimension and position of the components are then optimized taking into account their realistic realization, as shown in Fig. 4.14. Finally, the reference plasma scenario composed by the pre-magnetization, the start of flat top (SOF) and end of flat top (EOF) is designed assuming a non-optimized PF coil system, as shown in Fig. 4.15. The dimension and position of the CS stack is fixed in accordance with to the maximum magnetic field constraint [54]. The premagnetization flux is around $\Psi(t_{BD}) = 310\ Vs$; the flux at SOF is identified using the Ejima formula [57] while the flux at EOF is defined as minimum flux reachable at flat top maintaining an almost fixed plasma separatrix and it is mainly related to the capability of the CS stack. In order to define an optimized set of PF coils

satisfying all the currents and vertical forces constraints, a redundant set of 30 coils (5 for the CS and 25 for the PF, respectively) compatible with the available space limited by the outer TF shell has been produced, as shown in Fig. 4.16.

Table 4.1 – Main parameters of DEMO baseline 2017 defined by PROCESS [54]

Geometrical parameters		
Major radius	R_0 (m)	8.938 m
Minor radius	a (m)	2.883 m
Aspect ratio	A	3.10
Elongation	$k_{95\%}$	1.65
Triangularity	$\delta_{95\%}$	0.33
Volume	V	2266 m^3
Magnetic field on axis	B_0	4.89 T
Plasma physic parameters		
Plasma current	Ip	$19.07MA$
Poloidal beta	β_{pol}	1.141
Internal inductance	l_i	0.8

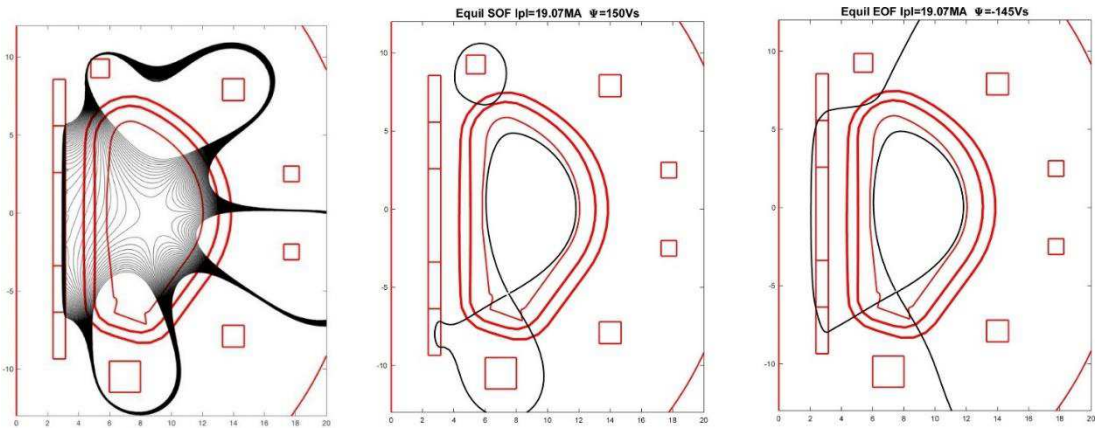

Fig. 4.15 – Plasma scenario at premagnetization, SOF and EOF

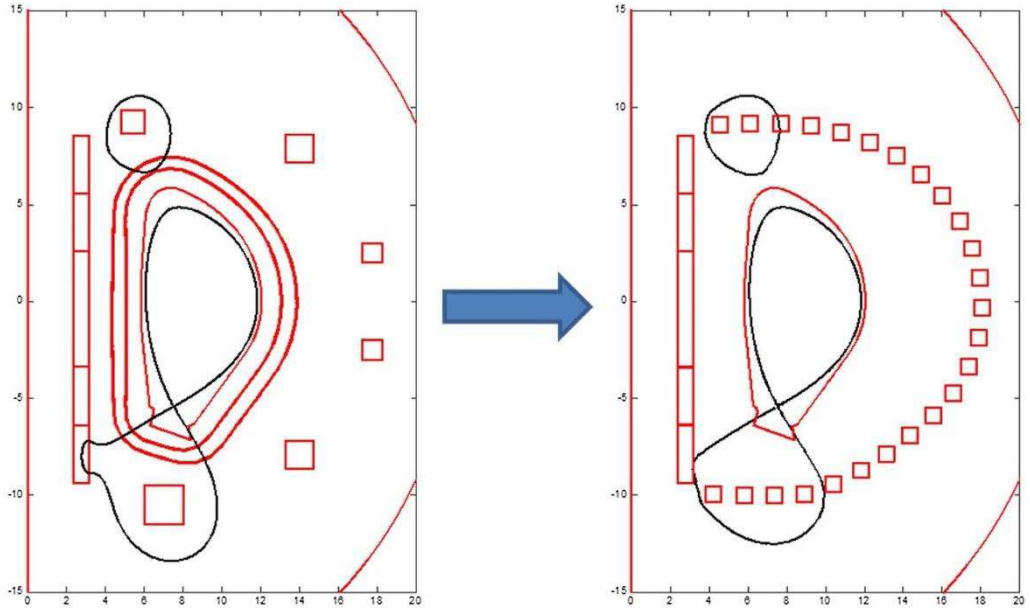

Fig. 4.16 – Redundant PF coil system for the 2017 SN baseline

All the PF coils have the same cross-section of 0.64 m^2. The number of possible PF coil systems composed by 6 over 25 PF coils is given by $\binom{25}{6} = 177100$. However, this number has been reduced to 5005 considering a constraint on the minimum distance between the centers of the cross sections of adjacent coils center, i.e. $d \geq 3m$. In the present analysis, possible geometric constraints (e.g., port locations for diagnostics, additional heating and remote maintenance) are only considered in the post-processing of the solutions.

An exhaustive analysis of the 5005 candidate PF coil systems has been then carried out in order to find SOF and EOF configurations able to maximize the flat-top flux swing while maintaining the desired plasma shape within a certain tolerance and verifying all field and vertical force constraints summarized in Section 4.31.2.

The exhaustive analysis has been performed using the CREATE-NL [37] equilibrium code and the CREATE-L [12] linearization code solving first an LQ minimization problem (4.16) - (4.20) in order to reduce the coil sets among which the optimal PF coil system could be determined. Finally the quadratic constraints (4.12) - (4.15) related to the force limits have been added.

Equilibrium and linearization evaluation with a course finite element triangular mesh of 13000 points required a CPU time of about 300s, whereas the full exhaustive analysis

took additional 200s (to be repeated at SOF and EOF) on a MacBook Pro 2.5 GHz Intel Core i7.

Due to the high number of PF coils solutions able to guarantee all the constraints in Section 4.3.1.2, it is possible to perform the analysis of a subset of PF coil systems which are characterized by vertical forces on the PF coils are below $200\,MN$. Six possible solutions have been found and shown in Fig. 4.17. Table 4.2 reports the main costs and constrained quantities of the selected PF coil systems. According with Table 4.2, the six PF coil systems are almost equivalent. However, to allow the presence of an adequate equatorial access port, the final choice went to the solution "2883".

For this configuration, a PF coil system with the 6 selected PF coils of appropriate dimensions has been produced. The set of PF coil currents defined by the optimization problem at SOF and EOF has been used to fix the dimension of the coils according to the current density constraint of $J_{max} = 12.5\ MA/m^2$. Moreover, a slight modification of the PF coil positions has been imposed to ensure a distance from the TF coil outer shell of $10\ cm$. Fig. 4.18 shows the optimized PF coil system with the equilibria at SOF (magenta) and EOF (black) evaluated with the CREATE-NL equilibrium code.

Table 4.2 – Costs and constraints of the candidate PF coil system

Costs \ PF coil system	**Flux swing at flat top (V·s)**	**$\Sigma\lvert I_{PF/CS}\rvert_{max}$ (MAturns)**	**Max PF coils current (MAturns)**	**Max. force on a single coil $F_{z,PF}$ (MN)**	**Max. vertical force on CS $F^{total}_{z,CS}$ (MN)**	**Max. CS separation force $F^{sep}_{z,CS}$ (MN)**
2883	298.27	179.74	14.95	149.26	131.47	131.47
2924	298.27	180.36	15.46	157.54	132.18	132.18
2939	298.27	180.14	15.23	151.12	128.04	128.04
2949	298.27	179.67	15.29	146.5	127.51	127.51
3050	298.25	179.99	15.56	151.04	134.73	134.73
3065	298.27	180.4	15.29	153.26	133.53	133.53

Table 4.3 shows that the optimization of the PF coil systems does not affect the flux swing between SOF and EOF (it is mainly related to the CS coils) while a 20% improvement can be noted on the maximum vertical force on the CS and PF coils. A fruitful application of the proposed procedure has been applied successfully to the ITER case [53].

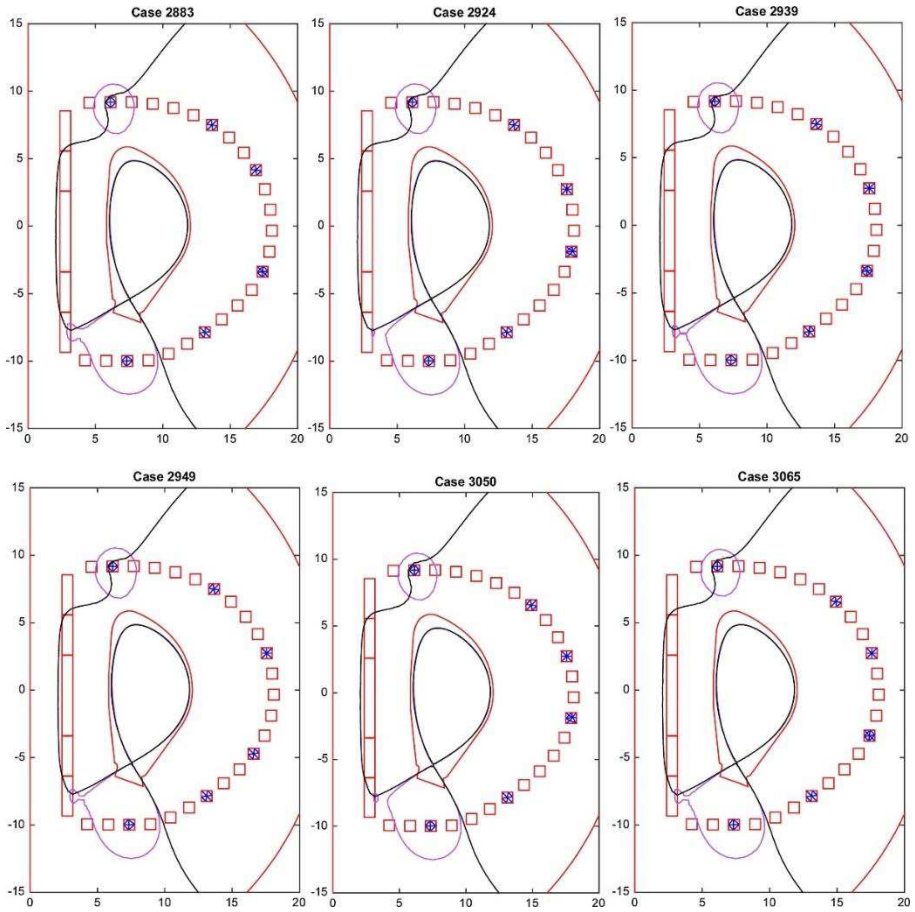

Fig. 4.17 – Candidate PF coil systems verifying the constraints with the maximum vertical force on a single PF coil below 200 MN at flat-top

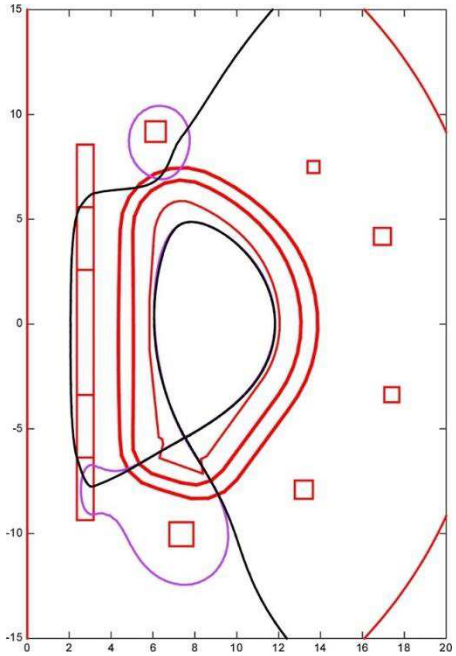

Fig. 4.18 – SOF (magenta) and EOF (black) optimized Single Null configurations

Table 4.3 – Costs and constraints of the candidate PF coil system

Costs \ PF coil system	**Flux swing at flat top (V·s)**	**$\Sigma\lvert I_{PF/CS}\rvert_{max}$ (MAturns)**	**Max PF coils current density (MA/m^2)**	**Max. force on single coil $F_{z,PF}$ (MN)**	**Max. vertical force on CS $F^{total}_{z,CS}$ (MN)**	**Max. CS separation force $F^{sep}_{z,CS}$ (MN)**
original	295.72	182.68	12.49	181.14	145.63	145.63
"2883"	298.27	179.74	14.95	149.26	131.47	131.47
optimized	298.10	181.47	12.50	145.29	111.72	111.72

4.3.2 Design of alternative magnetic configurations for DEMO

In this section, alternative magnetic configurations for DEMO tokamak will be presented [61]. A conventional DEMO design based on a SND configuration serves as a reference, which the alternative solutions are compared against. As stated in Section 4.3.1.4, PROCESS system code is used to identify the main parameters of the reference SND configuration. In Table 4.4, the key machine and plasma parameters [62] of the SND reference are reported.

Table 4.4 – DEMO SND reference scenario

Machine parameters		
Major radius	R_0 (m)	8.77 m
Aspect ratio	A	3.10
Elongation	κ_{95}	1.55
Volume	V	2214 m^3
Magnetic field on axis	B_0	5.80 T
Plasma current	I_P	20.3 MA

The optimization procedure, which is carried out for each AC, is an iterative procedure composed of two main steps. In the first step, given a reference plasma shape that features the main characteristic of an alternative divertor concept, the geometry of the machine (first wall, vessel and TF coil) is optimized by means of the NOVA optimization code. In the second step an optimization of the PF coil system (number, position and current in the

PF coils) is performed in order to find a finite set of PF coils able to maximize the flat top flux swing of the respective alternative configuration until the reference value of 240 Vs imposed for the SND baseline is reached while satisfying the PF coil currents and vertical forces constraints [37]-[53]. The constraints considered for the optimizations of the configurations have been reported in Section 4.3.1.2. In Section 4.3.2.1 the figure of merits which characterize the alternative divertor concepts will be provided. In Section 4.3.2.2 the design of DEMO alternative configurations will be presented while in Section 4.3.2.3 an analysis of costs and benefits of alternative configurations will be tackled.

4.3.2.1 Figure of merits

In order to evaluate the possible benefits of alternative magnetic configurations in the following, a brief description of the main figure of merits the will be provided.

Shape parameters

- $\boldsymbol{\kappa_{95\%}}$: plasma elongation at 95% of the flux difference between the axis and the separatrix.
- $\boldsymbol{\delta_{95\%}}$: plasma triangularity at 95% of the flux difference between the axis and the separatrix.
- $\boldsymbol{V_{pl}}$: plasma volume.
- $\boldsymbol{V_{TF}/V_{pl}}$: the ratio of the volume inside the inner shell of the TF coil and the plasma volume.

X-point parameters

- Gradient $\boldsymbol{|\nabla B_{p,xpt}|}$: gradient of the poloidal magnetic field at the X-point.
- $\boldsymbol{R_{xpt}}$: major radius of the X-point.
- $\boldsymbol{V_{SOL}}$: volume of the Scrape Off Layer (SOL) from the separatrix to the flux surface with an outboard midplane separatrix distance of $\rho = 1mm$ and $\rho = 3mm$.

Target parameters

- $\boldsymbol{L_p}$: poloidal connection length from the outer equatorial plane to the target.
- $\boldsymbol{L_{||}}$: parallel connection length from the outer equatorial plane to the target on the flux surface with an outboard midplane separatrix distance of $\rho = 1mm$ and $\rho = 3mm$.
- $\boldsymbol{f_{x,t}/f_{x,min}}$: the ratio of the flux expansion at the target and the minimum flux expansion along the divertor leg.
- $\boldsymbol{f_{x,t}}$: flux expansion at the target.
- $\boldsymbol{R_t/R_x}$: the ratio of the major radii of the target and the X-point.
- $\boldsymbol{\gamma_t}$: grazing angle of the magnetic field line at the target plate.
- $\boldsymbol{\beta_t}$: poloidal angle between the separatrix and the target plate.

4.3.2.2 DEMO ADCs

SN configuration

The optimized SN configuration has been realized using a CS/PF coil system composed by 5CS coils and 6PF coils, as shown in Figure 4.19.

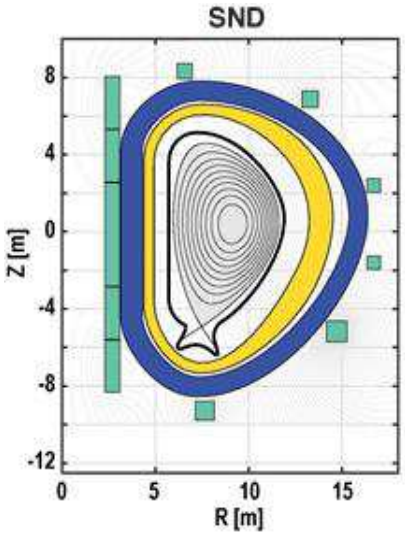

Fig. 4.19 – Optimized SND configuration

An optimization of the PF coil system is realized to maximize the flat-top flux swing verifying all the field, current density and vertical forces constraints on the PF coil system. The flat top flux swing of the SN configuration is 240Vs. Table 4.5 reports the main geometric characteristics of the ADCs evaluated at SOF.

Table 4.5 – Geometric parameters of the DEMO configurations

		SND		XD		SXD		SFD		DND
Shape	Elongation $\kappa_{95\%}$	1.55		1.57		1.56		1.55		1.55
	Triangularity $\delta_{95\%}$	0.34		0.27		0.34		0.25		0.34
	Volume V_{pl} $[m^3]$	2050		2100		2080		2060		2020
X-point	R_{xpt} [m]	7.47		6.98		7.17		7.64		7.4
	Gradient $\lvert\nabla B_{p,xpt}\rvert$ [T/m]	0.434		0.322		0.287		0.016		0.557
	V_{SOL} (ρ=1mm) [m]	5.62		8.05		7.33		17.3		3.78
	V_{SOL} (ρ =3mm) [m]	15.1		21.3		19.6		36.2		10.1
Targets		SN		XD		SXD		SFD		DND
		in	out	in	out	in	out	in	out	out
	L_p [m]	18.1	8.5	17.7	10.8	17.7	13.3	18.1	9.5	8.3
	$L_{\lvert\rvert}$ (ρ =1mm) [m]	215	125	237	236	238	217	464	344	104
	$L_{\lvert\rvert}$ (ρ =3mm) [m]	195	105	206	206	210	190	325	223	90
	$f_{x,t}/f_{x,min}$	1	1	1	1.29	1	1	1	1	1
	$f_{x,t}$	5.7	3.8	6.53	12.6	9.05	2.25	10.9	11.3	2.7
	R_t/R_x	0.85	1.11	0.81	1.08	0.87	1.51	0.8	1.16	1.1
	γ_t [Deg.]	1.5	1.7	1.5	1.5	1.54	1.58	1.52	1.54	1.51
	β_t [Deg.]	28.4	20.5	32.5	89	53	11.8	72.4	82.8	13

DN configuration

In accordance with the new geometry, an optimized PF coil system have been produced

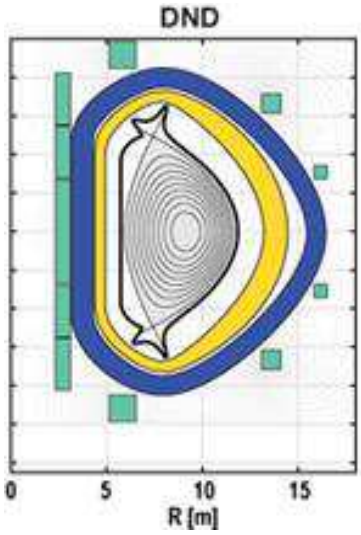

Fig. 4.20 – Optimized DND configuration

for DN configurations at SOF and EOF, as shown in Fig 4.20.

The main parameters of the DN configuration are reported in Table 4.5. SN and DN configurations have a similar lower X-point location and volumes, as shown in Fig. 4.21.

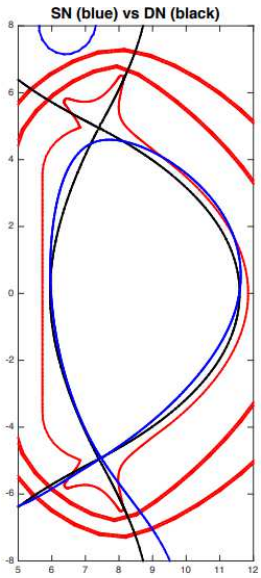

Fig. 4.21 – Comparison between SN and DN shapes

DN configuration has a flat top flux swing of 220VS, around 10% less than the SN case.

SF configuration

Concerning the SF configurations [73], a segmentation of the CS, as shown in Fig. 4.22,

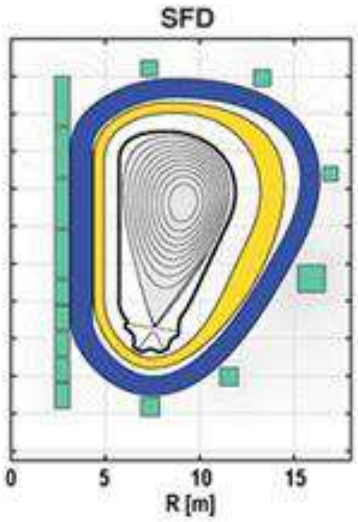

Fig. 4.22 – Optimized SF configuration

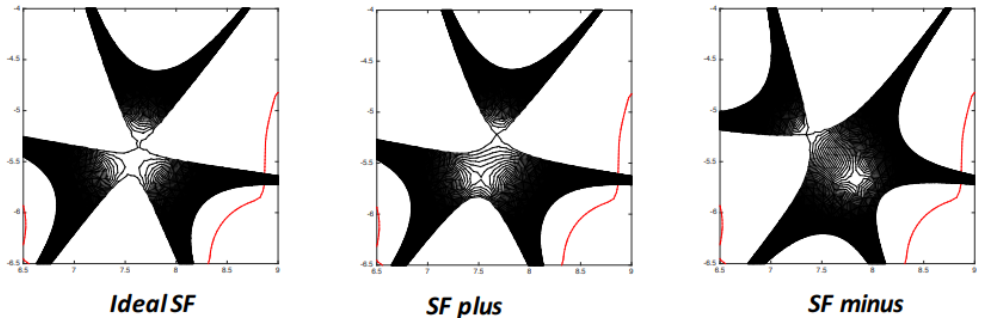

Fig. 4.23 – From left to right: Ideal SF configuration, SF plus and SF minus

has been necessary in order to maximize the Flux Swing. Using the optimized CS stack, it has been possible to increase the SF flat top swing up to 180Vs (about 25% less than the SN case), as indicated in Table 4.5.

Furthermore, since the exact SFD is only a point in the operational plane and any real configuration is characterized by two nearby X-points, a sensitivity analysis has been performed in order to produce Ideal SF, SF- and SF+ configurations as shown in Fig. 4.23.

SX configuration

The design of the SXD configuration has been realized using the same CS of SND and DND configurations and optimizing the positions and sizes of the PF coils. The resulting configuration at SOF is shown in Fig. 4.24.

The main parameters of the SX configuration are reported in Table 4.5. The shape of the SXD is very similar to the reference SN case. The main difference is related to the position of the X-point that has been moved inboard in the SX configuration, as shown in Fig 4.25. SX configuration has a flat top flux swing of 200VS, about 15% less than the SN case. The present SX configuration has been realized with only external coils. The addition of In-Vessel coils would be useful to:

- Increase the flux expansion along the outer leg;
- Increase the connection length;
- Make the flux surfaces diverging on the outer divertor plate

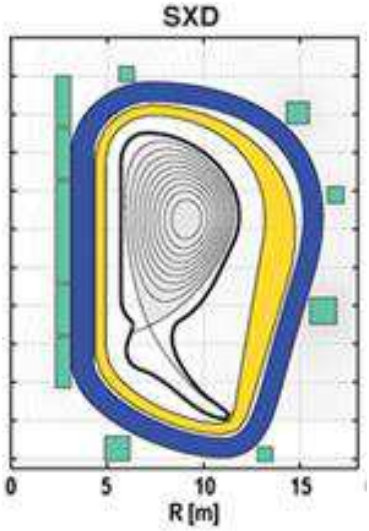

Fig. 4.24 – Optimized SXD configuration

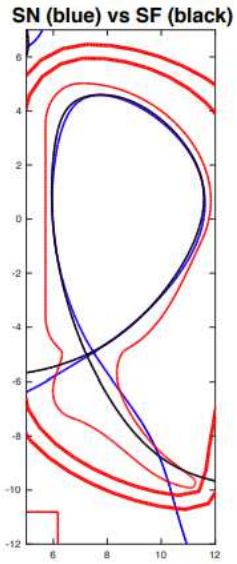

Fig. 4.25 – Comparison between SN and SX

XD configuration

The design of X-Divertor configuration with only external coils has been investigated relaxing the SF configuration previously presented. In accordance with the new geometry, an optimized PF coil system have been produced for XD configurations at SOF and EOF, as shown in Figure 4.26. The outer-XD configuration is characterized by flaring flux surfaces in the vicinity of the divertor plate. Defining $\boldsymbol{f_{x,t}/f_{x,min}}$ as the ratio of the flux

expansion at the target and the minimum flux expansion along the leg, we usually impose for XD configurations $f_{x,t}/f_{x,min}$ > 1.20. Moreover, for the divertor safe conditions, the most critical constraint for the XD is related to the minimum grazing angle should be 1.5°.

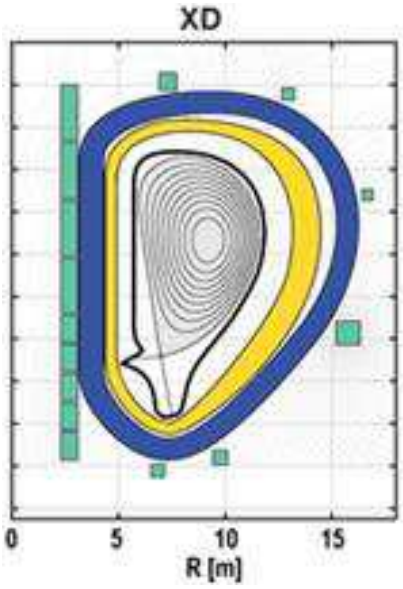

Fig. 4.26 – Optimized XD configuration

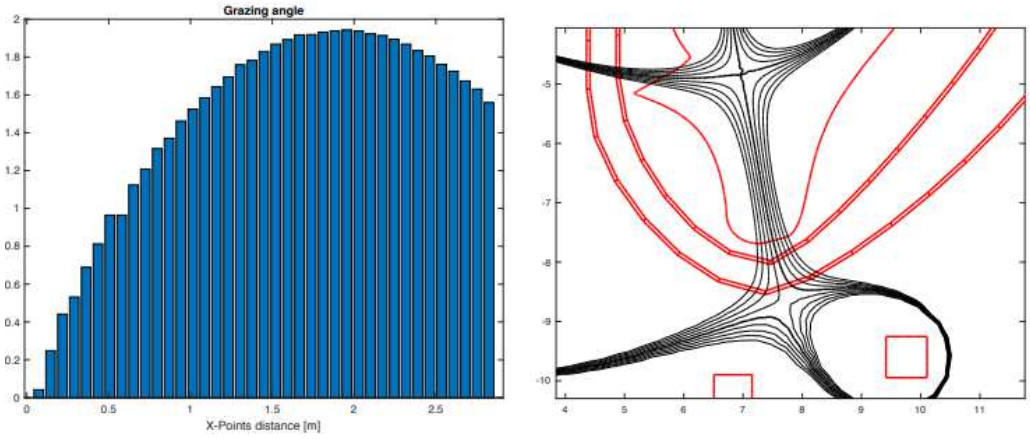

Fig. 4.27 – Grazing angle assuming divertor plates orthogonal to the plasma leg as a function of the distance of the outer divertor plate from the Xpoint for the XD configuration at SOF

In Fig. 4.27 the report of the behavior of the grazing angle (assuming divertor plates orthogonal to the plasma leg) as a function of the distance of the outer divertor plate from the Xpoint for the XD configuration at SOF is reported.

The grazing angle and $f_{x,t}/f_{x,min}$ at the inner and outer plates for the SOF and EOF configurations are reported in Table 4.6. XD configuration has a flat top flux swing of 185VS, very similar to the SF case.

Table 4.6 – Grazing angle and $f_{x,t}/f_{x,min}$ at the inner and outer plates for the SOF and EOF

	$f_{x,t}/f_{x,min}$	grazing angle	
	Outer Target	*Inner target*	*Outer Target*
XD SOF	1.29	1.50	1.50
XD EOF	1.22	1.81	1.74

4.3.2.3 Costs and benefits of alternative magnetic configurations

The feasibility of ACs on DEMO depends on whether there are engineering solutions to build such a device and how much it would cost. In this section, therefore, a distinction between *constraints* described in section 4.3.1.2 that must be met, *costs* and *benefits* of the ACs compared to the reference SN solution is performed, as shown in Table 4.7. The main constraints for the definition of the alternative configurations are related to the vertical forces on the poloidal field coils and the central solenoid. While the margin with which the constraints are met will certainly affect the costs, the total current request and, hence, the volume of the required coil systems is assumed to be the main cost driver. The request for the PF coils refers only to the coils that are placed outside the TF coils as all the configurations produced in 2017 don't make use of in-vessel coils. The current is weighted with the radius of the coil to yield a proxy for the volume and, hence, cost of the coil system. The ratio of TF coil volume and the plasma volume is a proxy for the cost of the TF coils. The normalization accounts for differences in the expected fusion power output of configurations with different plasma volume. Similarly, the flux swing that is available for the flat top will affect the (average) fusion power of a pulsed DEMO. The potential benefits of the ACs arise from the modified magnetic geometry. Several geometric parameters such as the connection length, $L_{\parallel}$, the ratio of the flux expansion

at the target and the minimum flux expansion along the divertor leg, $\boldsymbol{f_{x,t}/f_{x,min}}$ and the ratio of the radial target position and the X-point radius, $\boldsymbol{R_t/R_x}$ have been introduces to quantify the extent of the geometric variations. The parameters of the ACs are evaluated for the outer divertor. Most ACs seek to increase the connection length, $L_{\parallel}$, and with it the SOL volume. The connection length depends strongly on the on the upstream distance of the flux surface to the separatrix, ρ_u. The peak/divergence of $L_{\parallel}$ in the SOL of the SF-minus configuration is related to the presence of the secondary null point.

Table 4.7 – Constraints, costs and benefits of the configurations

		SND	XD	SXD	SFD	DND	Limit
Constraints	Max. force on single coil $F_{z,PF}$ (MN)	94	61	216	349	354	< 450
	Max. vertical force on CS $F_{z,PCS}$ (MN)	75	15	121	16	2	<300
	Max. CS separation force $F_{z,CS}$ (MN)	211	352	325	347	149	< 350
Costs	Max. S $\|I_{PF}\|$ (MA·turns)	154	168	176	188	216	
	Flux swing for current drive (V · S)	240	285	200	180	220	
	V_{TF}/V_{plasma}	3.50	3.61	4.42	3.57	3.60	
Benefits	$L_{\parallel,outer}$ (r_u=1mm) (m)	125	236	217	**344**	104	
	$f_{x,t}/f_{x,min}$	1	**1.29**	1	1	1	
	R_t/R_x	1.11	1.08	**1.51**	1.16	1.1	

4.3.3 Vertical stability and shape sensitivity analysis of DEMO Single Null and alternative configurations

Tokamak plasmas with elongated cross-sections show an inherent axisymmetric vertical instability [63]. This means that without corrective actions, any perturbation displacing the plasma's axisymmetric vertical position from an equilibrium position would grow

exponentially, leading to a so-called vertical displacement event (VDE). Without any conductive wall, this instability would take place on the very fast Alfvén time scale (typically μs); conversely, plasma perturbations may induce eddy currents in the surrounding conducting structures, which tend to counteract the instability itself. This stabilizing effect lasts until the eddy currents decay due to nonvanishing resistivity, thus intuitively explaining why such instabilities can be slowed down to electromagnetic timescales (typically milliseconds) [63]. Thanks to this effect, a suitable magnetic active feedback controller acting on poloidal field (PF) coils may be designed, that can stabilize the vertical position. The vertical stabilization system is hence a key feature of any elongated tokamak device, either existing or under design [64]. The design of such a feedback controller depend on the growth rate of the vertical instability. Hence, it is crucial to correctly estimate such quantities, which critically depend on a correct description of the conducting structures [65]. In Section 4.3.3.1 the vertical stability analysis of standard and alternative configurations will be proposed. In Section 4.3.3.2 a shape sensitivity analysis of the configurations will be presented.

4.3.3.1 Vertical stability analysis

In this section the assessment of the vertical stability performance of the 2017 ADCs is performed in terms of active and passive vertical stability parameters assuming a vertical stabilization system composed by external coils. The analysis is carried out at flat top considering the following set of disturbances:

- 5cm VDE,
- ELM ($\Delta l_i = 0.1$, $\Delta\beta_{pol} = -0.1$)
- MD ($\Delta li = -0.1$, $\Delta\beta_{pol} = -0.1$)

The assessment of the active vertical stability performance is done in terms of best achievable performance. Indeed, a constant voltage αV_0 is imposed on the imbalance circuit composed by the coils PF2-PF3-PF4-PF5 (Fig. 4.26), where V_0 is the minimum voltage able to stop the plasma vertical unstable mode for $t \to \infty$ and $\alpha \in R$ is a constant value fixed equal to 5. In accordance to our experience in DEMO and other fusion reactors

(JET, ITER…) the power request given by the best achievable performance with a constant voltage $5V_0$ is a good estimation of the real power request given by a feedback vertical control system. In Fig. 4.28 it is also shown the imbalance circuit considered for the vertical stabilization has been reported. DEMO active stabilization circuit has the same structure as the ITER VS1 circuit [74]: poloidal field coils PF2 and PF3 are in parallel whereas PF4 and PF5 are in anti-parallel.

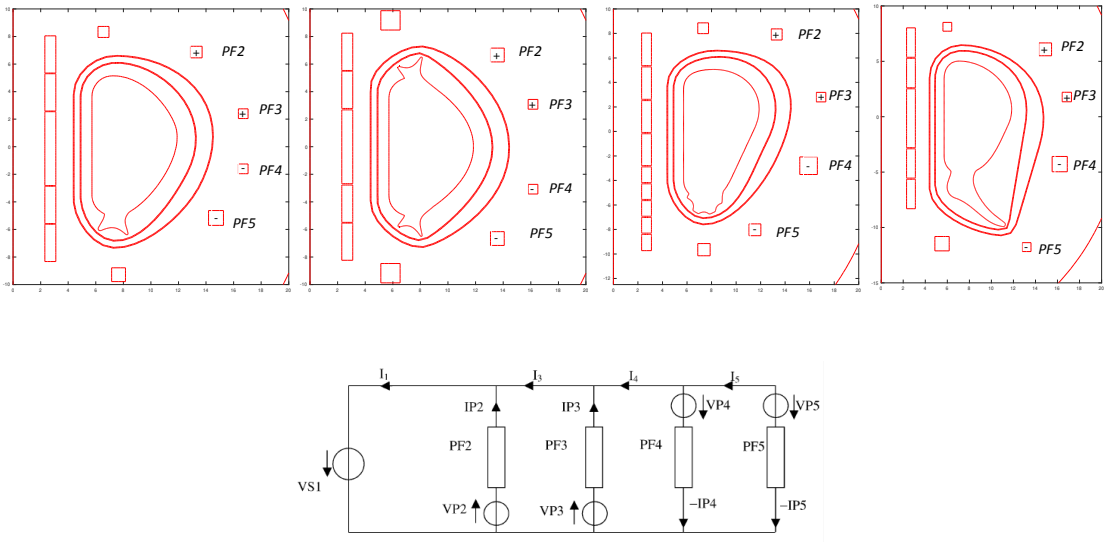

Fig. 4.28 – Imbalance circuit considered for vertical stabilization

The assessment of the VS performance in terms of passive stability parameters (growth rate γ and stability margin m_s) is reported in Table 4.8 while the maximum power request for the vertical stabilization system for VDE and the disturbances listed above are reported in Table 4.9, 4.10 and 4.11. The VDE analysis has been performed using the linearized code CREATE-L [12] while the analysis of the ELMs and MDs is performed by means nonlinear simulations using CREATE-NL code [37] neglecting the effect of the ports.

The DN configuration is the most demanding configuration in terms of growth rate and power request in case of VDE due to the high distance between the plasma and the passive conductive structures. However, the power requests in all the VDE cases are very far from the limit of 500MW.

Table. 4.8 – Passive vertical stability parameters

Configuration	γ [s^{-1}]	m_s
SN @ SOF $k_{95\%}$=1.55	1.69	1.22
DN @ SOF $k_{95\%}$=1.56	4.97	0.57
SX @ SOF $k_{95\%}$=1.57	2.17	1.05
SF @ SOF $k_{95\%}$=1.54	1.53	1.31

Table. 4.9 – Active VS analysis in case of a 5cm VDE

Configuration	Zmax [cm]	Pow [MW]
SN @ SOF $k_{95\%}$=1.55	6.06	8.78
DN @ SOF $k_{95\%}$=1.56	6.51	55.46
SX @ SOF $k_{95\%}$=1.57	6.38	50.71
SF @ SOF $k_{95\%}$=1.54	6.18	14.06

Table. 4.10 – Active VS analysis in case of ELM

Configuration	Z0 [cm]	Zmax [cm]	Pow [MW]
SN @SOF $k_{95\%}$=1.55	5.46	7.59	75.43
SX @ SOF $k_{95\%}$=1.57	11.38	15.37	>1000
SF @ SOF $k_{95\%}$=1.54	16.92	Limiter plasma	

Table. 4.11 – Active VS analysis in case of a MD

Configuration	Z0 [cm]	Zmax [cm]	Pow [MW]
SN @SOF $k_{95\%}$=1.55	-9.61	-17.05	316.06
SX @ SOF $k_{95\%}$=1.57	-20.27	-62.65	>1000
SF @ SOF $k_{95\%}$=1.54	-43.77	Limiter plasma	

The ELM and MD analysis has been performed only for the SN, SX and SF because, neglecting the effect of the ports, the DN configurations is ideally balanced and no vertical movement is caused by the disturbances application.

The instantaneous vertical displacement Z0 of the ACs is significant in all the cases and only the SN power requests are below 500MW. In the SX case, the maximum instantaneous vertical displacement $|Z0| \cong 20$cm and we are able to recover the plasma vertical mode with very high power on the VS circuit, much higher than the limit of

500MW. In the SF case, the maximum instantaneous vertical displacement |Z0|≅40cm and the plasma reaches the wall in the divertor region, so it hasn't been possible to conclude the vertical analysis. It is important to recognize that possible strategies such as linearized simulation or a fictitious modification of the FW could be adopted to conclude the VS analysis for the SF, however the initial displacement of 40cm clearly indicate power request much higher than the limit of 500 MW.

4.3.3.2 Shape sensitivity analysis

The instantaneous shape variations of the ACs in case of MDs and ELMs have been evaluated using the CREATE-NL code and the results are illustrated in Fig. 4.29, 4.30 and 4.31 and Tables 4.12, 4.13 and 4.14. For SN and SX it is reported the vertical and radial movements of the plasma centroid and the movements of the inner and outer legs evaluated as Euclidean distance pre and after the application of the disturbs at the intersection between the leg and the divertor plate. The SF, instead of the movement of the leg, it is reported the distance between the active and not-active X-point after the application of the disturb (in the reference case the distance is within 20cm). The results in Tables 4.12 - 4.14 show a high sensitivity of all the configurations with respect to the set of disturbances. The sensitivity can be reduced working on the balancing of the configurations to take into account that, at the present stage, the distance between plasma centroid and the magnetic axis is 7cm for the SN, 10cm for the SX and 22cm for the SF.

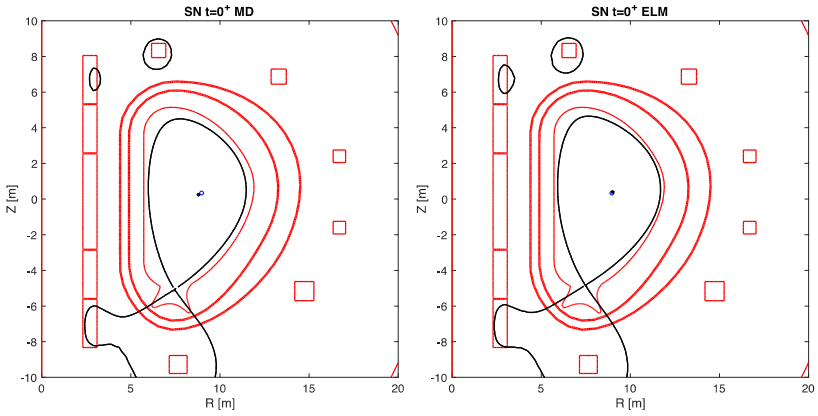

Fig. 4.29 – SN shape variation in case of ELM and MD

Table. 4.12 – SN shape instantaneous variation in case of ELM and MD

	ELM	MD
ΔZ_{pl} [cm]	5.5	9.6
ΔR_{pl} [cm]	5.0	17.8
$\Delta \text{leg}_{\text{in}}$ [cm]	7.9	12.3
$\Delta \text{leg}_{\text{out}}$ [cm]	4.8	8

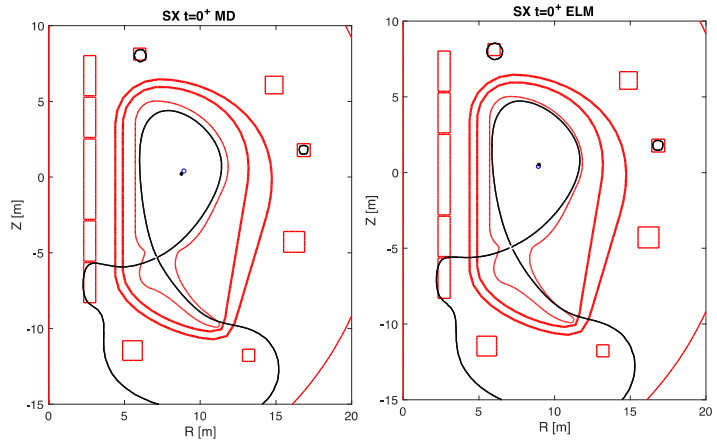

Fig. 4.30 – SX shape variation in case of ELM and MD

Table. 4.13 – SX shape instantaneous variation in case of ELM and MD

	ELM	MD
ΔZ_{pl} [cm]	11.4	20.3
ΔR_{pl} [cm]	4.6	17.1
$\Delta \text{leg}_{\text{in}}$ [cm]	14.0	14.0
$\Delta \text{leg}_{\text{out}}$ [cm]	6.4	6.4

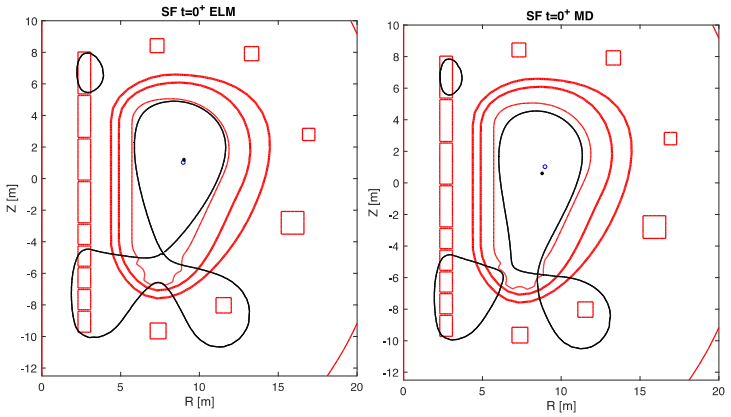

Fig. 4.31 – SF shape variation in case of ELM and MD

Table. 4.14 – SF shape instantaneous variation in case of ELM and MD

	ELM	MD
ΔZ_{pl} [cm]	16.9	43.8
ΔR_{pl} [cm]	4.7	18.5
Xpoints distance [cm]	124	191

4.4 DTT research activity

In this Section, the research activity for DTT device will be presented [68]. The main objective of the Divertor Tokamak Test (DTT) facility is to host experiments addressed to the solution of the power exhaust issues in view of DEMO [26]. This derives from the need to develop integrated and controllable exhaust solutions including plasma, PFCs, control diagnostics and actuators, using experiments, theory and modelling, to mitigate the risk that conventional divertor might not be suitable for DEMO. The DTT project has been proposed in 2015 by about one hundred scientists from several Italian institutions with the support of scientists from various international labs with the publication of the DTT facility proposal [27] and a special issue on Fusion Engineering Design [66]. In the last year the DTT Team has refined the project, also in the light of suggestions of EUROFusion, defining an up-down symmetric DTT device so as to allow for an additional, upper divertor and, thereby up-down symmetric configurations. The revision process necessitated a slight reduction of the major and minor radius (currently of $2.10m$ and $0.65m$, respectively) and plasma current (presently $5.5\ MA$) leaving the magnetic field unaltered ($6\ T$). Starting from a reference DTT scenarios in [67], conventional Single Null, Double Null and SnowFlake plasma scenarios for the symmetrized DTT device have been produced optimizing the plasma shape and the currents on the PF coils. Flat-top snapshots for Double Super-X (DSX) and Single Null with negative triangularity (SN-NT) have been also investigated in order to demonstrate the flexibility of the machine and its PF coil system to achieve different alternative divertor concepts. In Section 4.4.1 the geometry of DTT device will be proposed while in Section 4.4.2 the constraints to be met in order to design plasma scenarios will be presented. In Section 4.4.3 a description of the breakdown phase will be provided. Finally, in Section 4.4.4 a description of plasma scenarios for SN, DN, SF, DSX and SN-NT configurations will be proposed.

4.4.1 Machine configuration and geometry

The last version of the DTT device has been designed with a major radius $R_0 = 2.10m$ and an aspect ratio $AR \cong 3.2$. The DTT PF coils system, illustrated in Figure 4.30, is composed by:

	R [M]	Z [M]	DR [M]	DZ [M]	TURNS
'CS3U_H'	0.459	2.200	0.047	0.828	46
'CS3U_M'	0.534	2.200	0.103	0.828	92
'CS3U_L'	0.667	2.200	0.162	0.828	208
'CS2U_H'	0.459	1.320	0.047	0.828	46
'CS2U_M'	0.534	1.320	0.103	0.828	92
'CS2U_L'	0.667	1.320	0.162	0.828	208
'CS1U_H'	0.459	0.440	0.047	0.828	46
'CS1U_M'	0.534	0.440	0.103	0.828	92
'CS1U_L'	0.667	0.440	0.162	0.828	208
'CS1L_H'	0.459	-0.440	0.047	0.828	46
'CS1L_M'	0.534	-0.440	0.103	0.828	92
'CS1L_L'	0.667	-0.440	0.162	0.828	208
'CS2L_H'	0.459	-1.320	0.047	0.828	46
'CS2L_M'	0.534	-1.320	0.103	0.828	92
'CS2L_L'	0.667	-1.320	0.162	0.828	208
'CS3L_H'	0.459	-2.200	0.047	0.828	46
'CS3L_M'	0.534	-2.200	0.103	0.828	92
'CS3L_L'	0.667	-2.200	0.162	0.828	208
'PF1'	1.423	2.628	0.574	0.660	294
'PF2'	3.056	2.431	0.315	0.481	171
'PF3'	4.322	1.024	0.396	0.470	211
'PF4'	4.322	-1.024	0.396	0.470	211
'PF5'	3.056	-2.431	0.315	0.481	171
'PF6'	1.423	-2.628	0.574	0.660	294
'INVESSVSU'	2.988	0.553	0.134	0.134	4
'INVESSVSL'	2.988	-0.553	0.134	0.134	4
'INVESS1L'	1.397	-1.168	0.067	0.067	1
'INVESS2L'	1.499	-1.370	0.067	0.067	1
'INVESS3L'	1.734	-1.559	0.067	0.067	1
INVESS4L	2.193	-1.546	0.067	0.067	1

Table. 4.15 – PF coil system of DTT device

- 6 independent CS coils with a graded solution: *CS3U - CS2U - CS1U - CS1L - CS2L - CS3L*;
- 6 independent PF coils: *PF1 - PF2 - PF3 - PF4 - PF5 - PF6*;
- 4 independent divertor coils: *InVess1L - InVess2L - InVess3L - InVess4L*;
- 2 independent InVessel coils: *InVessVSU - InVessVSL*;

Each CS circuit is composed by the series of 3 coils at high, medium and low poloidal field. It allows to maximize the currents in the circuits up to 28 kA for the CS and 26.6 kA for the PF circuits. The details of the PF coils system are reported in Table 4.15. Two stainless steel vessel shells of 1.5 cm have been assumed with two toroidally discontinuous stabilizing plates of 3 cm placed between the first wall and the InVessel coils (*InVessVSU-InVessVSL*), as shown in Fig. 4.32.

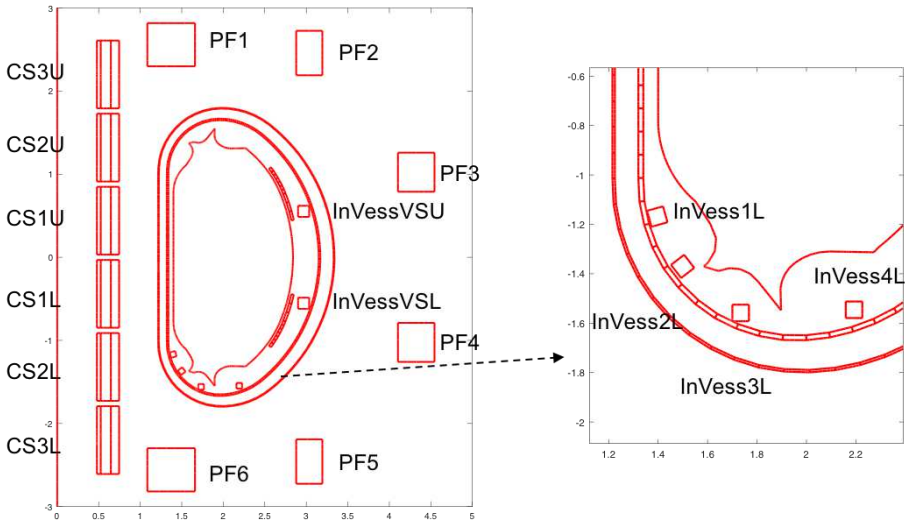

Fig. 4.32 – Poloidal section of the DTT device

4.4.2 Constraints

Hereafter the main specifications used for the design of the DTT plasma scenarios are summarized.

Magnetic field

The maximum magnetic field at the location of the CS coils shall not exceed $\sim 14\ T$ in the high field region, $\sim 12\ T$ in the medium field region and $\sim 8\ T$ in the low field region. The constraint related to the magnetic field on the PF is $\sim 6\ T$.

Vertical Forces

The force limits on the PF coils are:

- The maximum vertical force on the CS stack in DTT should not exceed $20MN$;
- The maximum separation force in the CS stack should not exceed $30MN$;
- Maximum vertical force on a single PF coil should not exceed $40MN$ at the low field PF coils (PF2-PF5) and it is $26MN$ for PF1 and PF6.

Plasma

- Minimum clearance of 30 mm between the plasma last closed surface and the first wall
- Maximum plasma current of 5.5 MA
- Plasma shape parameters similar to present EU DEMO: R_0/a≈3.2, $k_{95\%}$≈1.65-1.7
- Flux swing at flat top compatible with a pulse duration of about 100 s
- Ripple limited to 0.5%, yielding $R_0 + a$ <2.75 m
- Vertical stability margin m_s>0.3, thus m_s>>0.3 at high poloidal beta

4.4.3 Pre-magnetization and Breakdown

This section shows that the symmetric PF system is able to provide a flux swing of 32.4 Vs, with a pre-magnetization of 16.2 Vs inside the vessel shown in Fig. 4.33. The analysis is performed using a 2D equivalent models for 3D effects. Indeed, the effects of the ports are taken into account by removing 1/3 of the conductive elements in correspondence of each port; the presence of the stabilizing passive plates outboard connected to the vacuum vessel via sidewalls (see Figure 4.34) is modeled in terms of equivalent inductances and resistances, yielding a time constant of the passive structures of L/R=46.4 ms.

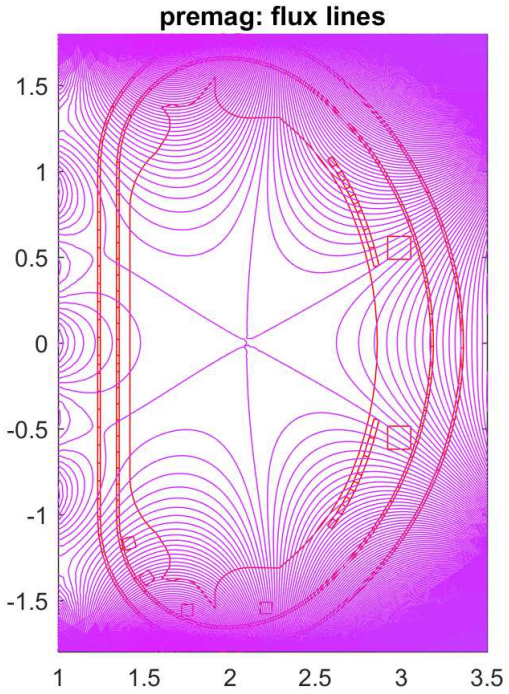

Fig. 4.33 – Pre-magnetization (16.2 Vs inside the vessel)

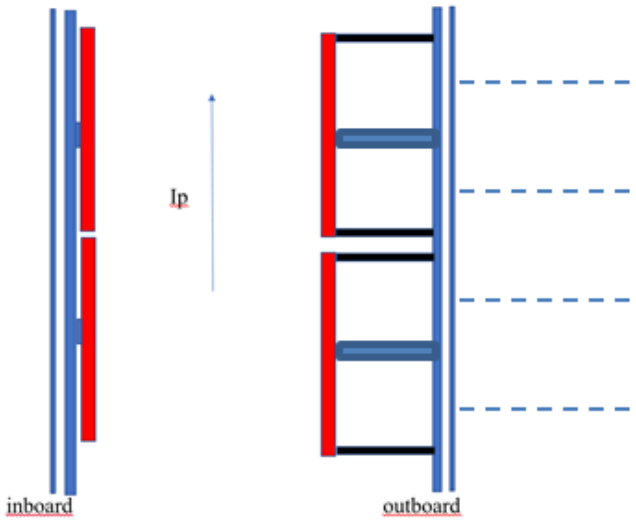

Fig. 4.34 – Horizontal view of the stabilizing passive plates outboard connected to VV via sidewalls

A dynamic compensation of the vertical magnetic field on the chamber geometrical center has been designed using the In-vessel circuit. The corresponding time behavior of the

electrical field and the vertical magnetic field is reported in Figure 4.35. The time delay of the flux response due to the passive structures is about $\tau_d = 40.4$ ms.

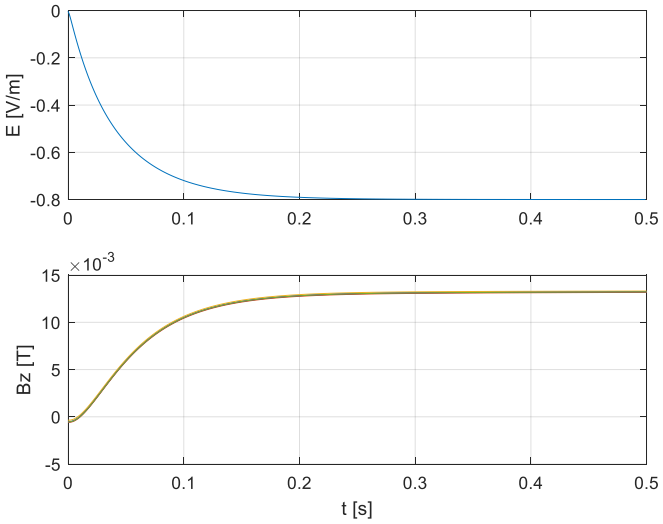

Fig. 4.35 - Time behavior of the electrical field and the vertical magnetic field in the chamber geometrical center in case of dynamical compensation

4.4.4 Plasma Scenarios

Single Null

The scenario has been designed to form a X-point configuration in H-mode with a plasma current $I_P = 5.5$MA with a discharge duration around 90s from the breakdown to the end of flat top and an X-point configuration sustained for around 70 s (much longer than the plasma resistive time) equals to a flat top flux-swing of around 8.1 Vs. Table 4.16 shows the time evolution of the PF coil currents guaranteeing the sequence of plasma shapes during the DTT reference Single Null scenario, obtained using the CREATE-NL code [37]. In Fig. 4.36 the sequence of plasma shapes during the scenario has been reported while in Tables 4.17,4.18 and 4.19 the main plasma parameters, the vertical forces and the magnetic fields of the SN scenarios are reported respectively.

After the breakdown, I_P rises up to 3.0 MA in $\Delta t = 15$ s; during this phase, the plasma evolves with a circular to elliptical shape, leaning on the inboard side of the first wall.

Between t = 15 s and t = 22 s the plasma current ramps up to 4.3 MA achieving the X-point configuration. In this scenario the plasma remains limited for about 15 s. Between t = 22 s and t = 27 s, the plasma current achieves its target value of 5.5 MA, while β_P remains very low. The boundary flux Ψ_{SOF} at start of flat top (t = 27 s) is calculated assuming an Ejima coefficient C_{EJIMA} = 0.35 and a breakdown flux Ψ_{BD} = 16.2Vs [57]. At t = 28 s, full additional heating is assumed, causing an increase of the internal kinetic energy on a time scale longer than the plasma energy confinement time. After t = 36 s, all plasma physical parameters are assumed to remain nearly constant up to the end of the current plateau at t = 90 s. At the end of flat top, the plasma is no longer heated and a controlled ramp-down phase similar to the JET tokamak follows, in which the plasma current decreases at the rate of ~100 kA/s (more than 400 kA/s if needed in emergency cases) while keeping a single null configuration at low beta, low elongation, and controlled density (no more than 50% of Greenwald limit) till about 200 kA.

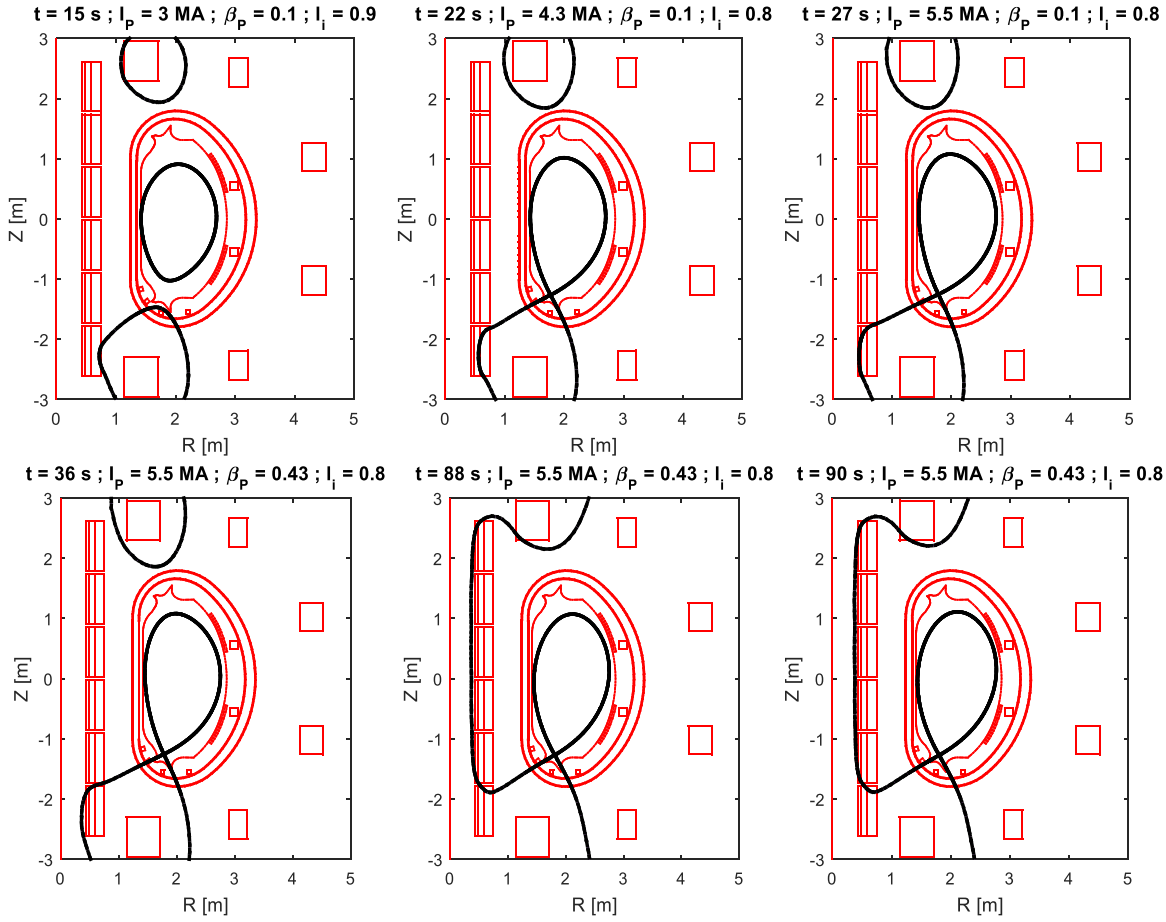

Fig. 4.36 – Snapshots of SN plasma scenario at t = 15 s, 22 s, 27 s, 36 s, 88 s and 90 s

Table. 4.16 – PF coil currents evolution of SN scenario

TIME	0	15	22	27	28	36	88	90
IPL [MA]		3,00	4,30	5,50	5,50	5,50	5,50	5,50
BETAPOL		0,10	0,10	0,10	0,10	0,43	0,43	0,43
LI		0,90	0,80	0,80	0,80	0,80	0,80	0,80
PSB [VS]		9,42	7,24	4,87	4,50	2,64	-5,13	-5,48
CS3U [KA]	28,00	-1,12	-3,50	-6,31	-6,57	-14,89	-28,00	-28,00
CS2U [KA]	28,00	4,98	1,08	-3,19	-3,81	-5,38	-28,00	-28,00
CS1U [KA]	28,00	8,85	-0,55	-9,83	-10,52	-12,96	-28,00	-28,00
CS1L [KA]	28,00	1,87	-9,36	-21,53	-22,17	-22,10	-28,00	-28,00
CS2L [KA]	28,00	7,23	1,77	-3,95	-4,52	-9,83	-27,98	-28,00
CS3L [KA]	28,00	14,41	16,48	17,99	16,91	16,36	-7,32	-7,80
PF1 [KA]	9,80	15,00	17,47	18,45	18,00	17,47	7,16	6,09
PF2 [KA]	0,43	-1,32	-4,92	-9,05	-8,92	-6,90	0,51	-0,22
PF3 [KA]	1,16	-4,64	-6,48	-8,30	-8,41	-10,50	-10,05	-9,77
PF4 [KA]	1,16	-6,01	-8,19	-9,15	-9,09	-10,33	-15,70	-15,05
PF5 [KA]	0,43	-7,89	-11,74	-16,16	-16,34	-14,77	-10,77	-11,07
PF6 [KA]	9,80	20,09	22,67	25,09	25,11	22,96	21,80	20,88

Table. 4.17 – Main plasma parameters time evolution of SN scenario

TIME	15	22	27	28	36	88	90
AXIS FLUX [VS]	15,13	14,75	14,65	14,27	12,46	4,68	4,36
RPL [M]	2,05	2,05	2,08	2,08	2,12	2,13	2,13
ZPL [M]	-0,02	-0,02	0,01	0,01	0,01	0,02	0,04
RAXIS - NODE [M]	2,09	2,11	2,13	2,13	2,17	2,17	2,17
ZAXIS - NODE [M]	-0,02	0,00	0,02	0,02	0,04	0,04	0,08
RBOUND - NODE [M]	1,42	1,78	1,80	1,80	1,78	1,80	1,80
ZBOUND - NODE [M]	0,00	-1,26	-1,24	-1,24	-1,26	-1,27	-1,27
R [M]	2,05	2,06	2,10	2,10	2,10	2,10	2,11
A [M]	0,63	0,63	0,65	0,65	0,65	0,65	0,67
BTOR_TOT AT MAG. AXIS [T]	6,29	6,35	6,38	6,38	6,22	6,23	6,20
BTOR0 AT MAJOR RADIUS [T]	6,19	6,22	6,31	6,31	6,03	6,03	6,01
BETAN	0,19	0,21	0,26	0,26	1,17	1,18	1,16
Q_95	3,54	3,12	2,50	2,50	2,54	2,47	2,57
ELONGATION (K)	1,53	1,79	1,79	1,79	1,80	1,80	1,79
K_95	1,49	1,67	1,67	1,67	1,67	1,67	1,66
TRIANGULARITY (DELTA)	0,13	0,28	0,34	0,34	0,33	0,21	0,23
DELTA_95	0,11	0,19	0,24	0,24	0,23	0,13	0,14
PERIMETER [M]	5,03	5,59	5,73	5,73	5,76	5,73	5,83
VOLUME [M^3]	23,89	26,93	28,69	28,69	28,79	28,68	29,99

Table. 4.18 – Time evolution of vertical forces and separation force on CS for SN scenario

TIME	15	22	27	28	36	88	90
FZCS3U [MN]	0,04	-1,19	-4,37	-4,78	-12,56	-59,30	-58,35
FZCS2U [MN]	-2,33	0,05	-1,63	-2,04	-1,01	-5,86	-5,15
FZCS1U [MN]	0,72	-0,30	-10,04	-10,76	-11,84	2,58	2,58
FZCS1L [MN]	0,05	2,26	10,49	10,92	7,35	4,72	4,41
FZCS2L [MN]	-6,96	-3,28	10,98	12,48	26,73	49,54	48,27
FZCS3L [MN]	0,06	-7,86	-17,69	-17,36	-21,43	18,35	19,39
FZP1 [MN]	4,67	1,43	2,97	3,45	8,80	10,92	9,22
FZP2 [MN]	0,10	1,06	2,80	2,86	3,22	0,35	0,14
FZP3 [MN]	1,92	3,09	3,18	3,26	6,00	13,72	12,39
FZP4 [MN]	0,29	0,18	0,25	0,21	2,05	5,08	4,30
FZP5 [MN]	0,91	3,14	6,05	6,26	7,26	10,14	10,06
FZP6 [MN]	14,57	13,08	9,69	8,38	3,97	22,84	22,23
FZ ON CS [MA]	-8,41	-10,31	-12,26	-11,54	-12,75	10,03	11,14
MAX SEPARATION FORCE FZUP [MN] ON CS	0,04	0,83	5,43	5,82	8,67	10,03	11,14
MAX SEPARATION FORCE FZDOWN [MN] ON CS	-8,45	-11,14	-17,69	-17,36	-21,43	10,03	11,14
MAX FZ IN P1-P6 [MA]	14,57	13,08	9,69	8,38	8,80	22,84	22,23

Table. 4.19 – Time evolution of magnetic fields for SN scenario

TIME	15	22	27	28	36	88	90
MAX BZ ON CS_HF [T]	7,81	8,34	8,64	8,23	7,78	12,85	12,90
MAX BZ ON CS_MF [T]	6,94	7,38	7,61	7,26	6,60	10,80	10,85
MAX BZ ON CS_LF [T]	5,37	5,75	5,97	5,74	5,50	6,55	6,58
BZ_P1 [T]	3,59	3,99	4,05	3,94	3,98	2,27	2,04
BZ_P2 [T]	0,52	1,19	1,92	1,90	1,62	0,57	0,47
BZ_P3 [T]	0,98	1,35	1,71	1,73	2,12	2,08	2,01
BZ_P4 [T]	1,22	1,65	1,86	1,85	2,09	3,03	2,91
BZ_P5 [T]	1,67	2,40	3,18	3,21	2,98	2,43	2,45
BZ_P6 [T]	4,40	4,73	5,01	4,99	4,46	4,46	4,27

Double Null

The up-down symmetrization of the DTT device has made it possible to obtain a flat top DN configuration with I_P = 5.5 MA and a flat top flux swing of 7.9 Vs. The reference DN scenario has been designed assuming the formation of both X-points at 22s with a plasma current of 4.3MA. The L-H transition occurs in the time interval [28 – 36] s and the duration of the flat top is ~ 55 s, similar to the SN scenario. In Fig. 4.37 the sequence

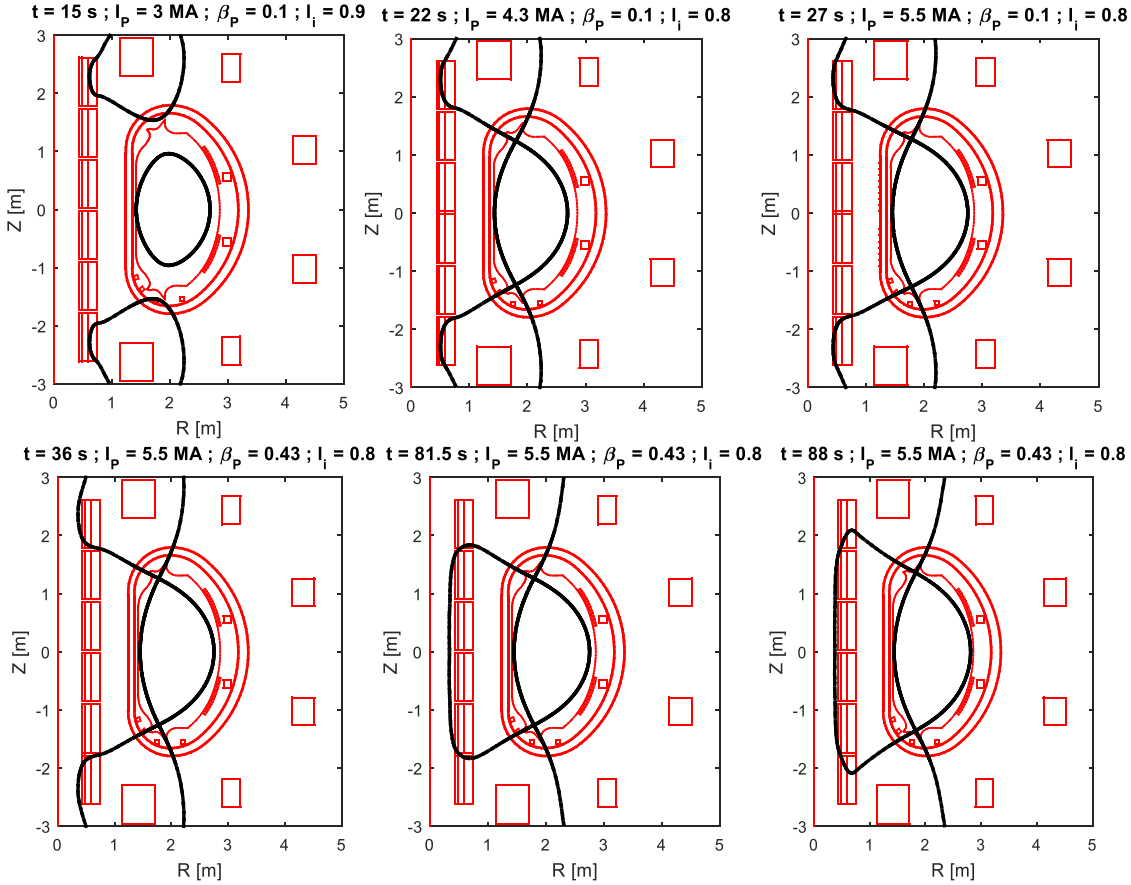

Fig. 4.37 – Snapshots of DN plasma scenario at t = 15 s, 22 s, 27 s, 36 s, 81.5 s and 88 s

Table. 4.20 – PF coil currents evolution of DN scenario

TIME	0	15	22	27	28	36	81.5	88
IPL [MA]		3,00	4,30	5,50	5,50	5,50	5,50	5,50
BETAPOL		0,10	0,10	0,10	0,10	0,43	0,43	0,43
LI		0,90	0,80	0,80	0,80	0,80	0,80	0,80
PSB [VS]		9,42	7,27	4,88	4,51	2,65	-4,20	-5,22
CS3U [KA]	28,00	20,07	21,28	20,20	19,98	16,19	-2,74	-12,60
CS2U [KA]	28,00	-3,01	-6,31	-10,20	-10,77	-15,25	-28,00	-28,00
CS1U [KA]	28,00	7,06	-4,19	-14,85	-15,55	-16,65	-28,00	-28,00
CS1L [KA]	28,00	7,06	-4,19	-14,85	-15,55	-16,65	-28,00	-28,00
CS2L [KA]	28,00	-3,01	-6,31	-10,20	-10,77	-15,25	-28,00	-28,00
CS3L [KA]	28,00	20,07	21,28	20,20	19,98	16,19	-2,74	-12,60
PF1 [KA]	9,80	20,67	26,60	26,60	26,27	26,60	26,42	20,29
PF2 [KA]	0,43	-8,21	-15,53	-18,86	-18,96	-18,97	-20,28	-13,71
PF3 [KA]	1,16	-4,63	-5,90	-7,32	-7,32	-8,56	-8,95	-9,97
PF4 [KA]	1,16	-4,63	-5,90	-7,32	-7,32	-8,56	-8,95	-9,97
PF5 [KA]	0,43	-8,21	-15,53	-18,86	-18,96	-18,97	-20,28	-13,71
PF6 [KA]	9,80	20,67	26,60	26,60	26,27	26,60	26,42	20,29

Table. 4.21 – Main parameters evolution of DN scenario

TIME	15	22	27	28	36	81.5	88
AXIS FLUX [VS]	15,14	14,76	14,65	14,28	12,47	5,63	4,71
RPL [M]	2,06	2,04	2,08	2,08	2,11	2,11	2,14
ZPL [M]	0,00	0,00	0,00	0,00	0,00	0,00	0,00
RAXIS - NODE [M]	2,11	2,09	2,13	2,13	2,17	2,17	2,19
ZAXIS - NODE [M]	0,00	0,00	0,00	0,00	0,00	0,00	0,00
RBOUND - NODE [M]	1,42	1,80	1,78	1,78	1,78	1,80	1,84
ZBOUND - NODE [M]	0,00	-1,24	-1,26	-1,26	-1,26	-1,27	-1,35
R [M]	2,06	2,06	2,10	2,10	2,10	2,10	2,12
A [M]	0,64	0,63	0,65	0,65	0,65	0,65	0,69
BTOR_TOT AT MAG. AXIS [T]	6,28	6,36	6,38	6,38	6,22	6,22	6,13
BTOR0 AT MAJOR RADIUS [T]	6,13	6,29	6,29	6,29	6,03	6,03	5,94
BETAN	0,19	0,21	0,26	0,26	1,16	1,15	1,09
Q_95	3,44	3,37	2,77	2,77	2,76	2,75	3,09
ELONGATION (K)	1,51	1,97	1,95	1,95	1,94	1,94	1,97
K_95	1,48	1,75	1,74	1,74	1,72	1,72	1,76
TRIANGULARITY (DELTA)	0,12	0,42	0,49	0,49	0,50	0,47	0,44
DELTA_95	0,10	0,27	0,32	0,32	0,31	0,31	0,28
PERIMETER [M]	4,99	5,83	6,02	6,02	6,00	6,00	6,38
VOLUME [M^3]	23,69	27,24	29,52	29,51	29,26	29,35	33,64

Table. 4.22 – Time evolution of vertical forces and separation force on CS for DN scenario

TIME	15	22	27	28	36	81.5	88
FZCS3U [MN]	12,24	22,33	27,55	27,92	27,62	-7,16	-30,99
FZCS2U [MN]	-3,07	-12,20	-26,13	-27,91	-37,52	-58,92	-39,14
FZCS1U [MN]	-3,43	-0,11	-6,55	-7,01	-4,37	-4,55	-2,60
FZCS1L [MN]	3,43	0,11	6,54	7,00	4,36	4,51	2,56
FZCS2L [MN]	3,08	12,21	26,15	27,94	37,55	59,01	39,22
FZCS3L [MN]	-12,24	-22,32	-27,53	-27,90	-27,59	7,15	30,94
FZP1 [MN]	14,35	14,71	9,46	8,58	2,12	23,89	23,30
FZP2 [MN]	0,74	3,37	5,71	5,88	8,12	13,18	9,05
FZP3 [MN]	0,13	0,51	0,81	0,82	0,02	0,59	3,21
FZP4 [MN]	0,13	0,51	0,82	0,82	0,01	0,58	3,20
FZP5 [MN]	0,75	3,41	5,76	5,94	8,18	13,24	9,08
FZP6 [MN]	14,36	14,74	9,49	8,62	2,16	23,85	23,28
FZ ON CS [MA]	0,01	0,02	0,04	0,04	0,06	0,04	-0,01
MAX SEPARATION FORCE FZUP [MN] ON CS	12,25	22,34	27,57	27,94	27,65	0,04	-0,01
MAX SEPARATION FORCE FZDOWN [MN] ON CS	-12,24	-22,32	-27,53	-27,90	-27,59	0,04	-0,01
MAX FZ IN P1-P6 [MA]	14,36	14,74	9,49	8,62	8,18	23,89	23,30

Table. 4.23 – Time evolution of magnetic fields for DN scenario

TIME	15	22	27	28	36	88	90
MAX BZ ON CS_HF [T]	9,45	10,11	9,33	9,17	7,66	12,29	12,49
MAX BZ ON CS_MF [T]	8,29	8,90	8,19	8,05	6,79	10,35	10,54
MAX BZ ON CS_LF [T]	6,32	6,92	6,46	6,45	6,22	6,18	6,23
BZ_P1 [T]	4,47	5,46	5,25	5,16	5,14	5,20	4,23
BZ_P2 [T]	1,71	3,01	3,59	3,61	3,65	3,85	2,73
BZ_P3 [T]	0,97	1,23	1,52	1,52	1,76	1,81	1,99
BZ_P4 [T]	0,97	1,24	1,53	1,52	1,76	1,81	2,00
BZ_P5 [T]	1,70	3,00	3,59	3,60	3,64	3,84	2,73
BZ_P6 [T]	4,48	5,48	5,26	5,17	5,15	5,22	4,27

of plasma shapes during the scenario has been reported while in Tables 4.20 - 4.23 the PF currents, the main plasma parameters, the vertical forces and the magnetic fields of the DN scenarios are reported respectively.

Snowflake

The DTT geometry and PF coils system have made it possible to obtain a flat top SF configuration at 4.5 MA with a flat top flux swing of ~ 8.5 Vs and a flat top duration around of ~ 45 s, due to currents and vertical forces limitations. The reference SF scenario coincide with the SN case up to 22 s. Then, a single null shape is maintained for the ramp up and the L-H transition while creating a lower secondary X-point in the vicinity of the vessel shells. At 34 s, after the L-H transition, a migration towards a SF is imposed in a time interval of 3 s. The flat top configuration is a SF minus with a distance between the null points within 30 cm and a poloidal magnetic flux difference within 15 mVs. However, with the use of the internal coils is possible to locally modify the poloidal magnetic field in order to define ideal SF, SF plus and X-divertor configurations within the limits of the accuracy of the diagnostic system [67]. In Figure 4.38 the SF scenario snapshots are illustrated while while in Tables 4.24,4.25, 4.26 and 4.27 the PF currents, the main plasma parameters, the vertical forces and the magnetic fields of the SF scenarios are reported respectively. It is worth to notice that the SF^+ configurations illustrated in Figure 4.39, derived with slight PF current variations from the SF^- scenario, can also be

regarded as Super-X configurations provided the divertor plates are placed at a larger major radius R_t.

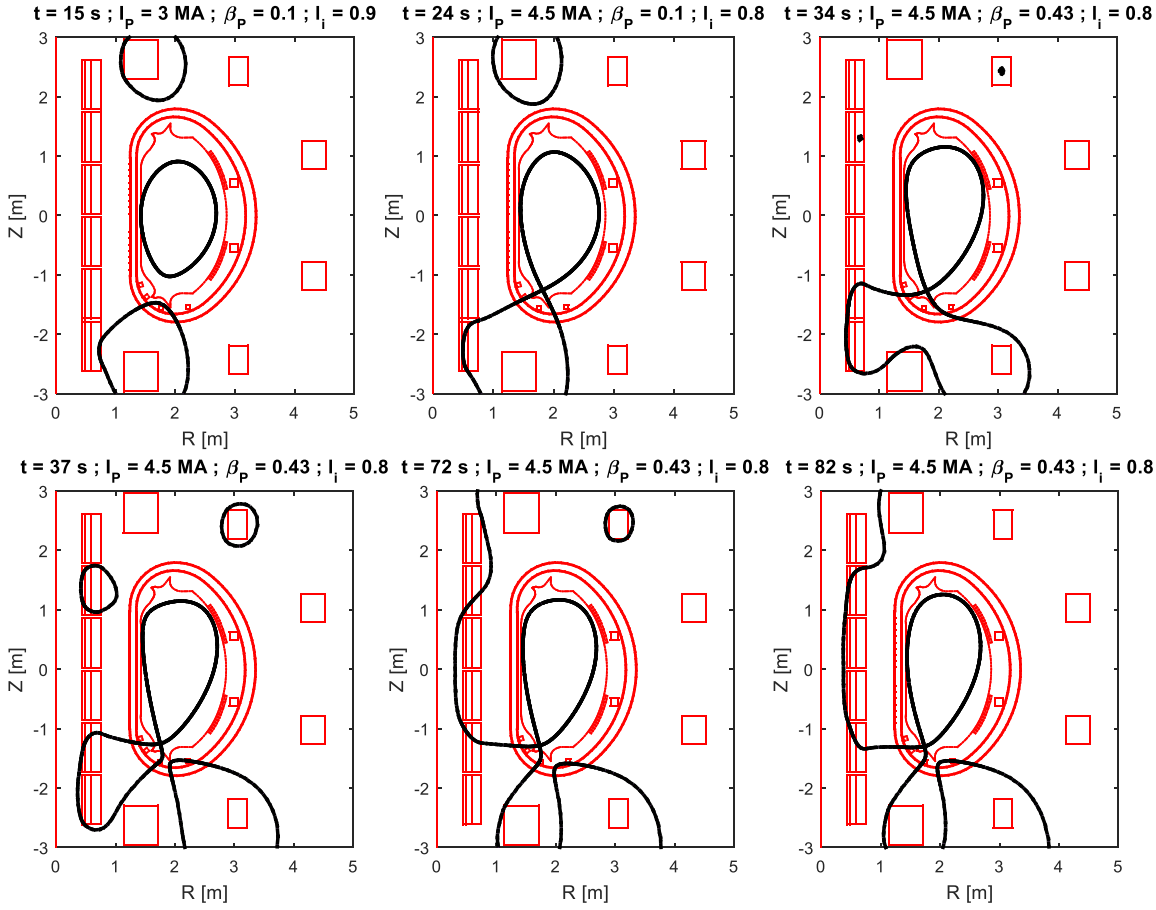

Fig. 4.38 – Snapshots of SF plasma scenario at t = 15 s, 24 s, 34 s, 37 s, 72 s and 82 s

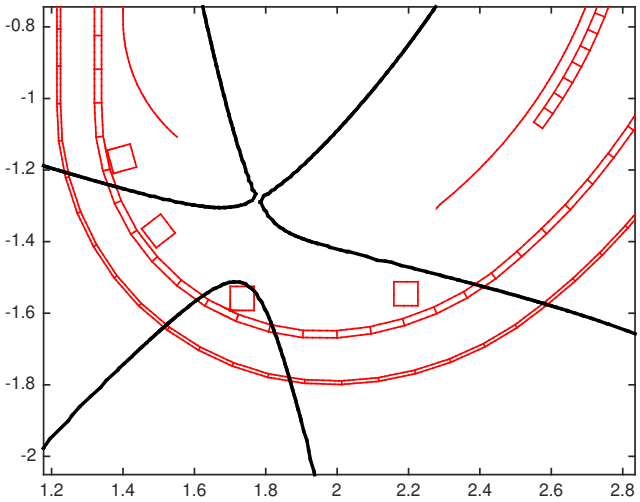

Fig. 4.39 – Snowflake plus configuration at 4.5 MA

Table. 4.24 – PF coil currents evolution of SF scenario

TIME	0	15	22	24	34	37	72	82
IPL [MA]		3,00	4,30	4,50	4,50	4,50	4,50	4,50
BETAPOL		0,10	0,10	0,10	0,43	0,43	0,43	0,43
LI		0,90	0,80	0,80	0,80	0,80	0,80	0,80
PSB [VS]		9,42	7,27	6,85	4,22	3,51	-3,18	-5,05
CS3U [KA]	28,00	-1,12	-3,62	-4,28	-4,41	-0,59	9,62	14,08
CS2U [KA]	28,00	4,98	0,83	-0,38	15,11	25,90	-0,70	-20,25
CS1U [KA]	28,00	8,85	1,05	-0,82	-9,07	-18,94	-28,00	-28,00
CS1L [KA]	28,00	1,87	-10,14	-12,28	-22,75	-20,97	-28,00	-28,00
CS2L [KA]	28,00	7,23	-1,21	-2,50	15,34	15,81	-3,85	-11,28
CS3L [KA]	28,00	14,41	21,11	21,56	19,03	26,68	24,83	28,00
PF1 [KA]	9,80	15,00	17,18	17,06	-11,81	-22,79	-22,79	-13,76
PF2 [KA]	0,43	-1,32	-4,85	-5,60	6,22	11,15	8,05	3,55
PF3 [KA]	1,16	-4,64	-6,76	-7,06	-4,14	-4,08	-4,63	-4,86
PF4 [KA]	1,16	-6,01	-7,94	-7,74	-22,32	-26,60	-26,60	-26,60
PF5 [KA]	0,43	-7,89	-11,59	-12,00	16,38	25,36	23,69	24,60
PF6 [KA]	9,80	20,09	22,28	22,68	-2,17	-11,12	-15,15	-17,89

Table. 4.25 – Main plasma parameters time evolution of SF scenario

TIME	15	22	24	34	37	72	82
AXIS FLUX [VS]	15,13	14,79	14,85	12,25	11,46	4,68	2,78
RPL [M]	2,05	2,05	2,09	2,12	2,10	2,08	2,08
ZPL [M]	-0,02	-0,03	0,01	0,17	0,20	0,18	0,21
RAXIS - NODE [M]	2,09	2,11	2,15	2,17	2,14	2,12	2,12
ZAXIS - NODE [M]	-0,02	0,00	0,02	0,22	0,25	0,24	0,24
RBOUND - NODE [M]	1,42	1,80	1,82	1,80	1,75	1,72	1,73
ZBOUND - NODE [M]	0,00	-1,27	-1,26	-1,27	-1,25	-1,29	-1,29
R [M]	2,05	2,07	2,10	2,10	2,08	2,06	2,06
A [M]	0,63	0,64	0,65	0,65	0,63	0,62	0,62
BTOR_TOT AT MAG. AXIS [T]	6,29	6,34	6,25	6,15	6,21	6,25	6,26
BTOR0 AT MAJOR RADIUS [T]	6,19	6,22	6,12	5,97	6,03	6,09	6,08
BETAN	0,19	0,21	0,22	0,94	0,94	0,91	0,88
Q_95	3,54	3,05	3,00	3,34	3,35	3,51	3,66
ELONGATION (K)	1,53	1,78	1,78	1,86	1,91	1,98	2,07
K_95	1,49	1,66	1,66	1,69	1,72	1,78	1,85
TRIANGULARITY (DELTA)	0,13	0,27	0,28	0,23	0,24	0,28	0,27
DELTA_95	0,11	0,20	0,21	0,13	0,12	0,14	0,14
PERIMETER [M]	5,03	5,57	5,72	5,97	5,93	5,99	6,11
VOLUME [M^3]	23,89	26,76	28,74	29,64	28,08	28,22	29,05

Table. 4.26 – Time evolution of vertical forces and separation force on CS for SF scenario

TIME	15	22	24	34	37	72	82
FZCS3U [MN]	0,04	-1,22	-1,79	5,60	1,28	-4,14	14,53
FZCS2U [MN]	-2,33	-0,05	-0,01	0,22	16,19	-1,33	-48,00
FZCS1U [MN]	0,72	0,60	-0,53	-18,34	-48,16	-43,59	-13,97
FZCS1L [MN]	0,05	-0,05	0,50	32,80	42,33	42,10	32,78
FZCS2L [MN]	-6,96	2,63	5,89	-38,12	-43,43	11,89	36,71
FZCS3L [MN]	0,06	-13,77	-16,45	16,73	30,44	-1,15	-12,33
FZP1 [MN]	4,67	1,35	0,62	4,53	15,41	4,78	1,67
FZP2 [MN]	0,10	1,07	1,15	0,12	0,60	1,60	1,21
FZP3 [MN]	1,92	3,01	2,64	6,85	8,53	9,68	9,66
FZP4 [MN]	0,29	0,12	0,13	18,77	31,48	33,16	35,87
FZP5 [MN]	0,91	3,01	3,13	13,05	24,43	27,01	29,30
FZP6 [MN]	14,57	14,33	13,73	1,74	11,28	6,00	5,32
FZ ON CS [MA]	-8,41	-11,85	-12,38	-1,12	-1,34	3,79	9,72
MAX SEPARATION FORCE FZUP [MN] ON CS	0,04	1,92	4,06	20,28	17,47	4,93	22,06
MAX SEPARATION FORCE FZDOWN [MN] ON CS	-8,45	-13,77	-16,45	-21,39	-18,81	-1,15	-12,33
MAX FZ IN P1-P6 [MA]	14,57	14,33	13,73	18,77	31,48	33,16	35,87

Table. 4.27 – Time evolution of magnetic fields for SF scenario

TIME	15	22	24	34	37	72	82
MAX BZ ON CS_HF [T]	7,81	9,78	9,89	7,43	9,31	11,25	12,04
MAX BZ ON CS_MF [T]	6,94	8,56	8,65	6,30	7,73	9,45	10,16
MAX BZ ON CS_LF [T]	5,37	6,53	6,61	6,56	7,29	6,18	6,80
BZ_P1 [T]	3,59	3,92	3,88	2,48	4,97	5,50	3,71
BZ_P2 [T]	0,52	1,18	1,30	0,93	1,75	1,21	0,71
BZ_P3 [T]	0,98	1,40	1,46	1,10	1,16	1,24	1,26
BZ_P4 [T]	1,22	1,61	1,58	4,24	5,04	5,02	5,02
BZ_P5 [T]	1,67	2,37	2,44	2,75	4,02	3,83	3,97
BZ_P6 [T]	4,40	4,64	4,69	0,92	2,87	3,89	4,62

Under these premises and in agreement with the space available in the divertor region, this DTT up-down symmetric machine can achieve a Super-X plasma scenario at 4.5 MA with a flat top flux swing similar to the SF case, a maximum toroidal flux expansion $R_t/R_x \approx 1.35$ and an outboard leg length $leg_{out} \approx 0.7$ m. The design of proper divertors for the SF configuration is an ongoing activity.

Additional alternative configurations

The symmetrized DTT geometry allows the design of additional alternative configurations such as DSX and SN-NT, as illustrated in Fig. 4.40. In Tables 4.28, 4.29, 4.30 and 4.31 the main plasma parameters, the vertical forces and the magnetic fields of DSX and SN-NT configurations at SOF and EOF are reported respectively. The SN-NT configuration at flat top can be achieved with a plasma current of 5.5 MA, a flat top flux swing of about 9.0 Vs and a lower triangularity of -0.26.

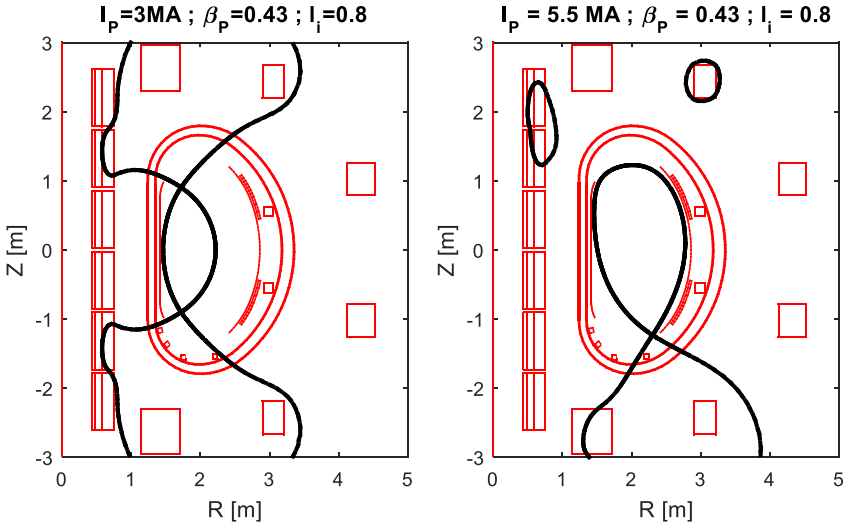

Fig. 4.40 – DSX at 3 MA and SN-NT at 5.5 MA

Table. 4.28 – PF coil currents of DSX and SN-NT configurations at SOF and EOF

	DSX		SN-NT	
TIME	**SOF**	**EOF**	**SOF**	**EOF**
IPL [MA]	3,00	3,00	5,50	5,50
BETAPOL	0,43	0,43	0,43	0,43
LI	0,80	0,80	0,80	0,80
PSB [VS]	10,27	-3,65	5,41	-3,71
CS3U [KA]	27,08	-12,17	19,32	13,08
CS2U [KA]	24,85	1,80	13,71	-4,49
CS1U [KA]	-4,00	-28,00	-12,60	-28,00
CS1L [KA]	-4,00	-28,00	-12,20	-28,00
CS2L [KA]	24,85	1,80	-9,81	-28,00
CS3L [KA]	27,08	-12,17	-21,52	-28,00
PF1 [KA]	9,18	10,41	-13,66	-20,90
PF2 [KA]	17,87	12,55	10,21	9,59
PF3 [KA]	-18,50	-18,65	-13,86	-14,45
PF4 [KA]	-18,50	-18,65	-19,24	-19,69
PF5 [KA]	17,87	12,55	23,17	22,00
PF6 [KA]	9,18	10,41	7,49	1,11

Table. 4.29 – Main plasma parameters of DSX and SN-NT configurations at SOF and EOF

	DSX		SN-NT	
TIME	**SOF**	**EOF**	**SOF**	**EOF**
AXIS FLUX [VS]	14,88	0,94	15,14	6,01
RPL [M]	1,84	1,84	2,14	2,14
ZPL [M]	0,00	0,00	0,14	0,14
RAXIS - NODE [M]	1,86	1,86	2,18	2,18
ZAXIS - NODE [M]	0,00	0,00	0,15	0,15
RBOUND - NODE [M]	1,71	1,71	2,29	2,29
ZBOUND - NODE [M]	-0,93	-0,93	-1,23	-1,23
R [M]	1,84	1,83	2,09	2,09
A [M]	0,39	0,39	0,66	0,66
BTOR_TOT AT MAG. AXIS [T]	6,93	6,96	6,18	6,18
BTOR0 AT MAJOR RADIUS [T]	6,79	6,82	5,97	5,97
BETAN	0,75	0,75	1,11	1,11
Q_95	3,03	3,01	2,66	2,66
ELONGATION (K)	2,38	2,38	1,85	1,85
K_95	2,07	2,06	1,73	1,73
TRIANGULARITY (DELTA)	0,33	0,31	-0,06	-0,06
DELTA_95	0,19	0,19	-0,02	-0,03
PERIMETER [M]	4,15	4,14	6,00	6,00
VOLUME [M^3]	11,35	11,20	31,33	31,31

Table. 4.30 – Vertical forces and separation force on CS for DSX and SN-NT configurations at SOF and EOF

	DSX		SN-NT	
TIME	**SOF**	**EOF**	**SOF**	**EOF**
FZCS3U [MN]	-34,03	-5,34	-23,86	-2,24
FZCS2U [MN]	49,60	2,38	21,02	-9,34
FZCS1U [MN]	-6,74	-47,31	-20,24	-42,61
FZCS1L [MN]	6,73	47,32	-1,70	-6,79
FZCS2L [MN]	-49,63	-2,39	-4,14	4,27
FZCS3L [MN]	33,92	5,34	18,77	54,85
FZP1 [MN]	12,87	6,87	14,42	4,14
FZP2 [MN]	14,74	15,69	2,80	5,13
FZP3 [MN]	39,52	39,82	18,87	21,14
FZP4 [MN]	39,34	39,63	36,78	39,39
FZP5 [MN]	14,68	15,66	19,06	23,82
FZP6 [MN]	12,87	6,89	5,87	1,83
FZ ON CS [MA]	-0,15	0,01	-10,15	-1,87
MAX SEPARATION FORCE FZUP [MN] ON CS	15,56	0,01	-2,84	-1,87
MAX SEPARATION FORCE FZDOWN [MN] ON CS	-15,71	0,01	-10,15	-1,87
MAX FZ IN P1-P6 [MA]	39,52	39,82	36,78	39,39

Table. 4.31 – Magnetic fields for DSX and SN-NT configurations at SOF and EOF

	DSX		SN-NT	
TIME	**SOF**	**EOF**	**SOF**	**EOF**
MAX BZ ON CS_HF [T]	12,62	11,41	6,91	12,75
MAX BZ ON CS_MF [T]	10,86	9,46	5,60	10,75
MAX BZ ON CS_LF [T]	7,58	6,53	4,72	6,58
BZ_P1 [T]	3,01	2,93	3,90	5,87
BZ_P2 [T]	3,01	2,41	1,70	1,63
BZ_P3 [T]	3,75	3,73	2,86	2,95
BZ_P4 [T]	3,78	3,76	3,89	3,95
BZ_P5 [T]	3,03	2,41	3,70	3,60
BZ_P6 [T]	3,02	2,91	3,10	1,68

The DSX configuration can only be achieved with a maximum plasma current of 3 MA and a flat top flux swing of about 14 Vs. The need of having reasonably large values of the toroidal flux expansion $R_t/R_x \approx 1.36$ and the outboard leg length ($leg_{out} \approx 0.90$ m), forces the plasma to have a high elongation and a reduced value of the minor radius. Such a plasma could not be stabilized vertically with the reference geometry of the passive structures. For this reason, we have envisaged the possibility of having a first wall closer to the plasma.

Chapter 5: Conclusions and future works

"Study hard what interests you the most in the most undisciplined, irreverent and original manner possible"

Richard Feynmann, Nobel laureate in physics in 1965

In this chapter, the conclusion of research activity shown in the previous chapter will be drawn.

Concerning EAST activity, reliable plasma-circuits models of the device have been produced as shown in Section 4.2 where the comparison between experimental data and open loop simulations has been presented. The good matching between the results of the simulations and measured signals prove the goodness of the models developed. Furthermore, the models produced have been employed to design an ITER-like vertical stability controller [69] and a MIMO shape controller [70] successfully adopted during EAST experimental campaigns. The future work on EAST foresee the design of new controllers to regulate the flux expansion near the divertor targets (a preliminary study can be found in [72]) and to control the distance of the two null points in Quasi-Snowflake discharges [71] while, from the modelling point of view, additional efforts will be spent to improve the performance of dynamical models performing an optimization of the passive conducting structures.

The research activities for DEMO tokamak have been carried out under the WP-ADC and WP-PMI work programs. An optimization procedure for the optimization of PF coil system has been presented showing its effectiveness for the DEMO SN baseline. The problem of the design of alternative divertor configurations has also been tackled showing the possible benefits and drawbacks of each configuration. According to the results presented in Section 4.3, alternative configurations represent a valid alternative to standard SN configurations since the modified magnetic topology allows to improve power exhaust performances. On the other hand, the preliminary vertical stability and shape sensitivity analyses of the above configurations have been performed showing critical results, in particular for the SF configuration. Additional engineering issues need to be considered in order to determine the engineering feasibility of the ADCs for DEMO.

This includes the analysis of the port location and remote maintenance (RM); structural analysis of the TF coils; definition of the in-vessel components compatible with the Tritium Breeding (TB); thermal load analysis on the PFCs (first wall and divertor); shape controllability of the configurations.

Concerning DTT research activity, the present analysis has shown the DTT capability to accommodate different types of alternative configurations proving a good flexibility of the machine design. A preliminary vertical stability analysis of standard and alternative configurations has been performed proving good stability properties of the machine due to the presence of the stabilizing plates. Future work will be dedicated to a deeper vertical stability analysis of the configurations and to the design of both vertical stability and plasma shape, current and positions controllers. Additional studies on the neutronics, the additional heating systems and the diagnostics could probably lead to a slight modification of machine geometry and PF coil system presented on this thesis.

References

[1] http://www.eia.gov/todayinenergy/detail.php?id=26212

[2] Bonolis Luisa – "Storia della ricerca sulla Fusione Termonucleare Controllata mediante confinamento magnetico";

[3] Bromberg Joan Lisa – "Fusion: Science, Politics, and the Invention of a New Energy Source", MIT Press, 1982;

[4] Wesson J., "Tokamaks – third edition", Clarendon Press-Oxford 2004, ISBN 0 19 8509227

[5] Lawson J. D., "Some criteria for a power producing thermonuclear reactor", Proc. Phys. Soc., 1967;

[6] Freidberg J. P., "Ideal MHD", Cambridge University Press, 2014;

[7] Freidberg J. P., "Plasma physics and fusion energy", Cambridge University Press, 2008;

[8] Albanese R., "Electromagnetic modelling of fusion devices", Lectures of "Advanced Engineering course", Padua 2017;

[9] Goedbloed J.P, Keppens R. and Poedts S., "Advanced magnetohydrodynamics: with applications to laboratory and astrophysical plasmas", Cambridge University Press, 2010;

[10] Albanese R., et al., "Plasma response models for current, shape and position control in JET", Fusion Eng. Des. 66–68 (2003) 715–718;

[11] Albanese R., Blum J., Barbieri O., "On the solution of the magnetic flux equation in an infinite domain", in: EPS. 8th Europhysics Conference on Computing in Plasma Physics, 1986;

[12] Albanese R., Villone F., "The linearized CREATE-L plasma response model for the control of current, position and shape in Tokamaks", Nucl. Fus., Vol. 38, Nr. 5, 1998, pp. 723;

[13] Igochine V., "Magnetohydrodynamics and Operational limits", Springer Berlin Heidelberg, 2015;

[14] Zohm H., "Tokamak Scenarios", Lectures of "Advanced Physics course", Garching 2016;

[15] Zanca P., et all, “A unified model of density limit in fusion plasma”, Nucl. Fus., 57(5):063008, 2013;

[16] Bolzonella T., “Introduction to Heating and Current Drive in fusion devices”, Lectures of “Advanced Engineering Course”, Padova 2017;

[17] Stix T., “Heating of toroidal plasma by neutral injection”, Plasma Phys., Vol. 14, 1972;

[18] Granucci G., “ECRH in fusion devices”, Lectures of “Advanced Engineering Course”, Padova 2017;

[19] Mirizzi F., “Ion cyclotron resonance heating systems”, Lectures of “Advanced Engineering Course”, Padova 2017;

[20] Peruzzo S., “Introduction to plasma diagnostics – Magnetic diagnostics on existing devices”, Lectures of “Advanced Engineering Course”, Padova 2017;

[21] Hutchinson I. H., “Principles of plasma diagnostics”, Cambridge University Press, 2001;

[22] Q.P. Yuan et al, “Plasma current, position and shape feedback control on EAST”, Nucl. Fus., Vol. 53, Nr.4, 2013;

[23] Weiyue W., Songtao W., Jie Y., Daming G., Peide W., “Assembly of Superconducting Tokamak EAST”, Journal of the Korean Physical Society, vol.49, 2006

[24] S.L. Chen et al, “3D passive stabilization of n = 0 MHD modes in EAST Tokamak”, Scientific Reports, 32440 (2016);

[25] http://english.ipp.cas.cn/rh/east/;

[26] EFDA, “Fusion Electricity - A roadmap to the realization of fusion energy”, https://www.euro-fusion.org/fileadmin/user_upload/Archive/wp-content/uploads/2013/01/JG12.356-web.pdf

[27] “DTT – Divertor Testing Tokamak Project Proposal”, http://fsn-fusphy.frascati.enea.it/DTT/downloads/Report/DTT_ProjectProposal_July2015.pdf

[28] D. Campbell, " ITER Research Needs", EUROFusion ITER Physics AWP-2016 Preparation Meeting, Garching, 6-8 July 2015;

[29] P. Batistoni, S. Clement Lorenzo, K. Kurzydlowski, D. Maisonnier, G. Marbach, M. Noe, J. Paméla, D. Stork, J. Sanchez, M.Q. Tran, H. Zohm ,”Report of the AHG on DEMO activities” CCE-FU 49/6.7;

[30] Kotschenreuther M., et al., “Magnetic geometry and physics of advanced divertors: The X-divertor and the snowflake”, Physics of Plasmas 20, 102507 (2013);

[31] Guo Y., Xiao B. J., Liu L., Yang F., Wang Y., Qiu Q., “A divertor plasma configuration design method for tokamaks”, Chinese Physics B, 2016, 25(11): 115201;

[32] D.D. Ryutov, “Geometrical properties of a snowflake divertor”, Physics of Plasmas 14 (2007) 064502.

[33] G. Calabrò et al., “Divertor configuration with two nearby poloidal field nulls: modelling and experiments for EAST and JET tokamaks”, 22th International Conference on Plasma Surface Interactions in Controlled Fusion Devices, Rome, May 30 – June 03, 2016;

[34] V. A. Soukhanovskii et al., “Snowflake Divertor as Plasma-Material interface for Future High-Density Fusion Devices”, 24th IAEA FEC, October 8-13, San Diego, California, USA, 2012;

[35] Y. Shimomura et al., “Characteristics of the divertor plasma in neutral-beam-heated ASDEX discharges”, Nuclear Fusion 23 (1983) 869;

[36] P. M. Valanju et al., “Super-X divertors and high-power density fusion devices”, Physics of Plasmas 16 (2009) 056110;

[37] Albanese R., Ambrosino R., Mattei M. “CREATE-NL+: A robust control-oriented free boundary dynamic plasma equilibrium solver”, Fus. Eng. Des, Vol. 96-97, 2015, pp. 664-667;

[38] A. Castaldo, A. Mele, R. Albanese, R. Ambrosino, G. De Tommasi, Z.P. Luo, B.J. Xiao, Q.P. Yuan, "Simulation suite for plasma magnetic control at EAST tokamak", Fusion Engineering and Design 133 (2018), 19-31;

[39] G. Manduchi, et al., “MDSplus evolution continues”, Fus. Eng. Des., 87 (2012) 2095–2099;

[40] L. Lao, H. S. John, R. Stambaugh, A. Kellman, W. Pfeiffer, “Reconstruction of current profile parameters and plasma shapes in Tokamaks”, Nuclear Fusion 25 (1985) 1611;

[41] R. Albanese, G. Artaserse, F. Maviglia and F. Sartori, “Identification of Vertical Instabilities in JET Tokamak”, IEEE Trans. Magnetics 44 (2008) 1650–1653;

[42] S. L. Chen, F. Villone, B. J. Xiao, L. Barbato, S. Mastrostefano, Z. P. Luo, Y. Guo, L. Liu, “Equivalent axisymmetric plasma response models of EAST”, Plasma Physics and Controlled Fusion 58 (2016);

[43] V.D. Shafranov, L.E. Zakharov, “Use of the virtual-Casing principle in calculating the containing magnetic field in toroidal plasma systems”, Nucl. Fusion 12 (5) (1972) 599;

[44] K. Lackner, “Computation of ideal MHD equilibria”, Comput. Phys. Commun. 12 (1) (1976) 33;

[45] “ITER Plant Description Specification (PDS) and Plant Description Document (PDD)”, Chap. 3.7, Report G A0 FDR 1 01-07-13 R1.0, ITER (2000);

[46] J. Wesley, et al. “The ITER poloidal field system”, in Plasma Physics and Controlled Nuclear Fusion Research 1990 (IAEA-CN-53/F-III-16, Proc. 13th Int.Conf., Washington D.C., 1990), Vol. 3, IAEA Vienna, (1991) 421–426;

[47] R. H. Bulmer, “Tokamak Physics Experiment Poloidal Field Design”, Proc. 15th IEEE0NPSS Symp. Fusion Engineering, Vol. 2, p. 661, IEEE (1993);

[48] K. Toi, T. Takeda, “Optimum design of control coils in a tokamak device by nonlinear optimization”, Jpn. J. Appl. Phys. 16 (2) (1977) 325;

[49] T. Kobayashi, K. Tani, S. Tamura, “Determination of optimum positions of the poloidal field coils of a large tokamak”, Jpn. J. Appl. Phys. 17 (12) (1978) 2139;

[50] R. Ambrosino, R. Albanese, et al., “Optimization of experimental snowflake configurations on TCV”, Nucl. Fusion 54 (2014);

[51] G. Calabrò, et al., “EAST alternative magnetic configurations: modelling and first experiments”, Nucl. Fusion 55 (2015);

[52] M. Ariola, A. Pironti, “Magnetic control of Tokamak plasmas”, Advanced in Industrial Control series, Springer (2008);

[53] R. Albanese, R. Ambrosino, A. Castaldo, V.P. Loschiavo, “Optimization of PF coil system in axysimmetric fusion devices”, Fusion Engineering and Design 133 (2018) 163–172;

[54] M. Kovari, “PROCESS runs for new baseline design EU DEMO1”, 2017: 02.05.2017;

[55] R. Ambrosino, R. Albanese, A. Castaldo, V. P. Loschiavo, S. McIntosh, H. Reimerdes, "WPDTT1 Final Report 2016 on Activity DTT1-AC3: Equilibrium generation" https://idm.euro-fusion.org/?uid=2MV7L9;

[56] G.F. Matthews, et al., "Investigation of the fluxes to a surface at grazing angles of incidence in the tokamak boundary", Plasma Phys. Controlled Fusion 32 (1990) 1301–1320;

[57] S. Ejima, et al., "Volt-second analysis and consumption in Doublet III plasmas", Nucl. Fusion 22 (1982) 1313;

[58] F.A. Potra, S.J. Wright, "Interior-point methods", J. Comput. Appl. Math. 124 (2000) 281–302;

[59] T.F. Coleman, Y. Li, "A reflective newton method for minimizing a quadratic function subject to bounds on some of the variables", SIAM J. Optim. 6 (4) (1995) 1040–1058;

[60] Kovari M., et al., "PROCESS: A systems code for fusion power plants—Part 2: Engineering", Fusion Eng. Des. 104 (2016) 9–20;

[61] R. Ambrosino, A. Castaldo, S. Ha, V. P. Loschiavo, S. Merriman, H. Reimerdes "Evaluation of feasibility and costs of alternative magnetic divertor configurations for DEMO", 30th Symposium On Fusion Technology (SOFT), 16-21 September 2018, Giardini Naxsos, Sicily, Italy;

[62] H. Reimerdes et al. "Towards an assessment of alternative divertor solutions for DEMO", 3rd IAEA DEMO programme workshop, 11-15 May 2015, Hefei, China;

[63] E.A. Lazarus et al, 1990, "Control of the vertical instabilities in Tokamaks", Nucl. Fusion 30 111;

[64] Y. Gribov et al., "Progress in the ITER Physics Basis: chapter 8. Plasma operation and control", Nucl. Fusion 47 S385, 2007;

[65] S. L. Chen, F. Villone, et al., "Effect of three-dimensional conducting structures on vertical stability in EAST", Nucl. Fusion 55 (2015) 013010 (11pp);

[66] Special Section on "DTT. Divertor Tokamak Test facility" - Guest Edited by R. Albanese et al., vol 122, November 2017;

[67] R. Ambrosino, et al., "The DTT device: poloidal field coil assessment for alternative plasma configurations", Fusion Eng. and Des., vol. 122, pp. 322-332

(2017);

[68] R. Ambrosino, A. Castaldo, G. Ramogida, R. Albanese, F. Crisanti, P. Martin, A. Pizzuto, F. Villone, "Magnetic configurations and electromagnetic analysis of the Italian DTT Device", 30th Symposium On Fusion Technology (SOFT), 16-21 September 2018, Giardini Naxsos, Sicily, Italy;

[69] R. Albanese, R. Ambrosino, A. Castaldo, G. De Tommasi, A. Mele, A. Pironti, B. J. Xiao, Z.P. Luo, "ITER-like vertical stabilization system for the EAST Tokamak", Nucl. Fus., Vol 57, 2017;

[70] A. Mele, R. Albanese, R. Ambrosino, A. Castaldo. G. De Tommasi, Z.P. Luo, A. Pironti, Q.P. Yuan, W. Yuehang, B.J. Xiao and the EAST team "MIMO shape control at EAST Tokamak", 30th Symposium On Fusion Technology (SOFT), 16-21 September 2018, Giardini Naxsos, Sicily, Italy;

[71] B.J. Xiao, Z.P. Luo, H. Li, G.Q. Li, L. Wang, G.S. Xu, D.M. Yao, Z.B. Zhou, G. Calabrò, F. Crisanti, A. Castaldo, R. Lombroni, S. Minucci, G. Ramogida, "Progress on in-vessel poloidal field coils optimization design for alternative divertor configuration studies on the EAST Tokamak", 30th Symposium On Fusion Technology (SOFT), 16-21 September 2018, Giardini Naxsos, Sicily, Italy;

[72] R. Albanese, R. Ambrosino, A.Castaldo, G. De Tommasi, L. Liu, Z. P. Luo, A. Mele, A. Pironti, B. J. Xiao, Q. P. Yuan, "A MIMO architecture for integrated control of plasma shape and flux expansion for the EAST tokamak", 2016 IEEE Multi-Conference on System and Controls, Buenos Aires, 19-22 September 2016;

[73] G. Calabrò, F. Maviglia, S. Minucci, B. Viola and JET Contributors, "Divertor currents optimization procedure for JET-ILW high flux expansion experiments", Fusion Eng. and Des., vol. 129, pp. 115-119 (2018);

[74] G. Ambrosino et al., "Plasma position and shape control for ITER scenarios", Final Report on EFDA Study Contract 07-1702/1579 (TW6-TPO-PLASMADYN1) (2007);